



NTNU – Trondheim
Norwegian University of
Science and Technology

Investigation of how Hydrophilic Silica Nanoparticles Affect Oil Recovery in Berea Sandstone

An Experimental Study

Gunnar Sie Dahle

Petroleum Geoscience and Engineering (2 year)

Submission date: June 2014

Supervisor: Ole Torsæter, IPT

Norwegian University of Science and Technology
Department of Petroleum Engineering and Applied Geophysics

Abstract

As many oil fields go into their final stage of production, new technologies are necessary in order to maintain the production and increase the recovery of hydrocarbons. Among these enhanced recovery techniques (EOR) are chemical injection, which has focus on increasing the effectiveness of waterfloods. The use of this technique has been hampered by its relatively high cost and substantial adsorption onto the rock formation. In recent years, nanofluids (suspended nanoparticles in brine) have been launched as a cheap, efficient and environmentally friendly alternative to other chemicals.

The purpose of this thesis was to determine the optimum nanoparticle morphology and particle size for enhancing oil recovery in Berea sandstone cores. Six different hydrophilic silica nanoparticles, with primary diameters ranging from 7 nm to 16 nm, were suspended in brine at 0,025, 0,05 and 0,075 wt% concentrations. Three of the nanoparticles were composed of fumed silica and the other three nanoparticles were composed of colloidal silica. Flooding experiments in Berea sandstone cores were conducted. Nanofluids were injected as a tertiary recovery method following a secondary water flooding. The experiments were performed at ambient conditions. Interfacial tensions and contact angles were measured in order to help explain the underlying mechanisms behind the increased recovery.

The results showed that the small particles were more chemically reactive due to their high specific surface area. These particles had the highest potential for reducing interfacial tension and altering wettability. However, the core flooding experiments showed that oil recovery increased with particle size. Thus it was concluded that the recovery mechanism is of a mechanical nature, rather than chemical. Microscopic diversion of fluid flow due to log-jamming was suggested as the dominating EOR mechanism, with only minor contributions from chemical mechanisms. The results also showed that the fumed silica particles had a higher potential to enhance oil recovery compared to the colloidal silica, and the optimal concentration for both morphologies was 0,05 wt%. Lastly, the coreflooding experiments showed that the nanoparticles had better effect in medium permeability cores compared to high permeability cores.

Sammendrag

Ettersom mange oljefelt går inn i sin siste produksjonsfase trengs nye teknologier for å opprettholde produksjonen og øke utvinningen av hydrokarboner. Blant teknikkene for økt oljeutvinning (EOR) finner vi kjemisk injeksjon, som har fokus på å øke effektiviteten av vannflømmingen. Bruken av disse teknikkene har vært hemmet av forholdsvis høye kostnader og betydelig adsorpsjon på reservoarbergarten. I senere år har nanofluidier (suspenderte nanopartikler i saltvann) blitt lansert som et billig, effektivt og miljøvennlig alternativ til andre kjemikalier.

Hensikten med denne oppgaven var å bestemme den optimale partikkelstørrelsen og morfologien av partiklene for å øke oljeutvinningen i Berea sandsteinskjerner. Seks forskjellige hydrofile silisiumdioksid nanopartikler, med primær diameter på 7 nm til 16 nm, ble suspendert i saltvann med en konsentrasjon på 0,025, 0,05 eller 0,075 vekt %. Tre av nanopartiklene er klassifisert som fumed silika partikler, og de tre andre nanopartiklene er klassifisert som kolloide silika partikler. Det ble gjennomført en rekke kjerneflømminger i Berea sandsteinskjerner hvor nanofluidier ble injisert som en tertiær utvinningsmetode etter en sekundær vannflømming. Forsøkene ble utført ved romtemperatur. Grenseflatespenninger og kontaktvinkler ble målt for å bidra til å forklare de underliggende mekanismene bak den økte utvinningen.

Resultatene viste at de små partiklene var mest kjemisk reaktive, dette på grunn av deres høye spesifikke overflateareal. Disse partiklene hadde høyest potensial for å redusere grenseflatespenningen og endre fuktpreferansen til reservoarbergarten. Kjerneflømmingene viste derimot at oljeutvinningen øker med partikkelstørrelsen. Derfor ble det konkludert med at utvinningsmekanismen er av en mekanisk natur, snarere enn et resultat av kjemiske prosesser. Log-jamming ble foreslått som den dominerende EOR mekanismen, med noen mindre bidrag fra kjemiske mekanismer. Resultatene viste også at fumed partikler hadde et høyere potensial til å øke oljeutvinningen i forhold til de kolloide partiklene. Den optimale konsentrasjonen av partikler for økt oljeutvinning var 0,05 vekt%. Kjerneflømmingene viste at partiklene hadde bedre effekt i medium permeable kjerner sammenliknet med høy permeable kjerner.

Acknowledgements

This master thesis was carried out at the Norwegian University of Science and Technology (NTNU), at the Department of Petroleum Engineering and Applied Geophysics during the spring of 2014.

I would like to thank all of those who have guided, inspired and educated me throughout the whole process of writing this thesis.

Special thanks to my supervisor Ole Torsæter for his expert advice and encouragement. I would also like to thank Roger Overå for his assistance in the lab, and for always being available when problems occurred.

All the laboratory work was performed together with Ph.D. student Katherine Rose Aurand. She deserves tons of credit and a special thanks for guidance, excellent collaboration and for taking time to give me valuable feedback on my work. Lastly I would like to thank Tor Arild Melby for proofreading and useful discussions.

Contents

Abstract	1
Sammendrag	3
Acknowledgements	5
List of Figures	11
List of Tables	15
1 Introduction	1
1.1 Objective	2
1.2 Structure of the report	2
2 Basic Concepts and Definitions in Reservoir Engineering	5
2.1 Reservoir Properties	5
2.1.1 Porosity	5
2.1.2 Saturation	6
2.1.3 Surface and Interfacial Tension	7
2.1.4 Wettability	8
2.1.5 Capillary Pressure	9
2.1.6 Permeability	10
2.2 Fluid Properties	12
2.2.1 Density	13
2.2.2 Viscosity	14
2.2.3 Compressibility	15
3 Introduction to Nanotechnology for Enhanced Oil Recovery	17
3.1 Nanofluids	17
3.1.1 Potential Nanoparticles	18
3.2 Mechanims for Increased Recovery	19
3.2.1 Structural Disjoining Pressure	19
3.2.2 Effect on Interfacial Tension	21
3.2.3 Effect on Wettability	22

3.2.4	Effect on Viscosity	23
3.2.5	Retention of Nanoparticles in Porous Media	24
4	Experimental Setup	27
4.1	Preparation of Core Samples	27
4.1.1	Cleaning of Cores	27
4.1.2	Porosity Measurement	28
4.1.3	Permeability Measurement	30
4.1.4	Saturation Cores with Brine	31
4.1.5	XRD-Analysis	31
4.2	Fluid Properties	32
4.2.1	Brine	32
4.2.2	Nanoparticles	32
4.2.3	Nanofluids	33
4.2.4	Crude Oil	34
4.2.5	Densities and Viscosities	35
4.2.6	Interfacial Tension and Contact Angle	36
4.3	Coreflood setup	39
4.4	Coreflood Scheme	41
5	Experimental Results	43
5.1	Core Properties	43
5.1.1	Porosity and Permeability	44
5.1.2	XRD-Analysis	47
5.2	Viscosity and Density Measurements	47
5.3	Contact Angle	48
5.4	Interfacial Tension	49
5.4.1	IFT at Different Concentrations	50
5.5	Stability of Nanofluids	52
5.5.1	IDISIL EM-7520K	53
5.6	Core flooding	54
5.6.1	Medium Permeability Cores	54
5.6.2	High Permeability Cores	56
5.6.3	Differential Pressure	57
5.6.4	Concentration Tests	58
5.6.5	Coreflooding Summary	60
5.6.6	Validation tests	61
6	Discussion	63
6.1	Wettability Alteration	63
6.2	Interfacial Tension	64
6.3	Retention of Nanoparticles	66
6.4	Coreflooding Experiments	68
6.4.1	Recovery at Different Nanoparticle Concentrations	72
6.4.2	Limitations and Complications	73

7 Conclusion	75
7.1 Future Work	76
Symbols	78
References	81
A Core Data	89
B Nanofluid Properties	101
C Flooding Results	107

List of Figures

2.1	Pore space in a rock.	6
2.2	A droplet on surface.	7
2.3	How the interfacial tensions works on a droplet/bubble.	9
2.4	Curved interface between oil and water due to pressure difference.	9
2.5	Typical capillary pressure curves.	10
2.6	Connected pores gives permeability.	11
2.7	Typical relative permeability curves for water wet sandstone.	12
2.8	Two-phase diagram of reservoir fluids showing how they will vary with different pressure and temperature.	13
2.9	Velocity profile.	14
2.10	Viscosity variations with temperature.	15
3.1	Nanoparticles establishing a wedge-film, resulting in a structural disjoining pressure.	19
3.2	Disjoning pressure in the wedge structure.	21
3.3	Breakup of oil droplets due to adsorption of nanoparticles.	22
3.4	Effect of viscosity and relative permeability on displacement.	24
3.5	The four different mechanisms of retention.	25
4.1	Soxhlet Extraction.	28
4.2	Helium porosimeter apparatus.	29
4.3	Constant Head Permeameter.	30
4.4	Vacuum pump setup.	31
4.5	Precipitation of nanoparticles.	34
4.6	Rotating viscometer.	35
4.7	The spinning drop method.	38
4.8	The spinning drop video tensiometer.	38
4.9	Imaging method for contact angle measurement.	39
4.10	Schematic of experimental setup.	40
5.1	Graphical presentation of porosity and permeability of the high permeability cores.	45
5.2	Graphical presentation of porosity and permeability of the medium permeability cores.	45
5.3	Graphical presentation of porosity and permeability of the cores from block 9.	46

5.4	IFT between oil and different nanofluids at 0,05 wt%.	49
5.5	IFT between oil and AERODISP W 7620 N.	51
5.6	IFT between oil and AERODISP W 7320 N.	51
5.7	IFT between oil and VP Disp W 3520 XN.	52
5.8	Fumed silica nanofluid after a week.	53
5.9	Destability of IDISIL EM-7520K.	53
5.10	Increased Recovery using 0,05 wt% fumed nanoparticles.	55
5.11	Increased Recovery using 0,05 wt% colloidal nanoparticles.	55
5.12	Increased Recovery using 0,05 wt% fumed nanoparticles.	56
5.13	Increased Recovery using 0,05 wt% colloidal nanoparticles.	57
5.14	Differential pressure across medium permeability cores.	58
5.15	Differential pressure across high permeability cores.	58
5.16	Recovery from AERODISP W 7620 N at different concentrations.	59
5.17	Increased recovery from AERODISP W 7320 N at different concentrations.	59
5.18	Increased recovery from VP Disp 3520 XN at different concentrations.	60
5.19	Test 2 using 0,05 wt% fumed silica in medium permeability cores.	62
5.20	Increased recovery from AERODISP W 7320 N in a high permeability core.	62
6.1	Spreading of nanoparticles.	64
6.2	Log-jamming.	70
A.1	Klinkenberg Plots for core 1H-6H.	96
A.2	Klinkenberg Plots for core 7H-10H and 1M-2M.	97
A.3	Klinkenberg Plots for core 3M-8M.	98
A.4	Klinkenberg Plots for core 9-1 to 9-6.	99
A.5	Klinkenberg Plots for core 9-7 to 9-10.	100
B.1	The imaging method for measuring contact angle.	101
B.2	Contact angle measurements of an oil droplet in North Sea Brine.	104
B.3	Contact angle measurements of an oil droplet in AERODISP W 7620 N.	104
B.4	Contact angle measurements of an oil droplet in VP Disp 3520 N.	105
B.5	Contact angle measurements of an oil droplet in AERODISP W 7320 N.	105
B.6	Contact angle measurements of an oil droplet in IDISIL IC 0820.	106
B.7	Contact angle measurements of an oil droplet in IDISIL SI 1520.	106
C.1	AERODISP W 7620 N flooding in medium permeability core.	109
C.2	AERODISP W 7620 N flooding in high permeability core.	109
C.3	AERODISP W 7320 N flooding in medium permeability core.	110
C.4	AERODISP W 7320 N flooding in high permeability core.	110
C.5	VP Disp W 3520 XN flooding in high permeability core.	111
C.6	VP Disp W 3520 XN flooding in high permeability core.	111
C.7	IDISIL IC 0820 flooding in high permeability core.	112

C.8	IDISIL IC 0820 flooding in high permeability core.	112
C.9	IDISIL SI 1520 flooding in high permeability core.	113
C.10	IDISIL SI 1520 flooding in high permeability core.	113
C.11	IDISIL EM-7520 K flooding in high permeability core.	114
C.12	IDISIL EM-7520 K flooding in high permeability core.	114
C.13	IDISIL 7620 W at 0,025% flooded in medium permeability core. . .	115
C.14	IDISIL 7620 W at 0,075% flooded in medium permeability core. . .	115
C.15	Vp Disp W 3520 XN at 0,025% flooded in medium permeability core.	116
C.16	Vp Disp W 3520 XN at 0,075% flooded in medium permeability core.	116
C.17	AERODISP W 7320 N at 0,025% flooded in medium permeability core.	117
C.18	AERODISP W 7320 N at 0,075% flooded in medium permeability core.	117
C.19	AERODISP W 7320 N at 0,05% flooded in medium permeability core.	118
C.20	AERODISP W 7620 N at 0,05% flooded in medium permeability core.	118
C.21	VP Disp W 3520 XN at 0,05% flooded in medium permeability core.	119
C.22	AERODISP W 7320 N at 0,05% flooded in high permeability core. .	119

List of Tables

4.1	Composition of the North Sea brine.	32
4.2	Nanoparticles used in making the nanofluids.	33
4.3	Properties of the oil sample used.	35
4.4	Refractive Index of aqueous phases.	37
5.1	Core flooding test summary.	44
5.2	XRD analysis of the cores.	47
5.3	Density and viscosity at the given temperature.	48
5.4	Contact angle measurements.	49
5.5	Interfacial Tension and percentage reduction compared to brine. All nanofluids have a 0,05 wt% concentration.	50
5.6	Summary of the increased recovery from 0,05 wt% nanofluids in medium and high permeability cores.	60
A.1	Core dimensions and porosity.	89
A.2	Core dimensions and porosity.	90
A.3	Pore volume of the cores.	90
A.4	Mineral analysis of the cores, five samples from each block.	91
A.5	Air permeability measurements and Klinkenberg Corrections.	92
A.6	Air permeability measurements and Klinkenberg Corrections.	93
A.7	Air permeability measurements and Klinkenberg Corrections.	94
B.1	Nanofluid properties. Particle and aggregate sizes are presented with average diameter.	102
B.2	Measured fluid properties at 22,8°C.	103
C.1	Core flooding summary. The first ten tests used 0,05 wt% nanofluids. The next six tested nanofluids at different concentrations. The last four testes were used to validate the previous results.	108

Chapter 1

Introduction

With a growing demand for energy the production of both non-renewable and renewable resources need to be increased. The demand for oil can be met in two ways: either by finding new hydrocarbon sources or by increasing the recovery of existing reservoirs. However, rate of discoveries of new oil fields are decreasing. As many oil fields goes into their final stage of production, as much as two thirds of the oil in place cannot be produced by conventional production methods. ([Kong and Ohadi, 2010](#)) Implementing enhanced recovery (EOR) techniques are therefore essential to keep up the oil production. In the petroleum industry nanotechnology has made its presence felt during the last few decades. Nanoparticles have been applied to upstream operations by developing better materials, they have been used as tracers, and dispersions with nanoparticles have been used for asphaltene/scale/paraffin remediation. Another emerging application of nanotechnology in the petroleum sector is the development of new types of smart fluids. Among these new nanoformulas are surfactants/polymers, microemulsions, colloidal dispersion gels etc. used in drilling, enhanced oil recovery etc. ([Evdokimov et al., 2006](#)) Recently researchers have begun looking into the so-called nanofluids. As the name suggests, nanofluids are dispersions containing small volumetric fractions of nanosized solid particles, which can be designed to give different properties. While surfactants and polymer are highly costly and potentially harmful to the environment, nanofluids have been launched as a possible cheap and green alternative.

Engineered silica nanoparticles (SNP) have been investigated and shown promising results in terms of altering reservoir and fluid properties for enhanced oil recovery.

The particles can be uniquely tailored giving them a certain set of properties designed for a given reservoir system. Laboratory experiments have shown up to 8 % increased recovery in some cases, while others have shown that additional recovery is not granted at all. (Hendraningrat et al., 2012, 2013e; Li et al., 2013a)

1.1 Objective

Before nanofluids can be applied as an EOR method, it is important to know as much as possible about the effects and mechanisms behind this technology. By establishing this, accurate predictions of the outcome from the EOR process can be achieved. Studies have shown that dispersions with nanoparticles in the injection water can potentially increase the oil recovery. However, in some cases it has been observed that the formation has taken damage. The main objective of this project is to investigate how different sizes of fumed and colloidal silica nanoparticles will affect the oil recovery process in Berea Sandstones. Coreflooding experiments were conducted at different permeabilities to investigate the potential of the particles. Interfacial tension and contact angle measurements were performed to support the findings and help explaining the underlying mechanisms behind the increased recovery.

1.2 Structure of the report

This thesis is an experimental study of nanoparticles and their application for enhanced oil recovery. Special emphasis has been placed on silica particles as they are the basis for the laboratory work. The thesis is organized as followed:

- Chapter 2 provides an overview of important reservoir and fluid properties and concepts.
- Chapter 3 gives an introduction to nanoparticles with special focus on how they are applicable as EOR agents.
- Chapter 4 describes the experimental setup and procedures employed for this thesis.

- Chapter 5 presents the experimental results.
- Chapter 6 evaluate, analyses and discusses the results. Relevant literature by other authors are reviewed.
- Chapter 7 rounds up the thesis and makes some concluding remarks based on the findings.

Chapter 2

Basic Concepts and Definitions in Reservoir Engineering

To understand the subsurface processes working in the reservoir, an understanding of basic reservoir engineering is important. The hydrocarbon system is complex, and driven by interaction between the components present (rock, water, oil and/or gas). This chapter explains the basic properties of oil and gas systems.

2.1 Reservoir Properties

2.1.1 Porosity

Porosity is defined as the rock's capacity to store fluids. The void part between rock grains and mineral cement is necessary in order to have hydrocarbons present in the rock, and the porosity is considered one of the most important parameters of a reservoir. The porosity can be expressed as the ratio of pore volume V_p over the total bulk volume V_b of the rock sample. Pore volume can be expressed as the grain volume, V_g subtracted from the bulk volume:

$$\phi = \frac{V_p}{V_b} = \frac{V_b - V_g}{V_b} \quad (2.1)$$

This is called the total porosity, where all the pore space is taken into account irrespectively if the pores are interconnected or not. The effective porosity corresponds to the interconnected pores only, which permits fluid flow. Hence it is a measure of the producible fluids in the reservoir. (Zolotukhin and Ursin, 2000)

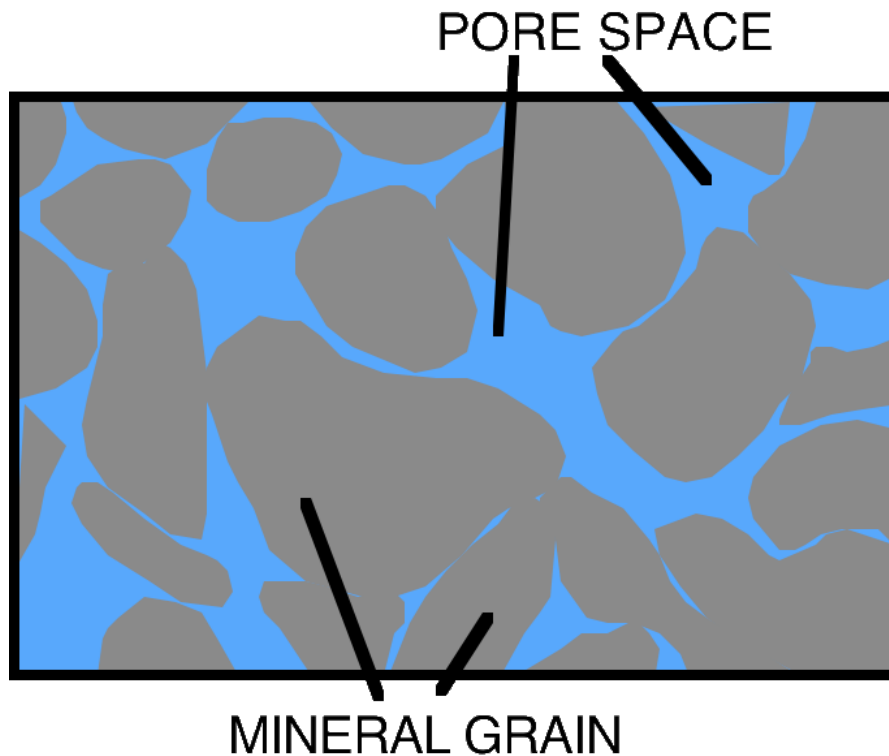


FIGURE 2.1: Pore space in a rock. (Wisconsin Geological Survey, 2010)

2.1.2 Saturation

The pore space in a reservoir rock is filled with oil, gas and water. The saturation, S , is the fraction of pore volume occupied by a specific fluids:

$$S_i = \frac{V_i}{V_p} \quad (2.2)$$

where i denotes a particular fluid (oil, water, gas) and V_p is the pore volume. Consequently, the sum of all fractions will equal the total pore space:

$$\sum S_i = S_w + S_o + S_g = 1 \quad (2.3)$$

where w, o and g denotes water, oil and gas respectively. The relationship between the fluid fraction can be subjected to progressive changes during production, in respect to both time and space. (Zolotukhin and Ursin, 2000)

2.1.3 Surface and Interfacial Tension

Fluids have a natural tendency to minimize their surface area. To achieve this, droplets tend to form a spherical structure. This phenomenon occurs because molecules of the same fluid attract each other. At a surface or interface, the molecules have fewer neighbors of the same chemical compound, and they will try to minimize the number of broken bonds by minimizing the surface area. (Daugherty et al., 1985)

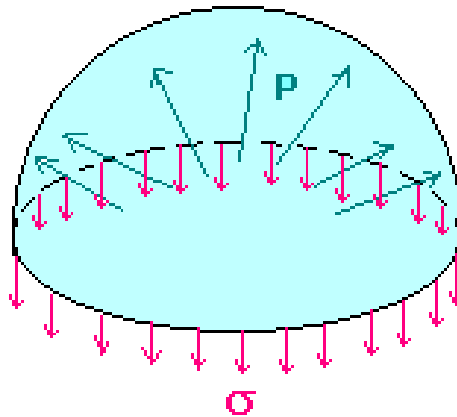


FIGURE 2.2: A droplet on surface. (Torsæter, 2012)

Interfacial tension (IFT), σ , is a force (per unit length) that is tangent to the interface between two immiscible fluids or at a fluid-solid interface. The surface forces are acting on the perimeter of droplets/bubbles, and work to make an equilibrium force balance in the horizontal direction. "Surface" tension is defined as the interfacial tension between a liquid and vapor. For a two-phase fluid system with constant mass, the interfacial tension under isothermal and isobaric condition can be formulated as follows:

$$\gamma = \frac{(\partial)G}{(\partial A)_{T,P,m}} \quad (2.4)$$

where G is Gibbs free energy (chemical potential) and A is the interface area. From the free energy term we can see that for a high IFT, molecules are strongly attracted to the molecules of their own kind and thereby the two fluids are immiscible. A low IFT means that the molecules are more strongly attracted to molecules of the other fluids, and hence a dissolution occurs, resulting in a stable new mixture.

IFT is an important parameter as the interaction between fluids and rock minerals affects reservoir properties like wettability, capillary pressure, relative permeability, viscosity, saturation distribution and displacement efficiency. (Pedersen et al., 1989; Hocott, 1939; Batychy and McCaffery, 1978)

Adding surfactants or nanoparticles to a fluid interface can significantly lower the interfacial tension as they adsorb at the interface between fluids, and lowers the repulsion between molecules of different fluids.

2.1.4 Wettability

A porous rock saturated with more than one fluid is a complex system of mutual static interactions between all the fluids present and between fluids and rock minerals. Wettability is defined as the tendency of one fluid to spread on to a solid's surface in the presence of another immiscible fluid. It is a result of interfacial tension between the fluid phases present and their individual adhesive attraction (electrostatic force) to the solid. The wettability of a rock's pore wall is dependent on the fluid's chemical composition and the rock's mineral composition (e.g. siliciclastic vs. carbonate). (Zolotukhin and Ursin, 2000)

Contact angle (θ) is a measurement of the degree of wetting by a particular fluid. This can be described to Youngs equation:

$$\cos \theta = \frac{\gamma_{SV} - \gamma_{SL}}{\gamma_{LV}} \quad (2.5)$$

where θ is the contact angle, γ is surface/interfacial tension and S, V and L denotes solid, vapor and liquid respectively. The contact angle can be measured at the fluid-fluid interface on the solid.

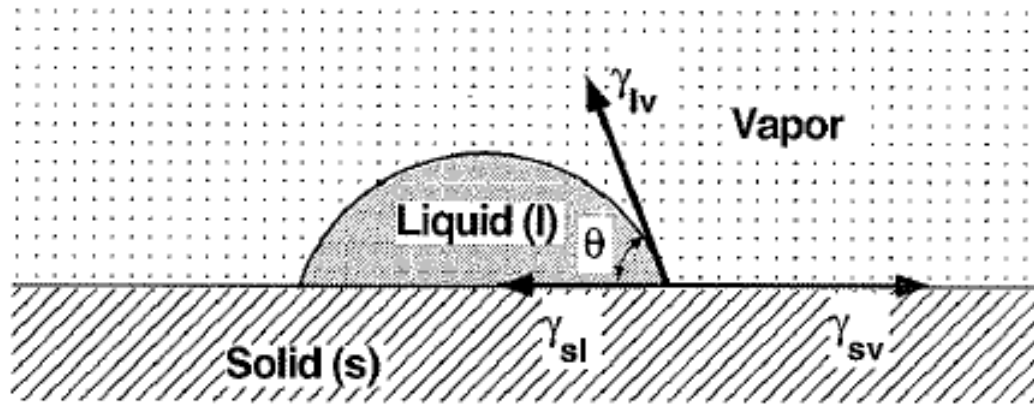


FIGURE 2.3: How the interfacial tensions works on a droplet/bubble. (Hiemenz and Rajagopalan, 1997)

For low contact angles ($\theta < 90^\circ$) the fluid is defined as the wetting phase while for higher contact angles ($\theta > 90^\circ$) the fluid is non-wetting. 90° angles indicates neutral wettability.

2.1.5 Capillary Pressure

When two immiscible fluids are in contact, the interfacial tension will cause the interface that separates the two fluids to curve. The stronger adhesive force of the wetting fluid will establish a meniscus, concaving towards the non-wetting fluid. The molecular pressure difference across the fluid interface is called *Capillary Pressure*, P_c :

$$P_C = P_{non-wetting} - P_{wetting} = \frac{2 * \sigma * \cos\theta}{r} \quad (2.6)$$

where r is the effective radius of the curved interface, θ is the contact angle and σ is the interfacial tension. (Bear and Bachmat, 1990)

The capillary pressure is a function of pore size, wettability, interfacial tension and saturation history. A typical capillary pressure curve for imbibition (wetting phase increase in saturation) and drainage (wetting phase decrease in saturation) can be seen in Figure 2.5.

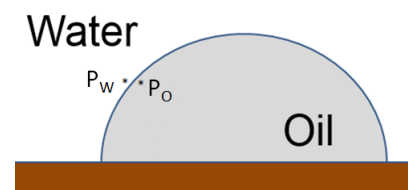


FIGURE 2.4: Curved interface between oil and water due to pressure difference. ($P_w < P_o$)

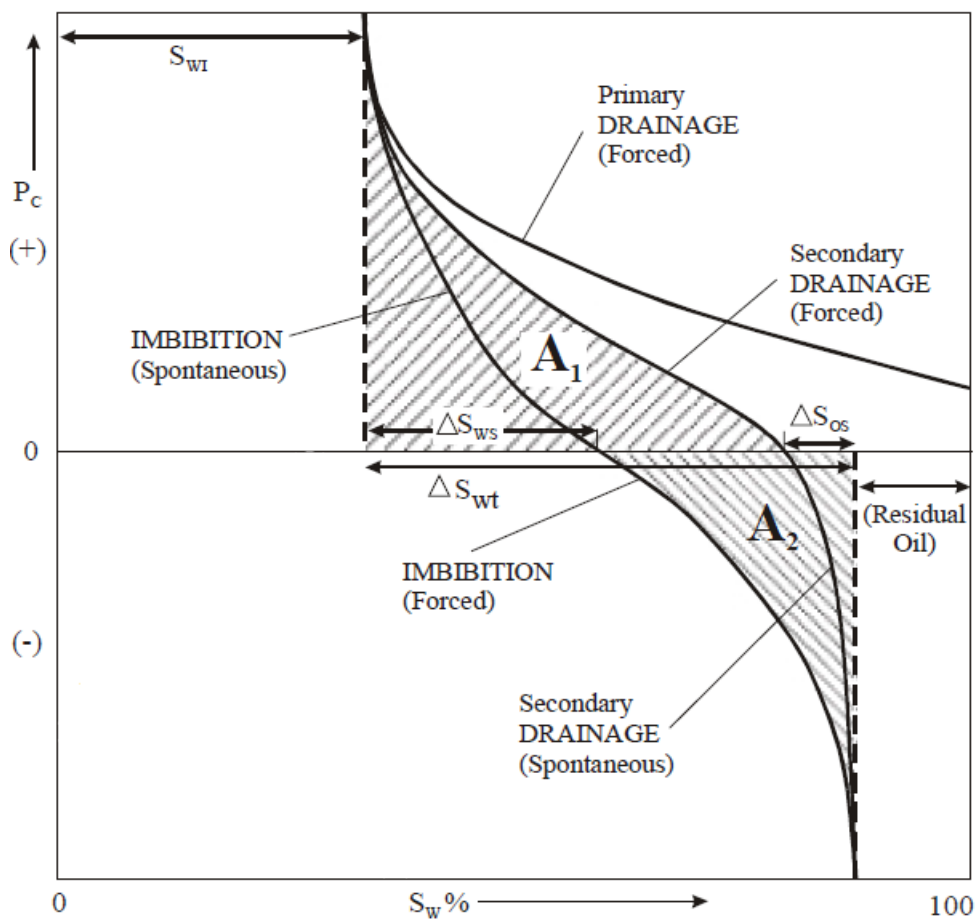


FIGURE 2.5: Typical capillary pressure curves. (Torsæter and Abtahi, 2000)

2.1.6 Permeability

Permeability, k , of a porous medium is defined as the medium's ability to transmit fluids through its interconnected pores. It is, together with porosity, considered the most important parameters of reservoirs. Permeability is a directional property, or a tensor, meaning it may vary by several magnitudes depending on the fluid flow direction. (Torsæter and Abtahi, 2000)

Darcy's law shows that a laminar, one-phase, steady-state flow with a fluid flow rate, q , obeys the following relationship:

$$\frac{q}{A} = u = -\frac{k}{\mu} * \frac{dP}{dx} \quad (2.7)$$

where A is the cross sectional area, k is the permeability and μ is the viscosity of the fluid. dP is the pressure drop over the length dx .

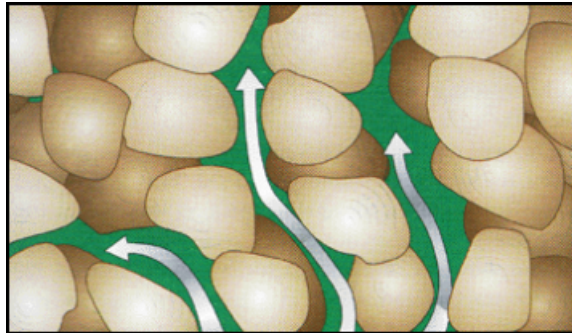


FIGURE 2.6: Connected pores gives permeability. (MPG Petroleum, 2003)

Darcy's Law refers to a situation with 100 % saturation of one fluid, this is rarely the case for actual reservoirs. In order to generalize the equation the concept of *effective* permeability, k_{je} , is introduced to describe multiphase flow. The effective permeability is the ability of the porous medium to conduct a fluid with less than 100 % saturation of the pore space.

Relative permeability, k_{rj} , is a concept used to relate the absolute permeability (100% saturated with one fluid) to the effective permeability of a particular fluid in the system. It can be decomposed as shown below:

$$k_{ej} = k_{rj} * k \quad (2.8)$$

The relative permeability is a strong function of the saturation of the phase. Being a rock-fluid property, relative permeability is also a function of rock properties (e.g. pore size distribution), saturation history and wettability. (Zolotukhin and Ursin, 2000) Relative permeability curves represent the dependence of saturation and saturation history on relative permeability. These curves shows end-point saturations and end-point permeabilities for drainage and imbibition processes, giving valuable information about recoverable oil, sweep efficiency etc. (Torsæter and Abtahi, 2000)

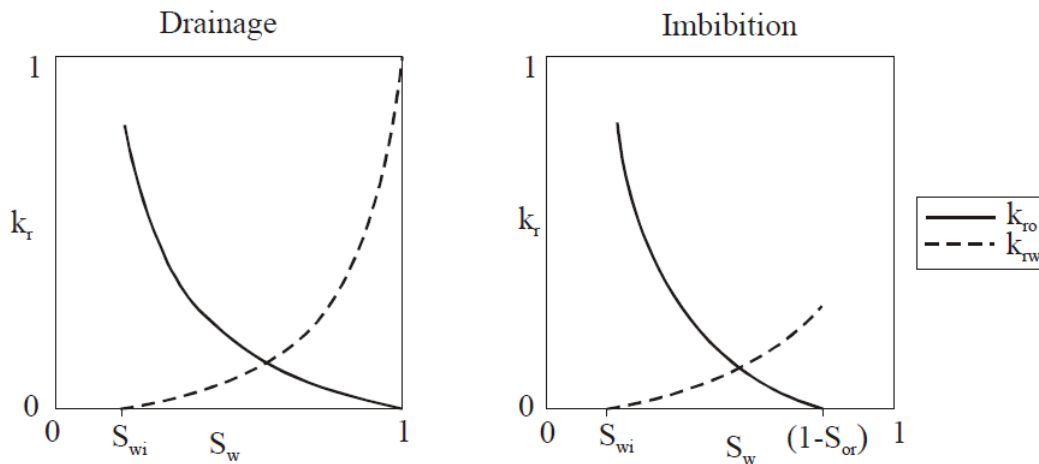


FIGURE 2.7: Typical relative permeability curves for water wet sandstone.
(Zolotukhin and Ursin, 2000)

2.2 Fluid Properties

Petroleum fluids are complex compositions of paraffins, naphthenes, aromatic series and often non-hydrocarbon components. Each mixture behaves differently in various situations.

During production the reservoir will undergo significantly changes to both temperature and pressure which affect the hydrocarbon mixture. Figure 2.8 illustrates how different types of depleting reservoirs. For the same hydrocarbon system, the type of reservoir is given by the initial pressure and temperature. Every composition of hydrocarbons have their own two-phase diagram. A given pressure and temperature will pinpoint a location in the diagram that will determine the type of reservoir fluid present. (Whitson and Brulè, 2000)

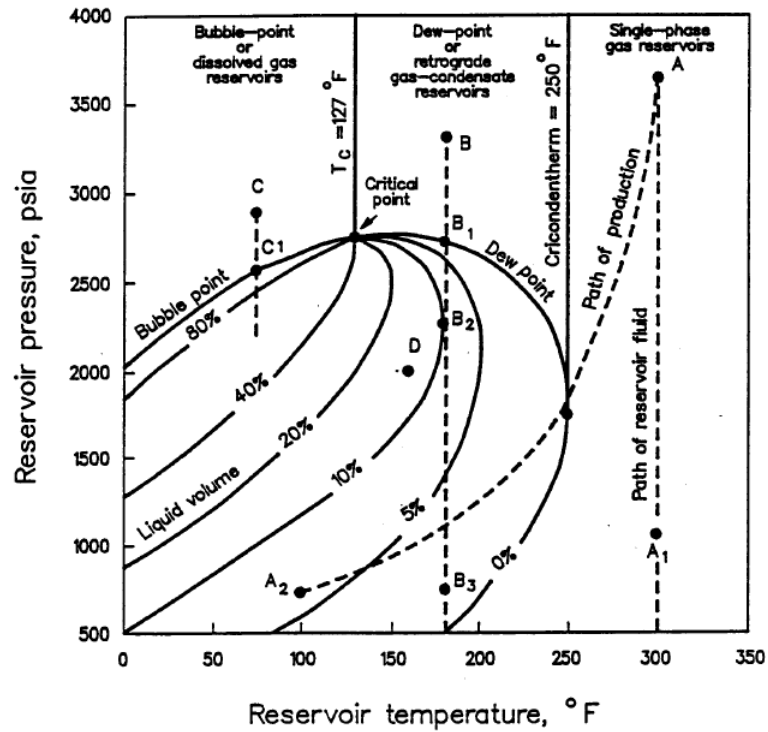


FIGURE 2.8: Two-phase diagram of reservoir fluids showing how they will vary with different pressure and temperature. (Whitson and Brulè, 2000)

2.2.1 Density

Density, ρ , is defined as the mass of a liquid, m , per unit of volume, v . As this property differs with pressure and temperature, it's important to report the density at a given reference point. Normally this is at 288 K and 1 atm (101 kPa). (Torsæter and Abtahi, 2000)

$$\rho = \frac{m}{V} \quad (2.9)$$

The term *specific gravity*, γ , is defined as ratio volume of a given liquid to the volume of water at given temperature and water:

$$\gamma = \frac{\rho_{liquid}}{\rho_{water}} \quad (2.10)$$

2.2.2 Viscosity

Viscosity, μ , is defined as a fluid's resistance to shear or angular deformation, or the internal resistance of a fluid to flow. The resistance to flow is caused by friction forces as a result of cohesion and momentum interchange between molecules. (Daugherty et al., 1985) The basic equation of deformation by shear stress (τ) is given by:

$$\tau = \mu \frac{\partial v}{\partial y} \quad (2.11)$$

where $\frac{\partial v}{\partial y}$ is the shear rate. The shear stress can also be defined as F/A , where F is the required force to keep the upper plate moving at a constant velocity in the x-direction. The viscosity transmits a force through the fluid to the lower plate, causing a linear velocity profile in x-direction, as seen in Figure 2.9.

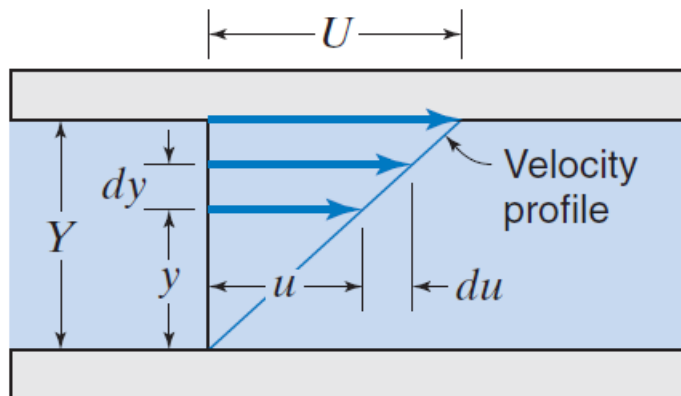


FIGURE 2.9: Velocity profile. (Daugherty et al., 1985)

Kinematic viscosity, ν , is the ratio between absolute viscosity and fluid density:

$$\nu = \frac{\mu}{\rho} \quad (2.12)$$

Viscosity of fluids are dependent on their temperature (and in some cases the pressure). Liquids tend to increase their viscosity as the temperature increases. This is because the forces of cohesion diminish with increasing temperature.

Gases have the exact opposite behavior, the viscosity increases as the temperature increases. The applied energy will cause some gas molecules to increase their

velocity which speeds up slower moving molecules, while the slow moving molecules slow down the fast moving ones. This molecular interchange will increase the friction force and hence the viscosity. (Daugherty et al., 1985)

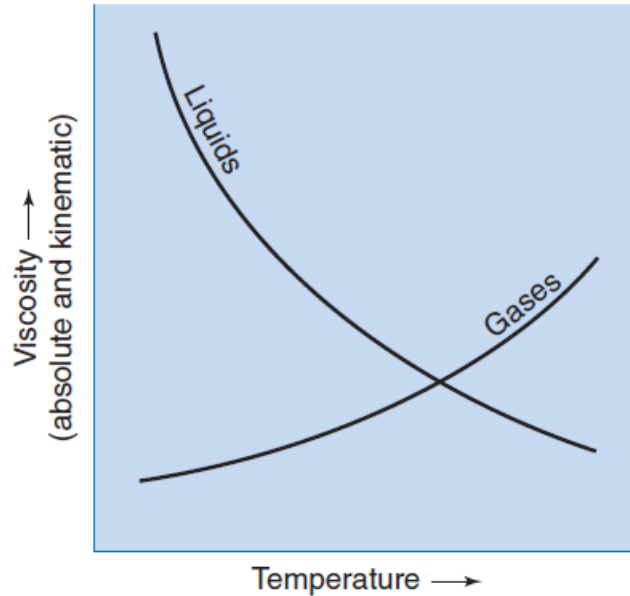


FIGURE 2.10: Viscosity variations with temperature. (Daugherty et al., 1985)

2.2.3 Compressibility

For engineering purposes the reservoir fluid can be classified as either (a) incompressible, (b) compressible, or (c) gas. The concept of incompressible fluid means that the fluid volume does not change with pressure. A compressible liquid will experience a small volume change with pressure while gases are highly compressible compared to liquids. (Craft et al., 1991) The tight packing of molecules in liquids compared to gases makes them harder to compress or expand. *Compressibility, C*, are defined relative volume change for a constant fluid mass that is subjected to pressure change:

$$C = -\frac{1}{V_f} * \left(\frac{dV_f}{dP}\right)_T = \frac{1}{\rho_f} * \left(\frac{d\rho_f}{dP}\right)_T \quad (2.13)$$

The negative sign indicates that as the pressure increases the volume decreases. Equation 2.13 are for isothermal conditions, but fluid compressibility is also a function of temperature and will increase with increasing temperature. Determining

compressibility for the reservoir fluids is of great importance for predicting expected pressure development and accurate reservoir volumes. ([Trube, 1957](#); [Ling and Shen, 2011](#))

Chapter 3

Introduction to Nanotechnology for Enhanced Oil Recovery

Manipulating a matter on atomic and molecular scale is called nanotechnology. This technology has become very important in recent decades and has spread to several different sectors of the industry like medicine, electronics and energy sector. In terms of the oil and gas industry, nanofluids have been launched as a promising future technology for enhanced oil recovery (EOR). Nanoparticles (NP) have been engineered to fit a wide variety of applications. Recent studies have shown that it might also be applicable as a method for EOR. Nanoparticles can mobilize trapped oil in the porous rock, or they can be used in combination with surfactants/polymers to enhance their effect and migration range.

3.1 Nanofluids

A nanofluid is a dispersion where small sized solid particles are suspended in a carrying fluid, usually water. A nanoparticle is typically between 1 nm and 100 nm. Their size is much smaller than rock pore channels, meaning nanoparticles can easily penetrate through the reservoir rock without much retention. ([Li et al., 2013a](#))

Nanofluids can be designed with a wide variety of properties. Two of the main characteristics of nanoparticles is widely different from other EOR agents and can

change the properties drastically; Firstly, their surface area to volume ratio is higher compared to similar material in a larger scale. This can enhance strength, electrical properties and make materials more chemical reactive. The overall effect is that less amount of NPs are needed compared to other chemicals like surfactants to achieve the same functions. In addition, quantum effects can affect the optical, electrical and magnetic behavior of the material. ([Nanowerk](#))

3.1.1 Potential Nanoparticles

In many studies performed on nanofluids for EOR an inorganic ceramic material composed of silica dioxide (SiO_2) is used as nanoparticle. Some of the advantages with silica nanoparticles, apart from being cheap and easy accessible, is that they offer: (i) increased sedimentation stability as surface forces counter balance the gravity force; (ii) thermal, stress-strain and rheological properties can be tailored for a certain purpose during production by changing size, shape and surface chemistry of the nanoparticles and (iii) the chemical properties of nanoparticles can easily be controlled by surface coating substances. ([Miranda et al., 2012](#)) Silica nanoparticles can be designed to be both hydrophilic and lipophobic (LHP) or hydrophobic and lipophilic (HLP) using surface treatment such as silanization with a hydroxyl group or sulfonic acid. ([Hendraningrat et al., 2013e](#)) As silica is found naturally as the main component in sandstone it will be easy to extract and also environmentally friendly. It is the most abundant mineral in the crust of the earth. ([Heiserman, 1991](#))

Other types of nanoparticles have also been studied as potential EOR agents. Among these types are metal oxides of aluminum, zinc, magnesium, iron, zirconium, nickel and tin. ([Ogolo et al., 2012](#); [Zhang et al., 2013](#)) The results of these studies showed that only the aluminum and nickel oxides improved the recovery, where aluminum gave the best result. The increased recovery was explained by aluminum's ability to decrease oil viscosity, and nickel's ability to increase the brine viscosity, both cases giving a favorable mobility factor (M). Magnesium- and zinc oxides caused severe permeability problems and decreased recovery. ([Ogolo et al., 2012](#))

3.2 Mechanisms for Increased Recovery

Several different EOR mechanisms for nanofluid are proposed and studied. Well established concepts of wettability alteration and interfacial tension reduction are not sufficient to fully explain the increased recovery seen. An overview of the potential EOR mechanisms will be given here.

3.2.1 Structural Disjoining Pressure

One of the most prominent mechanisms is the disjoining pressure. Investigations performed by Wasan and Nikolov (2003), Chengara et al. (2004), Wasan et al. (2011) and Mcelfresh et al. (2012) has revealed that the nanoparticles present in the three phase region between oil, water and rock tend to force themselves in between the discontinuous phase and the solid rock surface. The nanoparticles are creating a wedge like structure which works to separate the formation fluid (oil) from the pore wall and enhances the spreading behavior of the nanofluid.

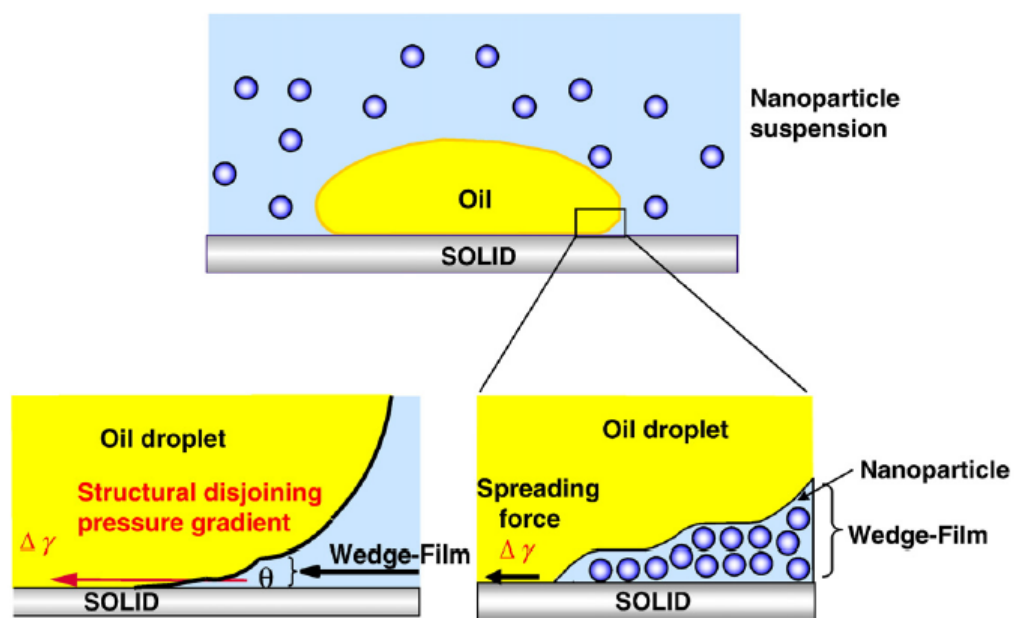


FIGURE 3.1: Nanoparticles establishing a wedge-film, resulting in a structural disjoining pressure. (Wasan et al., 2011)

When an oil/liquid drop dispersed in an aqueous nanofluid approaches a smooth, hydrophilic solid surface, nanoparticles will assemble themselves in a solid-like

ordering at the three-phase contact region, see Figure 3.1. This assembly becomes more disordered and fluid-like towards the bulk phase. Studies have shown that the pressure arising from such an ordering in the confined region will enhance the spreading behavior of nanofluids. (Wasan and Nikolov, 2003; Zhang et al., 2014) The particles that are present in the three-phase contact region will tend to form a wedge-like structure and force themselves in between the discontinuous phase and the solid rock surface. Particles present in the bulk fluid will apply a pressure that forces the particles in the wedge structure forward. This applied force is called the structural disjoining pressure, or film tension gradient ($\Delta\gamma$). (Mcelfresh et al., 2012)

The driving forces behind this phenomenon are electrostatic repulsion (where equal charged particles repel each other), Brownian Motion (random movement) and van der Waals forces (attraction/repulsion between molecules due to dipoles). (Mcelfresh et al., 2012) The ordering of particles inside the wedge structure can occur because the overall entropy of the dispersion increases as the nanoparticles in the bulk liquid achieve greater freedom. The electrostatic repulsion between the particles will be higher for particles with smaller size, giving a larger structural disjoining pressure. Also, when the amount of particles increases, the force working on the wedge film will increase. Wasan and Nikolov (2003) showed that the spreading behavior increased with decreasing the film thickness, that is, the number of particle layers in the film. The force will be at maximum at the tip of the wedge, see Figure 3.2.

When the structural disjoining pressure works on the vertex of the discontinuous phase, displacement occurs as the system tries to regain equilibrium. This force is related to the nanofluids ability to spread out on the surface of the rock due to imbalance of the interfacial forces between oil phase, aqueous phase and solid. The magnitude of this pressure depends on parameters such as particle size, particle volume fraction, polydispersity, temperature, salinity and rock properties. (Wasan and Nikolov, 2003; Zhang et al., 2014) Adding more electrolytes to the aqueous nanofluid will lower the disjoining pressure. Increasing salt concentration will lower the repulsive forces between nanoparticles and hence reduce the pressure that drives the wedge film. Because of this, an increase in salinity will have a negative effect on oil removal in the case of nanofluids. (Wasan and Nikolov, 2003)

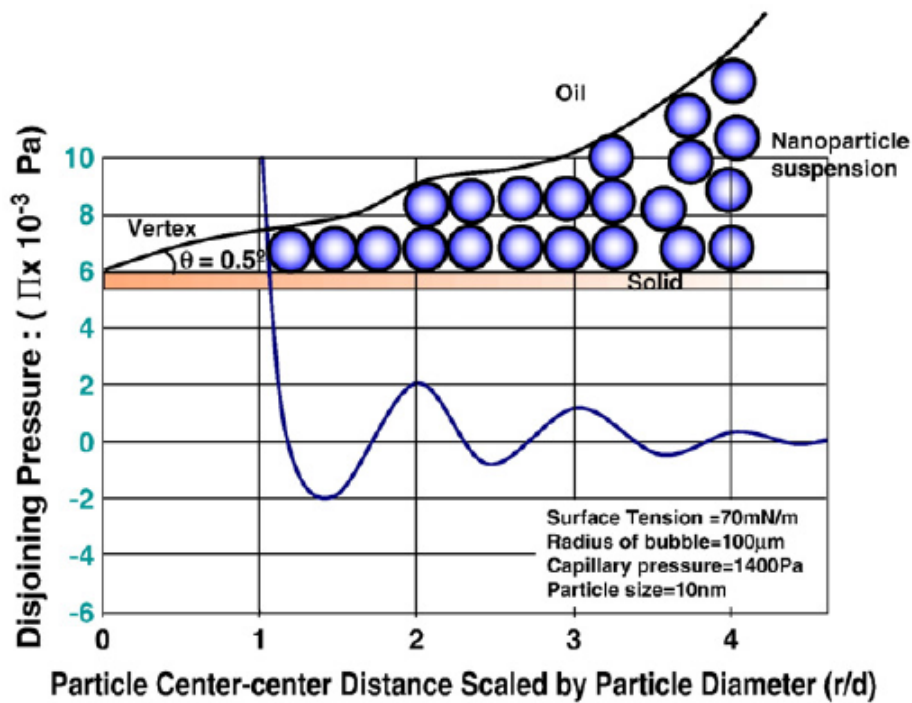


FIGURE 3.2: Disjoining pressure in the wedge structure. (Wasan and Nikolov, 2003)

3.2.2 Effect on Interfacial Tension

Oil and water are immiscible fluids, which means that the interfacial tension (IFT) between them is high. Introducing silica hydrophilic nanoparticles to the system has been observed to lower the IFT and potentially produce more oil. The nanoparticles will structure themselves at the oil/brine interface, reducing the contact between the two phases. The layer of particles generates a lower IFT between the two phases, much like surfactants work. The IFT tension is sensitive to nanofluid concentration; as the concentration increases, IFT decreases. (Li et al., 2013a; Dahle, 2013)

In this thesis hydrophilic silica is used to reduce oil/water IFT, but also neutral wetting particles would have an effect. Frijters et al. (2012) explained how the mechanisms behind the adsorption of neutral wetting particles work, and compares with surfactants. Surfactants adsorb at the interface due to their hydrophilic head and hydrophobic tail while neutral wetting nanoparticles adsorb because maintaining a particle-fluid interface requires less energy. Neutral wetting nanoparticles were

reported to change the interfacial free energy by taking away energetically expensive fluid-fluid interfaces and replaces them with a cheaper particle-fluid interface. This can be shown by the free energy term F_σ as a function of surface tension and droplet area (Frijters et al., 2012):

$$F_\sigma = \int_{\delta A} \sigma \delta A \quad (3.1)$$

The reduction of the interfacial free energy requires either (i) reduction of interfacial tension σ , which is achieved with adding surfactants, or (ii) reduce the area of integration, which is the effect of adsorbed particles. This shows that neutral wetting nanoparticles can reduce the overall interfacial free energy not by reducing the IFT itself, but by removing parts of the energetically unfavorable fluid-fluid interface area. For emulsions, assembly of particles on the oil droplet's surface is favorable because it blocks for destabilization by Ostwald ripening (larger droplets grows at the expense of small ones). It can also break up oil droplets (see Figure 3.3), making it easier for the emulsion to migrate through the porous media. (Frijters et al., 2012)

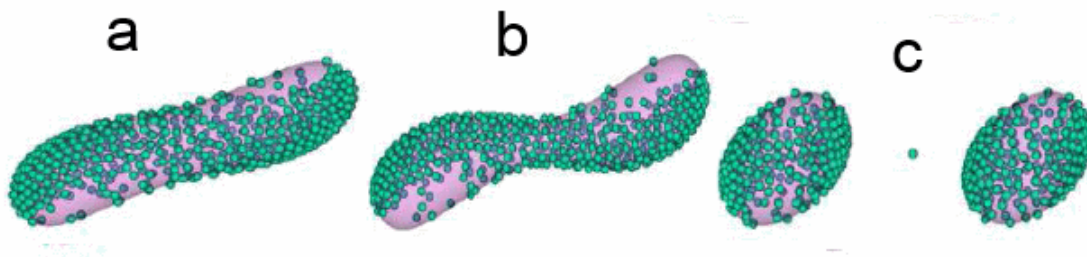


FIGURE 3.3: Breakup of oil droplets due to adsorption of nanoparticles. (Frijters et al., 2012)

3.2.3 Effect on Wettability

The ideal wetting preference of the rock for ultimate recovery is a much debated topic. Owens and Archer (1971) reported that oil recovery increased with increasing water-wetness. However, Morrow (1990) and Jadhunandan and Morrow (1995) reported increased recovery with decreasing water wetness. Even though there are

conflicting reports, the wettability is without doubt an important factor when it comes to oil recovery. [Li et al. \(2013b\)](#) reported increased water wetness using hydrophilic silica nanofluid and increased oil wetness using hydrophobic silica in neutral wet sandstones. This is a result of nanoparticles being driven by the aqueous bulk pressure and will spread along the solid surface and decrease the contact angle. Higher concentration of hydrophilic/hydrophobic nanoparticles will increase the wettability alteration in the core. Contact angle is the most universal measurement of the surfaces wettability.

[Vafaei et al. \(2006\)](#) showed that an increase in concentration of bismuth telluride nanoparticles increased the contact angle, until it reached a peak, where it decreased again. Their experiments also showed that the contact angle as a function of concentration was also dependent on particle size. For the same mass concentration, smaller particles caused larger variations in contact angle. The experiments indicates that nanoparticles suspended in fluids can be effective at manipulating the contact angle and interfacial tension.

3.2.4 Effect on Viscosity

Experiments have shown that adding high concentrations nanoparticles to water can increase the shear viscosity. Water molecules layered at the nanoparticle surface decreases the fraction of adjacent fluid molecules that are more mobile and hence increasing the shear viscosity. The viscosity can be increased by either increasing the nanoparticle concentration, or by increasing the size of the particles. ([Balasubramanian et al., 2011](#); [Shanker et al., 2012](#)) Another possibility is to mix polymers with nanoparticles, which will enhance the viscoelastic properties. ([Skauge et al., 2010](#))

Increasing the viscosity of water will decrease the mobility factor, M . The mobility factor is defined as the mobility of the displacing fluid compared to the displaced fluid. It's favorable to have a low value of M ; the lower the value, the better displacement efficiency. Values of $M \leq 1$ give a stable displacement (piston like) while higher values gives low displacement efficiency. The mobility factor is a function of viscosity and relative permeability of the displacing fluid compared to the displaced fluid:

$$M = \frac{k_{rw}}{\mu_w} * \frac{\mu_o}{k_{ro}} \quad (3.2)$$

where k_r is the relative permeability and μ is the viscosity of the respective fluids.

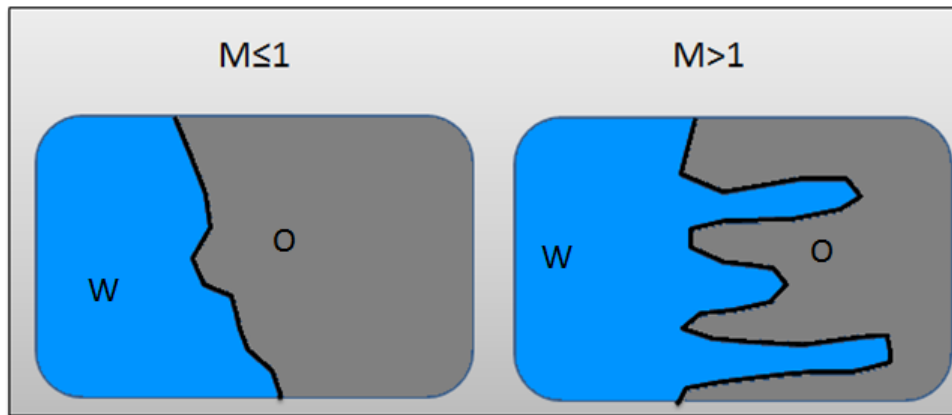


FIGURE 3.4: Effect of viscosity and relative permeability on displacement.

Suleimanov et al. (2011) showed that if a small amount of a non-ferrous nanoparticles was added to surfactant solutions, the viscosity would increase significantly. In addition the nanoparticles enhanced the surfactants in terms of stability and IFT reduction. Skauge et al. (2010) reported an increase in viscosity of the nanofluid with polymer additives, which could be useful for better sweep efficiency. This indicates that nanoparticles can be used to enhance polymers and surfactants in addition to increase stability, letting them migrate further into the reservoir.

3.2.5 Retention of Nanoparticles in Porous Media

Coreflooding experiments (Li et al., 2013a,b) have shown that nanofluids have a tendency to reduce the porosity and permeability of a porous rock. Nanoparticles are transported through a porous media through diffusion, convection and hydrodynamics. During the early stage of flooding, adsorption and desorption of nanoparticles will occur at the pore wall. (Li et al., 2013b) It is the combined force of van der Waals forces, repulsion between electrical double layers (EDL), Born repulsion, acid-base interaction, and hydrodynamics. (Khilar and Fogler, 1998) This is a dynamic balancing process which will eventually reach equilibrium state, where nanofluid can travel through the pore system without too much adsorption and diffusion.

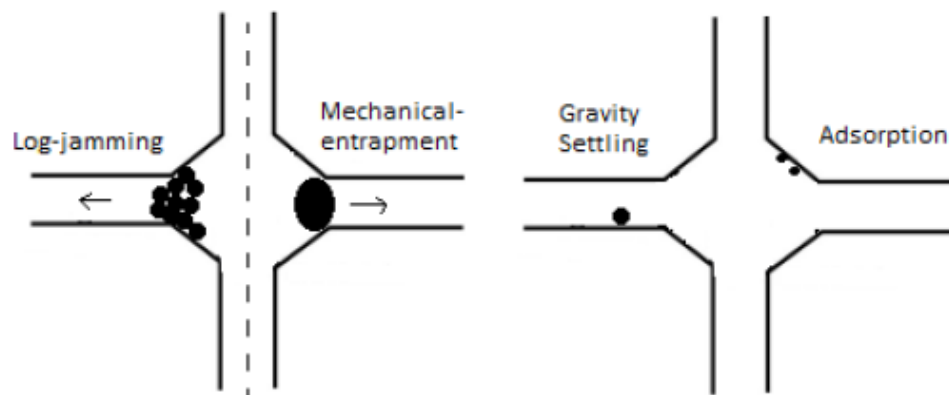


FIGURE 3.5: The four different mechanisms of retention. (Engeset, 2013)

Migration and retention of solid particles in porous media is a complex process governed by factors such as particle size and shape and the flow rate, chemistry of the carrying fluid and concentration suspended particles. (Todd et al., 1984; Vetter et al., 1987; Moghadasi et al., 2004; Yu et al., 2010) Four different mechanisms can lead to formation damage (Civan, 2000; Gao, 2008): (1) adsorption due to particles Brownian motion and their electrostatic interactions with the surface of the porous rock, (2) mechanical entrapment where the size of the particle is larger than pore throat, (3) sedimentation or gravity settling when the densities of moving particles and carrying fluid are very different and (4) log-jamming where particles move at lower velocities compared to the carrying fluid and accumulate at the pore throats, which eventually leads to blockage. Adsorption of nanoparticles occur on the stationary grain surface of the reservoir rock, but also on interfaces between oil and water. Note that pore throats are usually significantly larger than nanoparticle sizes, meaning very few particles suffer from mechanical entrapment. (Zhang et al., 2013) Temperature has been reported to have a marginal effect, with two percent points greater retention at 80°C compared to 21°C. (Caldelas et al., 2011) Existence of salt ions in the carrying fluid has been observed to dramatically delay nanoparticle breakthrough time and increase retention. (Yu et al., 2010)

Chapter 4

Experimental Setup

The purpose of this chapter is to give an overview of the laboratory experiment performed in this project. The overview includes the materials, the apparatus and an introduction on how they work. All the experiments were conducted at the Institute of Petroleum Technology and Applied Geophysics at NTNU.

4.1 Preparation of Core Samples

All flooding experiments were performed with Berea Sandstone Cores from Ohio, USA. Berea Sandstone is a sedimentary rock mainly composed of quartz held together by silica. The relatively high porosity and permeability makes it a good representation of a typical reservoir rock. ([Berea Sandstone Cores](#)) The cores are taken from two different blocks, meaning the cores will have two sets of properties. The cores taken from the high permeability block will be noted with "H", and the cores taken from the medium permeability block will be noted with "M". Cores noted with "9" are from the medium permeability block.

4.1.1 Cleaning of Cores

A soxhlet extraction is the most common method for cleaning core samples. As seen in Figure 4.1, methanol is heated to the boiling point of $65^{\circ}C$. The vapor will move upwards through the core, and into the condenser where cold circulating water will condense the vapor. The re-condensed methanol will drip into the core

$$V_2 = \frac{(p - p_1)V_1}{p_2 - p} \quad (4.1)$$

where p_1 and p_2 is the initial pressure in the reference cell and sample chamber respectively, and p is the equilibrium pressure after opening the valve. The grain volume V_g of each core plug is determined by the volume difference of the empty reference cell, V_1 , and the sample chamber with the core plug, V_2 . The volumes can be read directly from the scale, and the effective porosity can easily be calculated:

$$\phi_e = \frac{V_p}{V_b} = \frac{V_b - V_g}{V_b} = \frac{V_b - (V_1 - V_2)}{V_b} \quad (4.2)$$

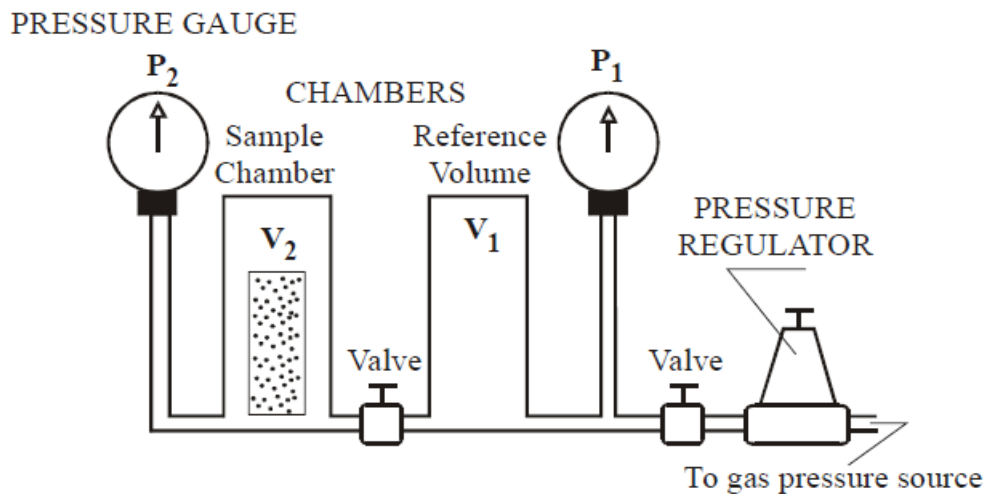


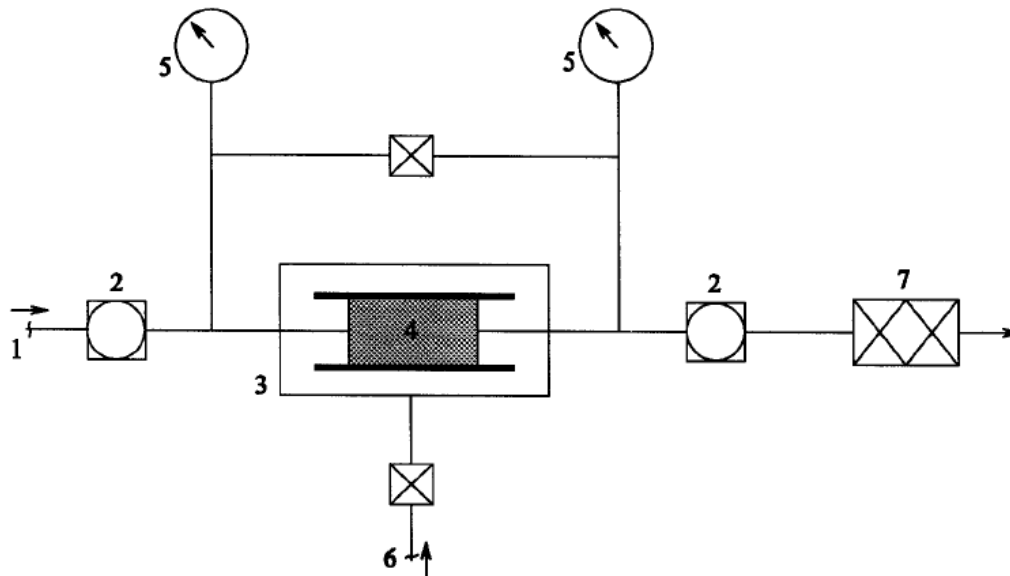
FIGURE 4.2: Helium porosimeter apparatus. (Torsæter and Abtahi, 2000)

Using the helium porosimeter has several advantages compared to other methods (Torsæter and Abtahi, 2000):

- Helium particles are small and can easily penetrate small pores.
- It is an inert gas and does not adsorb on rock surfaces as air may do.
- Helium can be considered as an ideal gas ($z = 1$) for pressures and temperatures usually employed in the test.
- Helium has high diffusivity and therefore affords a useful means of determining porosity of low permeability rocks.

4.1.3 Permeability Measurement

A constant head permeameter as seen in Figure 4.3 were used to measure permeability of each core plug. This is one of the most common methods for permeability testing, using dry air as flowing fluid. The air has the advantages of rapidly reaching steady state, it will not alter rock minerals and it's easy to obtain 100% fluid saturation.



- | | |
|----------------------------|---|
| 1. Air supply | 5. Manometers |
| 2. Reduction valves | 6. Sleeve pressure |
| 3. Core holder | 7. Wet-test meter (gas-volume measurement) |
| 4. Core sample | |

FIGURE 4.3: Constant Head Permeameter. (Torsæter and Abtahi, 2000)

A clean and dry core is placed inside a Hassler core holder with a confining pressure of 20 bar. Inlet and outlet pressures are measured by gauges at both sides of the core. The airflow is measured at the outlet, and will vary with pressure. Different flow velocities but with the same total pressure drop were tested, and gas permeability were calculated using following equation:

$$k = \frac{Q_{atm} \mu L^2 P_{atm}}{A(P_1^2 - P_2^2)} \quad (4.3)$$

where k is the gas permeability across a core with length L and cross section A . With a pressure drop of $P_1 - P_2$ the air with viscosity μ will flow at a mass rate

of Q_{atm} . By measuring flow rate at different pressures and plot against average pressure $1/P_m$ across the core, Klinkenberg corrections could be obtained. These plots are used to find liquid permeability using values from air/gas measurements.

4.1.4 Saturation Cores with Brine

The cores were saturated with a 3 wt% NaCl brine, using a vacuum pump. The setup for the procedure can be seen in Figure 4.4. The cores were placed in a beaker inside the vacuum tank and sealed off, making an isolated system. A vacuum pump creates an under-pressure of approximately 100 mbar inside the tank to extract all fluids from the system. Lastly the valve to the pump was closed and the valves to the brine opened. When the cores were completely covered in brine they were left soaking for one hour to saturate.

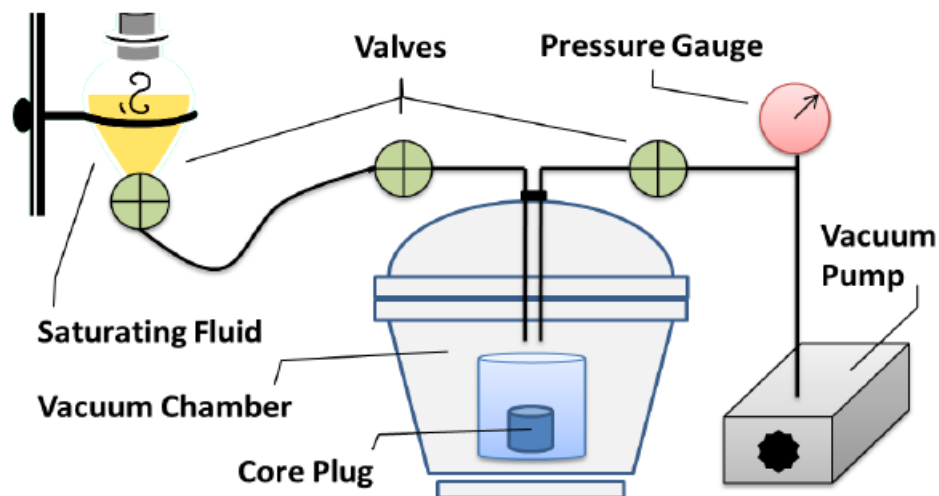


FIGURE 4.4: Vacuum pump setup. (Kaasa, 2013)

4.1.5 XRD-Analysis

Samples from the Berea Sandstone cores were sent to the Department of Geology and Mineral Resources Engineering at Norwegian University of Science and Technology for X-Ray Diffraction (XRD) analysis. This is a common technique used for analyzing mineral and crystalline materials in rocks. The rock core samples are grounded to fine powder and the X-rays are directed onto the sample. The reflections are used to identify specific materials, which gives the waves unique

characteristic patterns. Five different samples were taken from each block in order to get an accurate measurement of the mineral composition.

4.2 Fluid Properties

The fluids used in the experiments were heavy oil, brine and nanofluids. Certain properties of the fluids were needed as input parameters for experiments measuring interfacial tension and contact angle.

4.2.1 Brine

A synthetic North Sea brine (NSB) was used for both flooding and as a dispersing agent for the nanofluids. The composition of the brine is shown in the table below, and was made from a recipe provided by Evonik. The salt content features a typical brine in the North Sea. To ensure that all the salts were fully dissolved, a magnetic pin were used to stir the solution for 3-4 hours.

TABLE 4.1: Composition of the North Sea brine.

Salt	Mass g/L	Concentration wt%
<i>NaCl</i>	28,5	2,77
<i>NaHCO₃</i>	0,22	0,02
<i>Na₂SO₄</i>	4,066	0,39
<i>CaCl₂x2H₂O</i>	1,625	0,16
<i>MgCl₂x6H₂O</i>	3,162	0,31
<i>SrCl₂x6H₂O</i>	0,024	0,00
<i>KCl</i>	0,721	0,07
Total	38,318	3,72

4.2.2 Nanoparticles

A total of six different types of nanoparticles were tested in the experiments. Evonik Industries provided nanofluids with concentrations of 20 wt % nanoparticles

dispersed in DI water. All the nanofluids contained a sodium hydroxide stabilizing agent, except for the IDISIL EM 7520 K which contained a potassium based stabilizer. Preparing a nanofluid for the experiments only required diluting the high concentrated solution with the wanted dispersion agent (brine). The full list of nanoparticles can be found in Table 4.2. More data can be found in Appendix B with all relevant properties. All the silicas are hydrophilic, produced and surface treated by Evonik Industries. Two of the particles have a unknown particle diameter, but according to Evonik, it should be larger than 7 nm and lower than 16 nm. Thus they will from this point on be called medium sized.

TABLE 4.2: Nanoparticles used in making the nanofluids.

Fluid Name	Type of Particle	Avg. primary particle D [nm]	Surface Area [m ² /g]
AERODISP W 7620 N	Fumed Silica	7	300
AERODISP W 7320 N	Fumed Silica	16	130
VP Disp W 3520 XN	Fumed Silica	-	-
IDISIL IC 0820	Colloidal Silica	8	350
IDISIL SI 1520	Colloidal Silica	15	150
IDISIL EM 7520 K	Colloidal Silica	-	65

A colloidal state is a subdivision where dispersed particles are sufficiently small ($\leq 100nm$) to not be affected by gravity forces, but sufficiently large ($\geq 1nm$) to deviate from true solutions. Typically the colloidal particles have a spherical shape as opposed to fumed silica, which are fused, chain-like structures. Both types have the property of high surface area in common, as a result of their small size. The smaller the particle diameter, the higher the surface area. Based on the data provided by Evonik, the colloidal and fumed silica differs from each other when it comes to the size of the aggregations. While the colloidal particles forms aggregations of around twice the size of a normal particles, the fumed types can aggregate to more than 10 times the original particle size.

4.2.3 Nanofluids

Nanofluids for the flooding experiments were prepared by diluting the highly concentrated nanosuspensions with a dispersion agent, in this case brine. The

suspensions were diluted to a concentration of 0,05 wt % nanoparticles for initial testing, based on recommendations from earlier studies. (Hendraningrat et al., 2013b,c,e) Nanofluids of 0,025 and 0,075 wt% were also prepared for testing the effect of varying concentrations.

It was observed that the best procedure for preparing a nanofluid was to firstly dilute with a small dose of DI water, before adding any brine. This ensured that the nanoparticles remained properly dispersed. When adding brine directly into the high concentrated suspension from Evonik, severe instability and precipitations occurred. The "snowy" content in Figure 4.5 is precipitated nanoparticles. The brine used for diluting is the synthetic North Sea brine mentioned earlier.



FIGURE 4.5: Precipitation of nanoparticles.

4.2.4 Crude Oil

A degassed crude oil from the North Sea was used for all the experiments. The properties of the oil (Crude Oil A) were analyzed by Tichelkamp et al. (2014) and given in the table below:

TABLE 4.3: Properties of the oil sample used. (Tichelkamp et al., 2014)

Temperature $^{\circ}C$	Density g/cm^3	Viscosity cP
15	0,8582	-
20	0,8560 ¹	19,90
60	0,8252	4,07

4.2.5 Densities and Viscosities

To measure viscosity of the fluids, a rotating viscometer was used. Viscosity varies with temperature as shown in Section 2.2.2. It is therefore important to perform the experiment with a consistent temperature. All the measurements were performed at room temperature ($21-23^{\circ}C$) A cylinder connected to a spring were placed in the liquid rotating at a constant velocity. The rotational reflection of the cylinder will be a measure of the liquid viscosity.

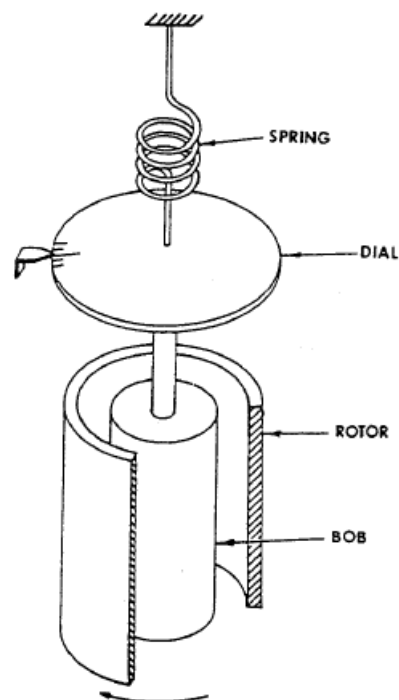


FIGURE 4.6: Rotating viscometer. (Torsæter and Abtahi, 2000)

¹Measured by the author of this thesis.

The advantages with using the rotating viscometer to measure viscosity is that it can be used for a wide range of viscosities and that the experiment can be conducted without temperature change, using a thermocell to regulate for temperature changes.

The pycnometer was used to measure both the oil and the water density. This is an accurately made flask that can be filled with a known volume of fluid. Weighting the flask before and after adding the fluid gave the weight of the fluid. Knowing this, the density was calculated as mass over volume:

$$\rho_f = \frac{m}{V} \quad (4.4)$$

The advantages with this method is that it is easy to perform and accurate, as any air will be forced out of the flask when applying a stopper to the bottleneck.

4.2.6 Interfacial Tension and Contact Angle

The spinning drop method was used to measure the interfacial tension. The basic concept is that a droplet of a less dense fluid (oil) is injected into a container of the denser fluid (brine), and the whole system is rotated. This process results in a centrifugal field where the drop gets an elongated shape in the axial direction of the rotation. (Torsæter and Abtahi, 2000) As the drop elongates the interfacial tension will oppose the deformation and the system will reach an equilibrium. If no interfacial tension had been present, the droplet would continue to elongate indefinitely. As the length of the drop gets large compared to the radius, it can be treated as a circular cylinder with hemispherical ends.

Viades-Trejo and Gracia-Fadrique (2007) showed that the Young-Laplace equation (LY) can be used to calculate the IFT from the spinning drop method. This equation applies for both spherical and non-spherical shapes, and can be used in absence or influence of an external field (like gravity). In the case of spinning drop method the rotational acceleration is usually so much higher than the gravity acceleration that the latter is negligible. The Young-Laplace equation for calculating interfacial tension σ in a centrifugal field where $\omega \rightarrow \infty$ and a cylindrical shaped oil droplet is given by:

$$\sigma = \Delta\rho\omega^2 R^3(n-1)^2\left(\frac{n}{2-n}\right) \quad (4.5)$$

where n is the refractive index of the heavy fluid (brine/nanofluid), ω is the angular velocity, $\Delta\rho$ is the density difference of the two fluids and R is the radius of the oil droplet.

The refractive index was measured for the aqueous phases using the refractometer Mettler Toledo Refracto 30GS. As seen in Table 4.4, the refractive index increases slightly with salts and nanoparticles present in the dispersion. The index difference between the different nanofluids are very low, and might be due to small (room) temperature variations. The refractive index is a dimensionless parameter that describes how light and other types of radiation propagates through the medium compared to the propagation in vacuum.

TABLE 4.4: Refractive Index based on aqueous phases.

Fluid	Refractive Index (n)
Deionized water	1,3310
North Sea Brine	1,3390
AERODISP W 7620 N	1,3389
AERODISP W 7320 N	1,3389
IDISIL IC 0820	1,3386
IDISIL SI 1520	1,3393
VP Disp W 3520 XN	1,3389
IDISIL EM 7520 K	1,3394

One of the main advantages of the spinning drop method for measuring interfacial tension is that the surface of the droplet is closed and any inaccuracy regarding the contact angle is removed. (Vonnegut, 1942) This is often problematic when using other methods like capillary rise or Whilhelmy plate, especially for low interfacial tensions.

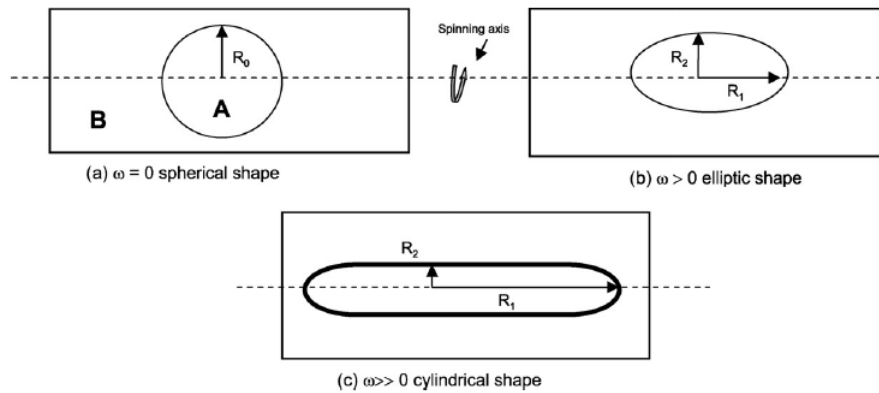


FIGURE 4.7: The spinning drop method. (Viades-Trejo and Gracia-Fadrique, 2007)

The same oil sample and the same temperature ($T = 22, 8^{\circ}C$) were used for all experiments to ensure consistent results. A refrigerating and heating circulation system (Jubalo F-12-ED) were used to maintain an isothermal state ($\Delta T = 0$). Rotation speed was kept between 4000-6000 rpm, depending on the size of the oil droplet. A spinning drop video tensiometer (SVT20) recorded how the shape of the oil droplet changed over time, calculating the IFT based on input data of fluid densities and refraction index.

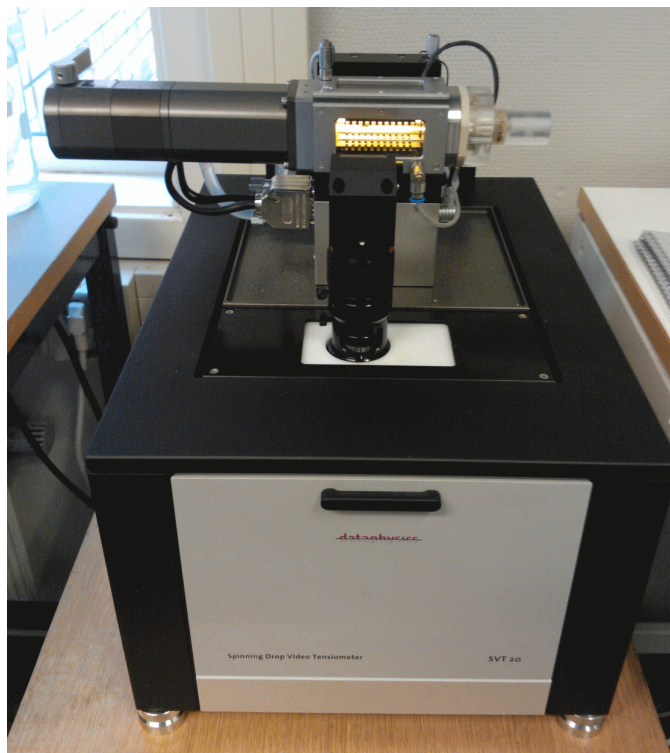


FIGURE 4.8: The spinning drop video tensiometer.

To measure the contact angle an imaging method was used. A small oil droplet was placed on a smooth glass plate and immersed in a brine/nanofluid filled transparent cell. Using the Goniometry KSV CAM instrument enlarged images of the droplet were obtained by photographing. The dimensions of the drop image can be used to calculate the contact angle of the system. (Torsæter and Abtahi, 2000) Measurements were taken every 10 minutes for up to 10 hours or until the angle stabilized. For each image a baseline had to be placed manually between the solid surface and the oil drop. This made it possible for the software to recognize the drop and find contact angles at both sides of the drop. The experiment was conducted at ambient conditions.

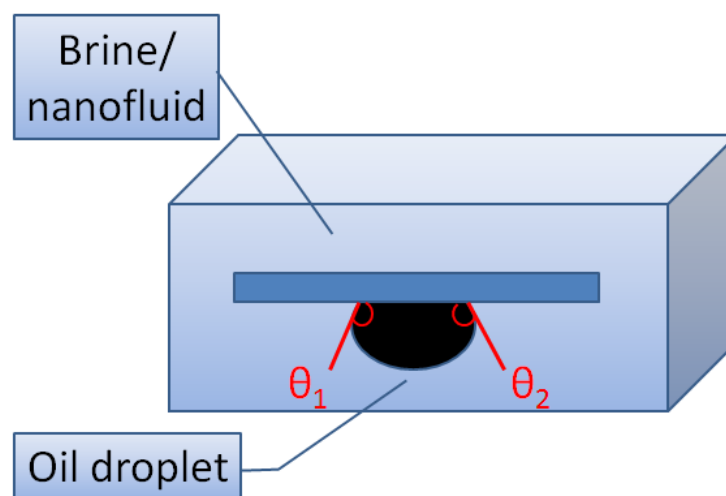


FIGURE 4.9: Imaging method for contact angle measurement.

4.3 Coreflood setup

The aim of this experiment was to investigate how hydrocarbon recovery varied with changing core permeability and nanoparticle size, morphology and concentration. The best way to test this was through coreflooding experiments. The coreflood setup consists of three different vessels, filled up with either brine, crude oil or nanofluid. Each of the vessels had valves on the inlets and outlets in order to regulate the fluid flow. A high precision pump (Pharmacia LKB pump P-500) was used to inject exxsol D-60 into one of the vessels at the time, pushing a piston plate inside. The piston pushes out the liquid inside the vessel, and at the same time works as a separation between the liquid and the exxsol D-60. As seen from the schematics of the coreflood setup in Figure 4.10, all the vessels were connected to a

flowline going to the Hassler core holder. A significant pressure drop was observed when changing from one vessel to another as the fluid kept flowing due to high pressure drop across the system. In order to prevent this, a valve was installed just before the core holder and was closed during the downtime spent switching vessel.

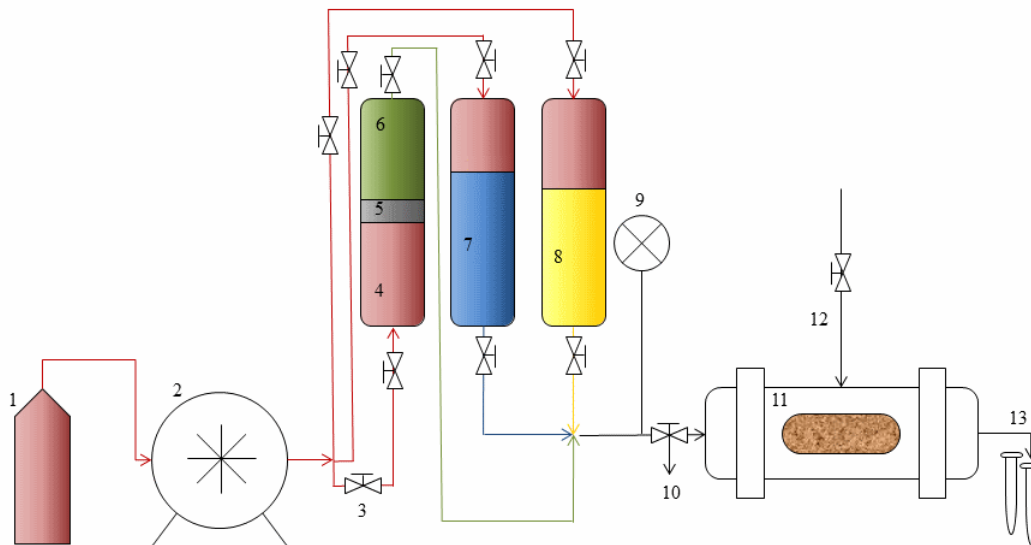


FIGURE 4.10: Experimental setup of the core flooding apparatus. 1) Exxsol D60 pump fluid, 2) pump, 3) valves, 4) Exxsol D60 displacing reservoir fluid, 5) piston to separate the oils, 6) crude oil, 7) NSB, 8) nanofluid, 9) pressure gauge, 10) bypass valve, 11) Hassler cell holder with core, 12) sleeve pressure, 13) effluent into test tubes. (Aurand et al., 2014)

A confining pressure of 16-20 bar was applied in the core holder to ensure that no fluid flow could occur in the space between the sleeve and the core sample. All the experiments were performed at ambient conditions and a constant injection rate of 0,4 mL/min. A pressure gauge at the inlet was used to measure the differential pressure (ΔP) across the core holder. Measurements were taken every 5 minutes, and were continued for all the flooding phases. Making differential pressure vs. time plots were in important in order to investigate retention of nanoparticles in the core plug. An increasing pressure during the nanofluid flooding would indicate that the permeability had been reduced.

4.4 Coreflood Scheme

The cores were initially saturated with 100% brine. Thus the flooding experiments had to start with a primary drainage process. Oil was injected into the core plugs at 0,4 mL/min until no more brine was produced, usually after 2-3 pore volumes injected. This procedure established the initial water saturation, S_{wi} .

The next stage was the water flooding, where synthetic North Sea brine was injected into the core plugs at 0,4 mL/min until no more oil was produced. This would establish the residual oil saturation, S_{or} . Nanofluid flooding was initiated as a tertiary recovery process. Six different nanoparticles were used with varying size and morphology. A full list can be found in Chapter 4.2.2. To investigate if they had any effect on the oil recovery, they were injected into the core plug after the water flooding. Any additional oil produced during the tertiary process would increase the recovery factor and hence prove that nanoparticles potentially can work as an EOR agent. As there were no automated way to measure the recovery, the experiment had to be watched over during the whole flooding sequence. Samples of the effluent fluids were manually taken every 5 minutes at the outlet of the core holder. The samples were used to measure the amount of oil and brine produced, and used for calculating saturations as well as recovery factor. Each flooding experiment took 6-9 hours.

Chapter 5

Experimental Results

The results presented in this chapter were provided using the experimental procedures explained in Chapter 4. The purpose of these experiments was to determine the optimal nanoparticle size, morphology and concentration for enhanced oil recovery. All data is given in the Appendixes.

5.1 Core Properties

A total of 22 core flooding experiments were performed. A summary of which nanofluid is used in which core is given in Table 5.1. As the cores can have different properties, it is important to know which core is used for which experiment. The bottom four rows in the table are validation tests, used to confirm the results from the previous flooding experiments. Due to insufficient time, not all the nanofluids were tested a second time.

TABLE 5.1: Core flooding test summary.

	Nanofluid ¹	Core	
Test 1 - 0,05% concentration	AERODISP W 7620 N	7M	
	AERODISP W 7320 N	6M	
	VP Disp W 3520 XN	4M	
	IDISIL IC 0820	3M	
	IDISIL SI 1520	1M	
	IDISIL EM 7520 K	5M	
	AERODISP W 7620 N	5H	
	AERODISP W 7320 N	1H	
	VP Disp W 3520 XN	2H	
	IDISIL IC 0820	4H	
	IDISIL SI 1520	6H	
	IDISIL EM 7520 K	8H	
	Concentration tests	AERODISP W 7620 N - 0,025 wt%	9-3
		AERODISP W 7620 N - 0,075 wt%	9-2
VP Disp 3520 XN - 0,025 wt%		9-4	
VP Disp 3520 XN - 0,075 wt%		9-5	
AERODISP W 7320 N - 0,025 wt%		9-1	
AERODISP W 7320 N - 0,075 wt%		8M	
Validation tests	AERODISP W 7320 N	9-7	
	AERODISP W 7620 N	9-8	
	VP Disp W 3520 XN	9-6	
	AERODISP W 7320 N ²	7H	

5.1.1 Porosity and Permeability

In Figure 5.1 to 5.3 the porosity (dark gray) and permeability (light gray) are presented for all the 28 cores used. Core dimensions, weights, permeability measurements and Klinkenberg plots are given in Appendix A. The cores are classified according to the block they were cut from. The "H" plugs are from a high permeability block and the "M" and "9" plugs from a medium permeability block. It has to be noted that there are some variations within each block. For example, some plugs from the M block has higher permeability than the lower H cores.

¹0,05 wt% concentration unless otherwise stated.

²The core holder sleeve was replaced before this test.

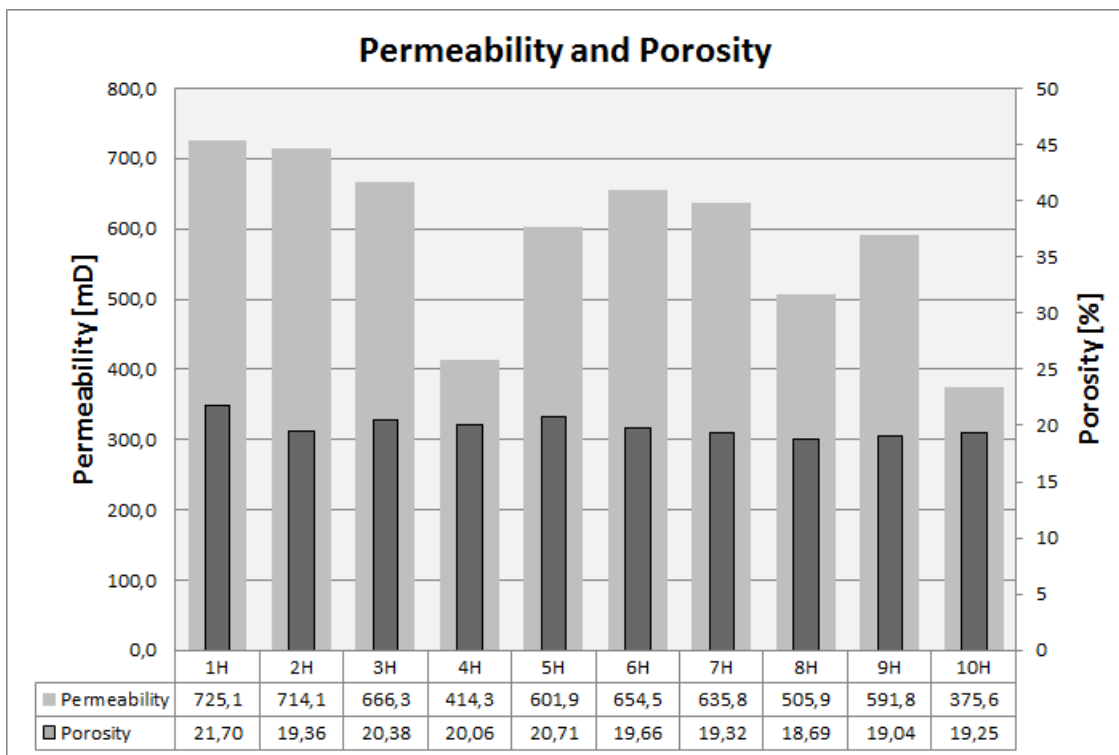


FIGURE 5.1: Graphical presentation of porosity and permeability of the high permeability cores.

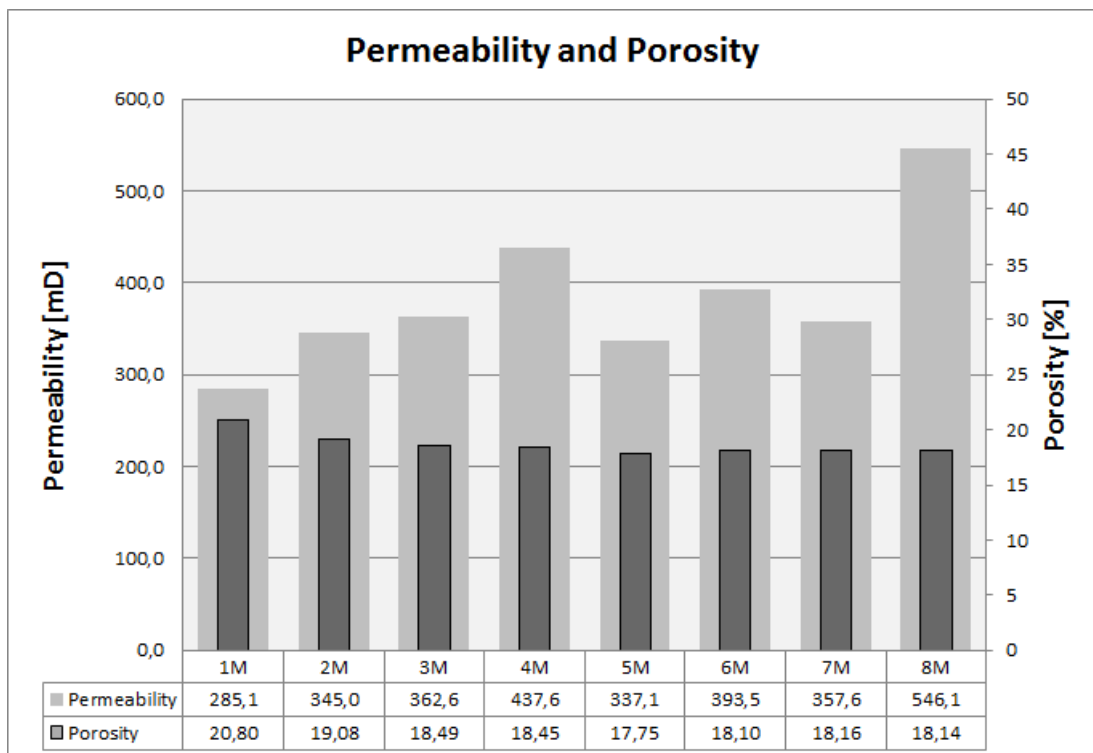


FIGURE 5.2: Graphical presentation of porosity and permeability of the medium permeability cores.

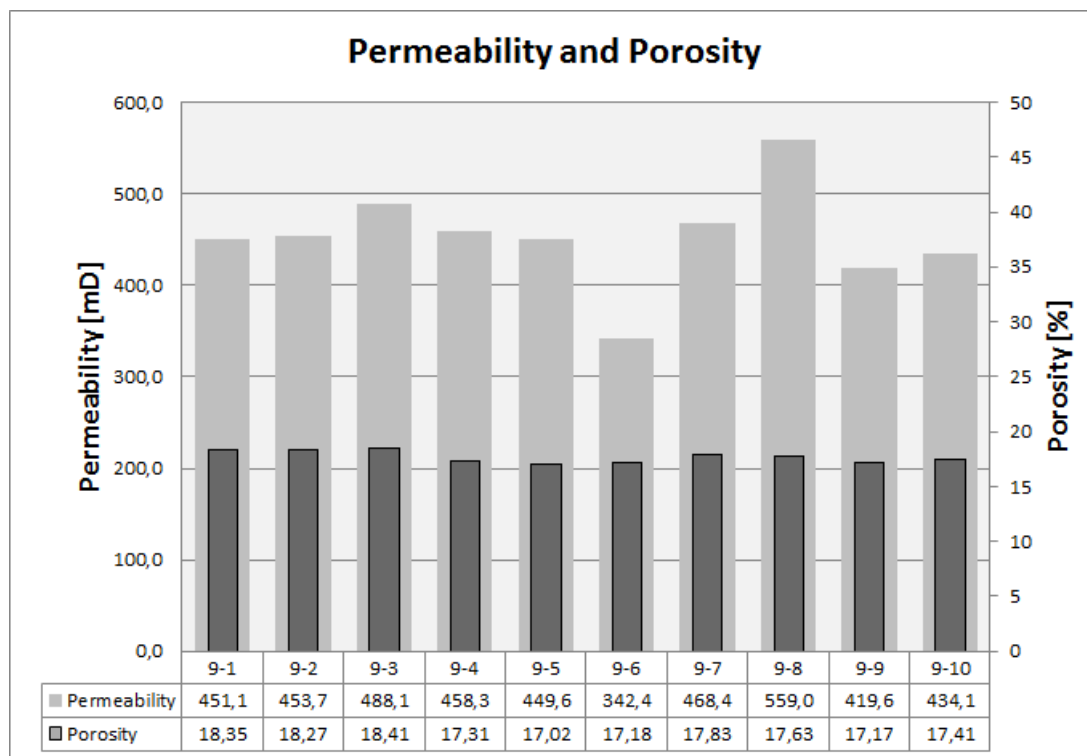


FIGURE 5.3: Graphical presentation of porosity and permeability of the cores from block 9.

The porosity of the cores varies from 17,02 % to 21,7 %. The porosity readings from each individual block is very similar. As Berea sandstone is quite homogeneous, this is to be expected. The few deviations are likely due to inaccurate dimension measurements of the cores, or inaccurate readings from the helium porosimeter scale.

The permeability of the cores are ranging from 285 mD to 725 mD. Generally, the highest permeabilities are found in the cores from the H block and the lowest permeabilities in the cores from the M and 9 cores. The permeability of Berea sandstones varies mostly with the mechanical structure of the rock and the grain size. Large variations in permeabilities from cores of the same block are most likely due to inaccurate measurements of the core dimensions. Furthermore, the air permeability measurements are very sensitive even to small adjustments in the differential pressure across the cores. Lastly, it's assumed that the cores are drilled in the same longitudinal direction. If not, the permeability might vary significantly as it is a directional property and will vary according to fluids flow direction. (Zolotukhin and Ursin, 2000)

The cores from block H and M were used to make base-case flooding experiments, testing different types of nanoparticles at both high and medium permeability. The cores from block 9 were used to make concentration tests and confirming the results from the M core floodings.

5.1.2 XRD-Analysis

An XRD Analysis was performed to characterize the mineral contents of the rock samples used in the experiments. The cores were taken from two different blocks of Berea Sandstone, resulting in slightly different compositions. Mineral analysis should always be performed before corefloodings, as the cores might contain clay. Several types of clay can be present in a typical sandstone reservoir such as kaolinite, smectite, illite and clorite. Some of them are reactive and will swell in contact with fresh water or high concentration of sodium cations (Lake, 1989), which will induce a porosity/permeability impairment. Five samples were taken from each block, and the mineral content is given in Table 5.2.

TABLE 5.2: XRD analysis of the cores.

Block	Quartz %	Microline %	Diopside %	Kaolinite %
H	97,31	2,45	0	0,24
M	93,72	4,99	1,29	0

The XRD analysis shows that the cores consists of mainly quartz and microline. The medium permeability cores had no measurable clay content, while the high permeability cores had traces of kaolinite clay. This is a well-known none swelling clay, and will have no impact on the porosity/permeability during the flooding experiments.

5.2 Viscosity and Density Measurements

For making contact angle and IFT measurements relevant liquid properties were needed. The measurements were performed at room temperature, ranging from ca. 20°C to 23°C. The properties of the oil were already analyzed by Tichelkamp et al. (2014) and given in Table 4.3.

A pycnometer was used for density measurements, and a rotating viscometer was used for measuring the viscosities. A summary of the fluid properties is given in Table 5.3. Due to the low concentration of nanoparticles, the properties of all the nanofluids were similar to the brine.

TABLE 5.3: Density and viscosity at the given temperature.

Liquid	Density g/cm ³	Viscosity cP	Temperature °C
North Sea Brine	1,022	1,08	22,8
AERODISP W 7620 N	1,022	0,94	22,8
VP Disp W 3520 XN	1,025	0,97	22,8
AERODISP W 7320 N	1,025	1,02	22,8
IDISIL IC 0820	1,023	0,97	22,8
IDISIL SI 1520	1,025	1,02	20,1
IDISIL EM 7520 K	1,023	0,91	20,4

Difficulties in getting the rotating viscometer to stabilize may have affected the resulting viscosities slightly. As for the densities, the accuracy of the scale used to weight the pycnometer is important.

5.3 Contact Angle

The contact angle of an oil droplet on a glass plate submerged in nanofluid was measured in order to investigate how nanoparticles affect the wettability. A summary is given in Table 5.4. All the measurements can be found in Appendix B. The experiment was conducted at ambient conditions. An increase in contact angle compared to brine means that the surface has become more water wet. Introducing nanoparticles to the system increased the contact angle, indicating that the particles have potential to alter the wettability of a reservoir rock. The medium colloidal particles were unstable and precipitated after a few hours. Thus the contact angle for this nanofluid was not measured.

TABLE 5.4: Contact angle measurements.

Liquid	Particle Type-Size	Contact angle
North Sea Brine	-	153,4
AERODISP W 7620 N	Fumed - Small	158,4
VP Disp W 3520 XN	Fumed - Medium	160,6
AERODISP W 7320 N	Fumed - Large	158,4
IDISIL IC 0820	Colloidal - Small	167,9
IDISIL SI 1520	Colloidal - Large	150,0
IDISIL EM 7520 K	Colloidal - Medium	-

5.4 Interfacial Tension

Interfacial tension measurements were performed using the spinning drop method. All experiments were conducted at room temperature (22,8°C), where a heating/-cooling system made sure that the temperature variations were kept to a minimum. Brine or nanofluid were surrounding a small oil droplet in a glass tube and rotated, as explained in Chapter 4.2.6. The experiment was stopped once the measurement stabilized. The IFT between oil and various nanofluids at 0,05 wt% is shown in Figure 5.4. A base case using the North Sea Brine and oil is also shown for comparison.

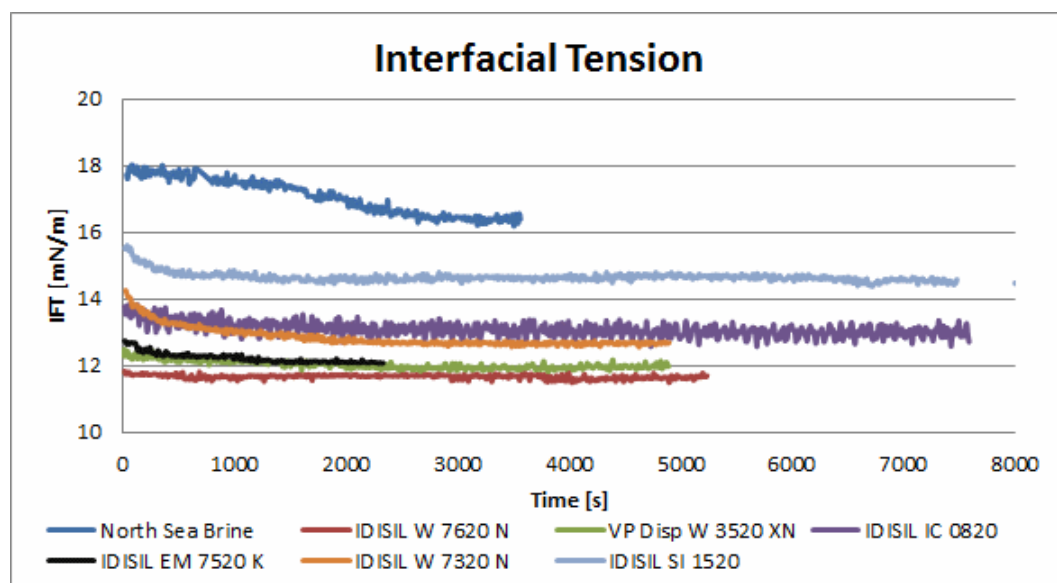


FIGURE 5.4: IFT between oil and different nanofluids at 0,05 wt%.

TABLE 5.5: Interfacial Tension and percentage reduction compared to brine. All nanofluids have a 0,05 wt% concentration.

Fluid	Particle Type	IFT mN/m	Percent Reduction %
Brine		16,41	-
AERODISP W 7620 N	Small Fumed	11,65	29,02%
VP Disp W 3520 XN	Medium Fumed	11,96	27,13%
AERODISP W 7320 N	Large Fumed	12,67	22,75%
IDISIL IC 0820	Small Colloidal	12,99	20,81%
IDISIL EM-7520 K	Medium Colloidal	12,15	25,93%
IDISIL SI 1520	Large Colloidal	14,52	11,53%

All the nanofluids proved to be useful for reducing the tension between oil and brine. A summary is given in Table 5.5, where the nanofluids are compared to the brine. The fumed silica showed the highest potential for reducing IFT. A trend was observed where the IFT decreased as nanoparticle size decreased. The smallest fumed particle gave a 29 % reduction compared to brine, while the largest provided a 23 % reduction. The colloidal silica showed more unstable results with the medium sized particles giving the largest reduction of 26 %. The large colloidal silica was the worst in terms of lowering the IFT, with a 11,5 % decrease.

5.4.1 IFT at Different Concentrations

Based on the coreflood experiments, the three most promising nanofluids (the fumed silicas) were selected for testing at different concentrations. The IFT for each of these nanofluids were tested at concentrations of 0,025 wt%, 0,05 wt% and 0,075 wt%. The results can be seen in Figure 5.5, 5.6 and 5.7. The general trend was a larger reduction in IFT at higher concentrations, although the large and small sized particles provided the largest IFT reduction at 0,05 wt% followed by the 0,075 wt% concentration. AERODISP W 7320 N gave almost identical IFT at all the concentrations tested.

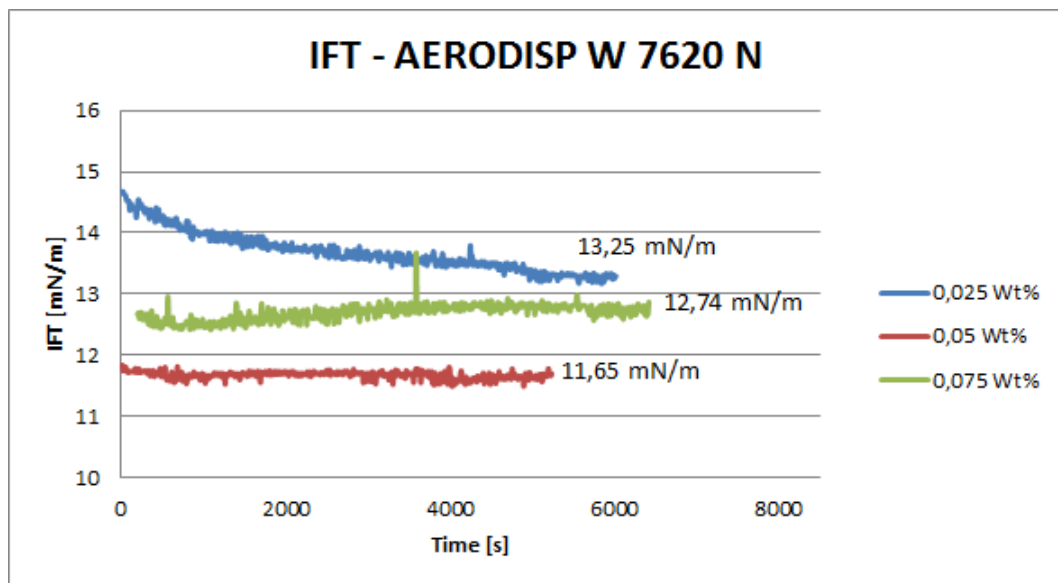


FIGURE 5.5: IFT between oil and AERODISP W 7620 N (small particles).

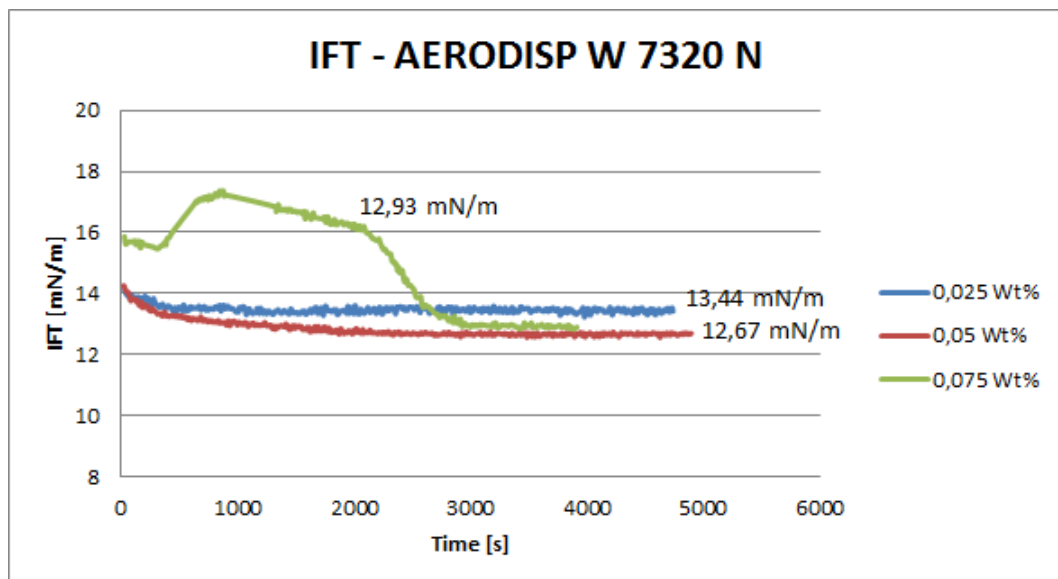


FIGURE 5.6: IFT between oil and AERODISP W 7320 N (large particles).

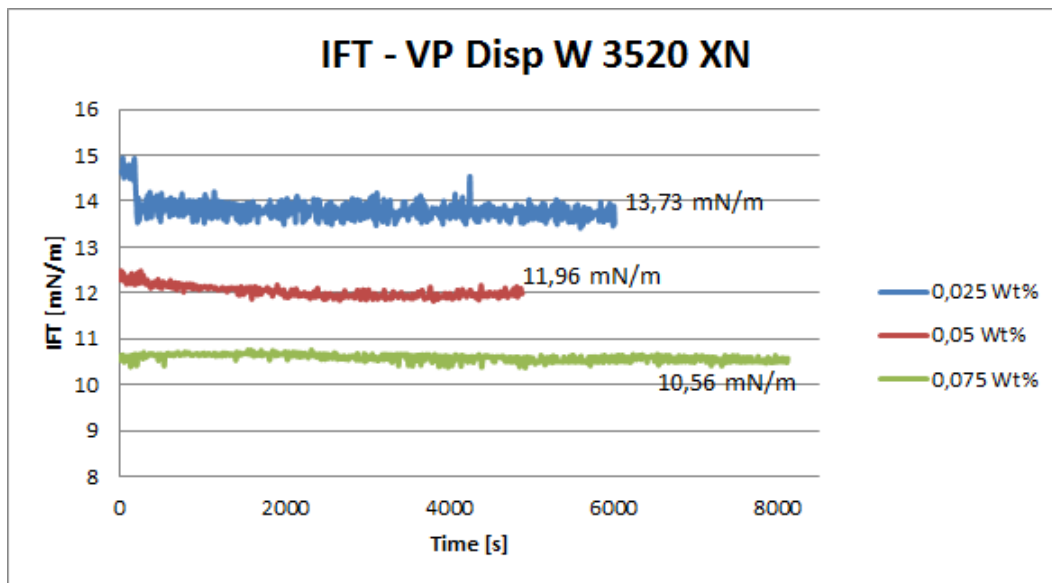


FIGURE 5.7: IFT between oil and VP Disp W 3520 XN (medium sized particles).

5.5 Stability of Nanofluids

Nanoparticles in DI water together with a stabilizing agent will remain dispersed for months. However, adding salt will give a more unstable dispersion. Each particle will have a structure of ions at the surface called the electrical double layer. Equal particles will have equal charged ions on their surface, meaning the electrical double layer will have a repulsive force on the other particles. When the salt concentration is increased, or monovalent ions are swapped for divalent ions, the radius of the electrical double layer will shrink. When this happens, the particles can get closer to each other before the repulsive force kicks in. Thus it will be easier for the particles to collide and form agglomerates. (Hiemenz and Rajagopalan, 1997; Yu et al., 2010) If the procedure described in Chapter 4.2.3 for preparing a nanofluid of 0,05 wt% was followed, it would remain stable for at least two days. After a certain point (depending on the type of nanofluid), the particles would start making agglomerates, as seen in Figure 5.8. The length at which a nanofluid remains stable is of great importance when it comes to EOR applications. Large agglomerates can plug the reservoir rock, making it impermeable. Hence, any nanofluids showing rapid destability will be ineffective and unsuitable for EOR purposes.

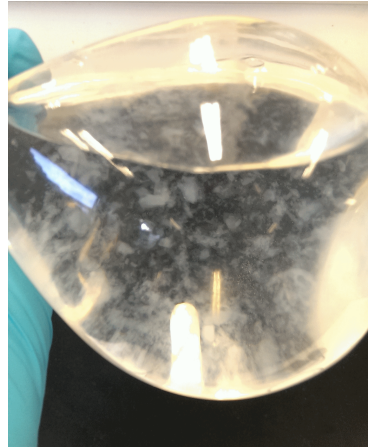
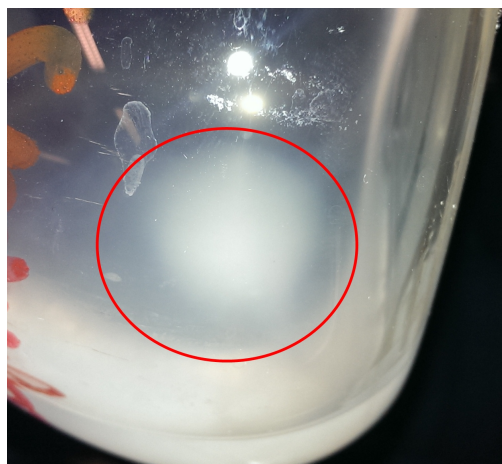


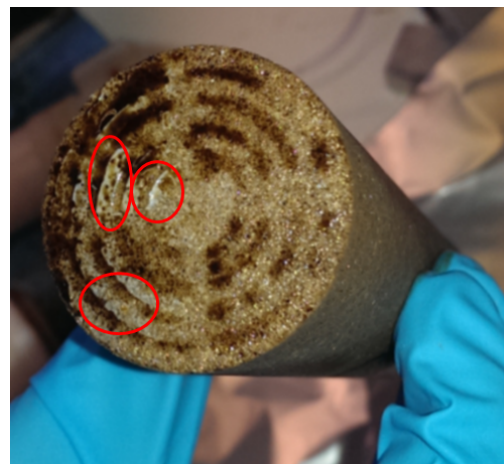
FIGURE 5.8: Fumed silica nanofluid after a week.

5.5.1 IDISIL EM-7520K

Nanofluid made out of the colloidal silicon dioxide IDISIL EM-7520K showed instability and agglomerations of nanoparticles at a very early stage. Even though the nanofluid provided an increased recovery of 3,5 %, the destabilization proves that it's not suitable as an EOR agent. Figure 5.9a shows the nanofluid 4,5 hours after mixing. The nanoparticles had gathered at the bottom of the flask. After the flooding experiment were completed and the core sample was taken out of the core holder, layers of nanoparticles were observed at the inlet (Figure 5.9b). This might have prevented portions of the particles from traveling through the core.



(A) IDISIL-7520K nanofluid 4 hours after mixing.



(B) Visual nanoparticles at the inlet of the core.

FIGURE 5.9: Destability of IDISIL EM-7520K.

5.6 Core flooding

Six types of silica nanoparticles were tested with coreflooding. They differentiate from each other by size and shape. According to [Li et al. \(2013a\)](#) and [Hendraningrat et al. \(2013d\)](#) a 0,05 wt% concentration of silica is optimal in terms of oil recovery. It was therefore decided to test all the different nanoparticles at this concentration, both in a case using medium permeability cores and a case using high permeability cores. Based on these experiments, the three nanofluids with the most promising results were proceeded to testing with different concentrations. A constant pump rate of 0,4 mL/min for both brine and nanofluid were used. First brine was injected to displace oil until residual oil saturation was reached. Afterwards, nanofluids were used as a tertiary recovery method to see if any additional oil could be mobilized. Each phase was continued until no more oil was produced, usually after 2-3 PV injected.

5.6.1 Medium Permeability Cores

All the nanoparticles showed promising results, giving increased oil recovery from the medium permeability cores. The best result came from the large fumed silica nanoparticle AERODISP W 7620 N, which gave an additional recovery of 11,76 %. The nanoparticle with the least effect was the small colloidal silica IDISIL IC 0820, with an additional recovery of 2,36 %.

The fumed particles provided overall a better additional recovery than the colloidal silica. Additionally, larger particles proved to be more effective in mobilizing oil than the smaller particles. All the cores had very similar properties, in hope that the small differences would not distinguish the results in any way.

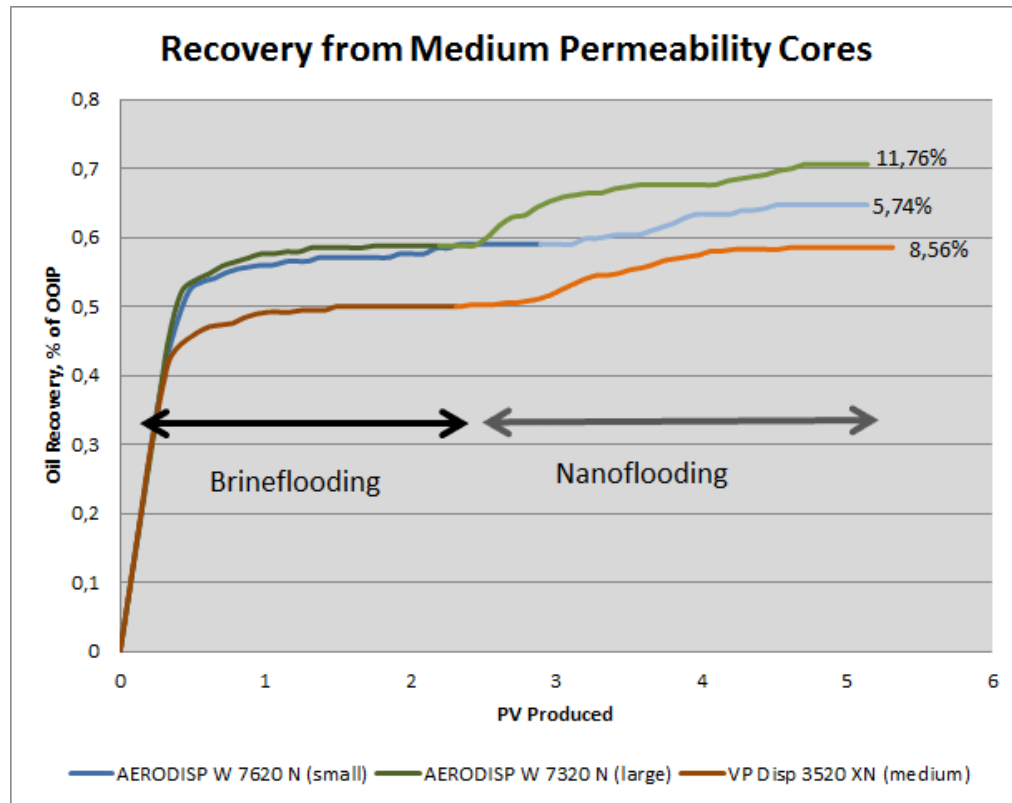


FIGURE 5.10: Increased Recovery using 0,05 wt% fumed nanoparticles.

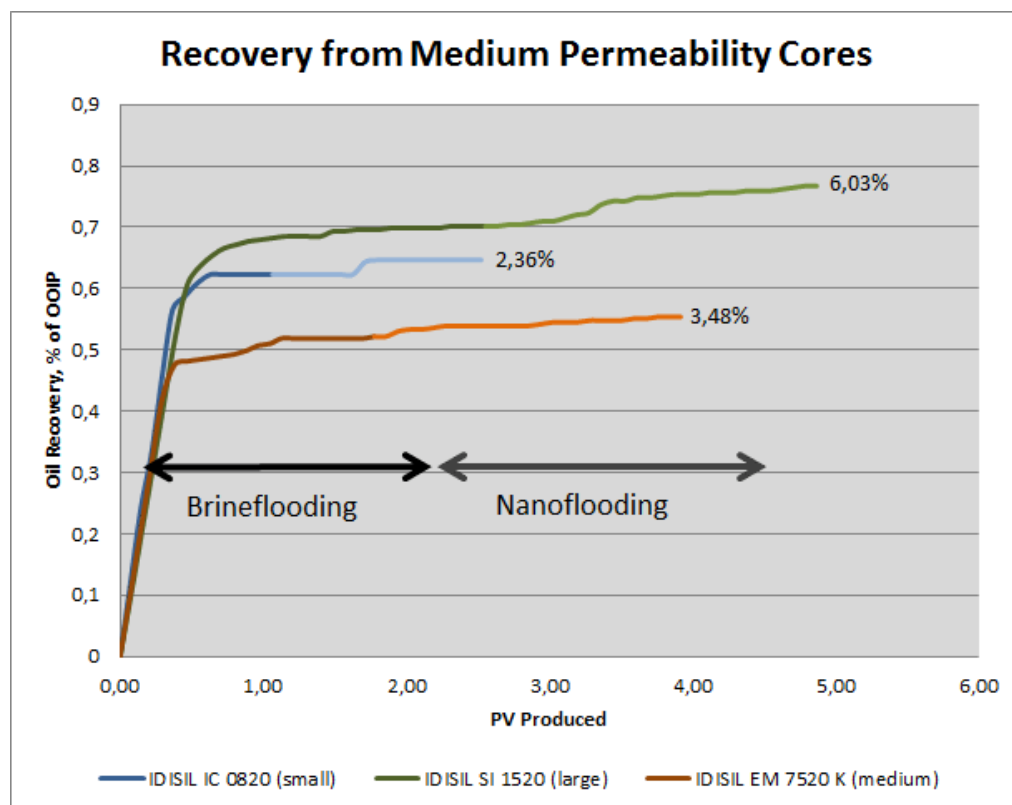


FIGURE 5.11: Increased Recovery using 0,05 wt% colloidal nanoparticles.

5.6.2 High Permeability Cores

Compared to the medium permeability cores, the recovery from high permeability cores were poor. None of the nanoparticles could provide additional recovery above one percent, and some gave none at all. There were no distinguishable differences between fumed and colloidal silica, nor between larger and smaller particles. Because it was difficult to compare the nanofluids' impact on oil recovery in high permeability cores, the medium permeability cores were used for the flooding tests with different nanoparticle concentrations.

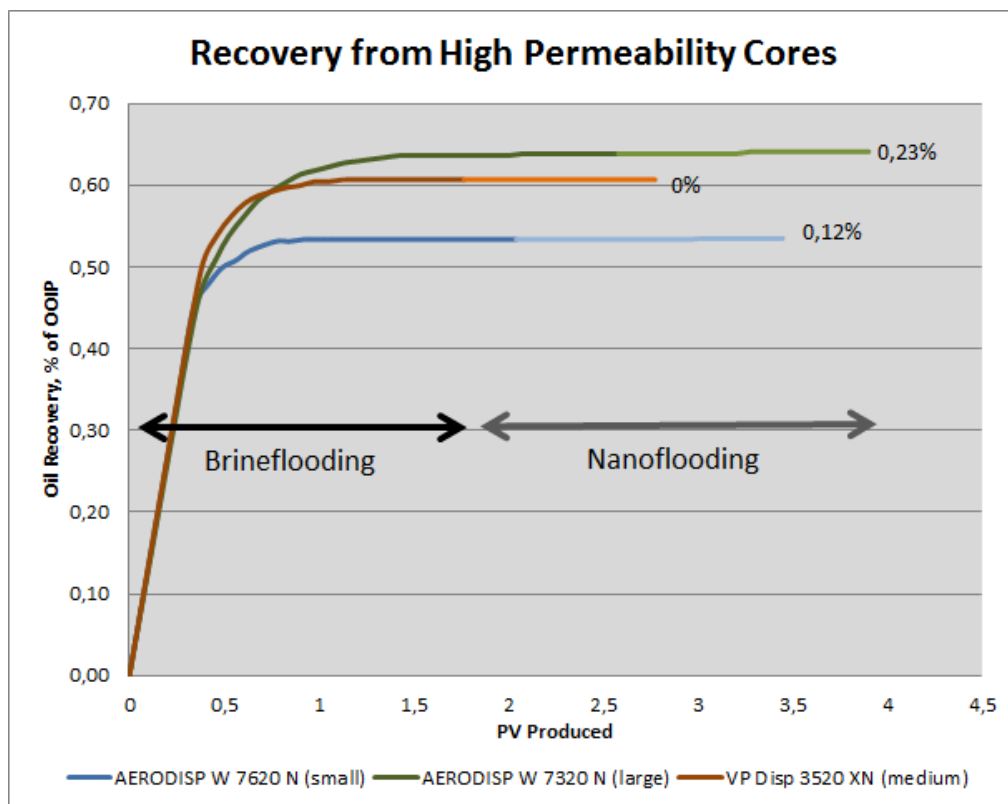


FIGURE 5.12: Increased Recovery using 0,05 wt% fumed nanoparticles.

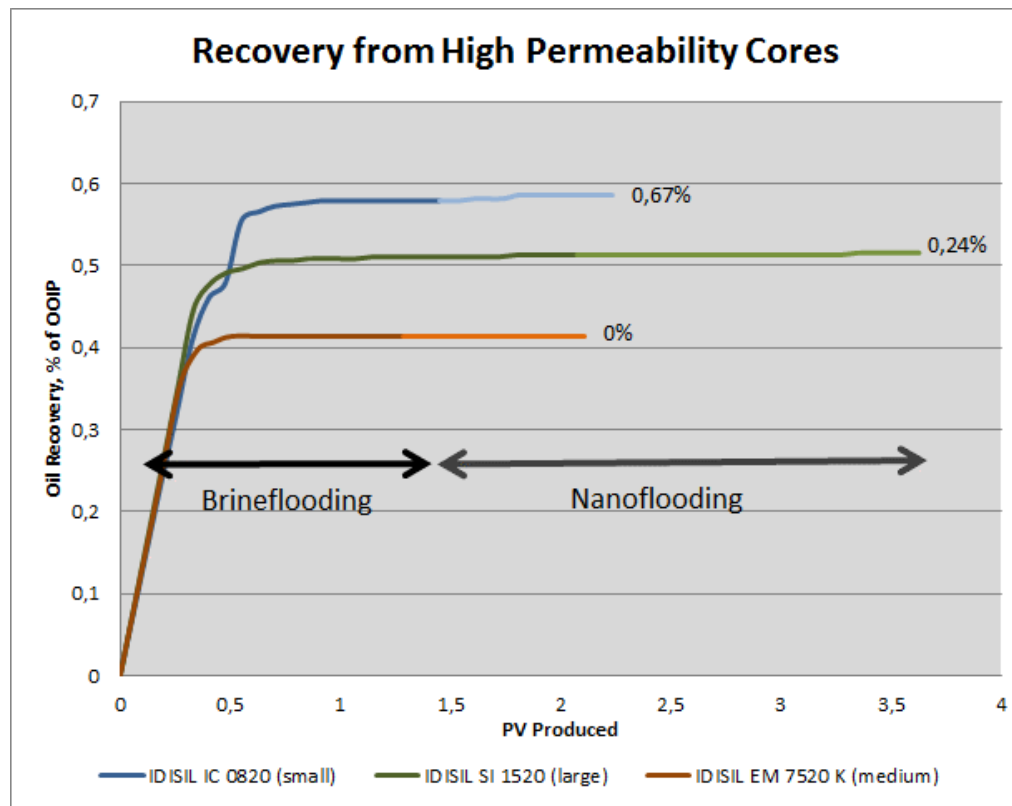


FIGURE 5.13: Increased Recovery using 0,05 wt% colloidal nanoparticles.

5.6.3 Differential Pressure

The differential pressure was measured across the core during the flooding experiments. XRD analysis showed that the only clay mineral found in the cores was kaolinite, which is non-swelling. Hence no pressure increase is due to swelling of minerals. The graphs below show the pressure development for the brineflooding (black) and the nanoflooding (red) at 0,05 wt% concentration. The general trend was that the pressure would stabilize during the brineflooding, and then steadily rise during the nanoflooding. The increase seemed to continue indefinitely. The differential pressure were rising more rapidly in the medium permeability cores compared to the high permeability ones.

As seen from the graphs, the pressure drops across the medium permeability cores are much larger than across the high permeability cores. Since the fluids used in the experiments are the same (apart from minor variations in the nanofluids), the pressure drop is related to the rocks properties. In particular the permeability,

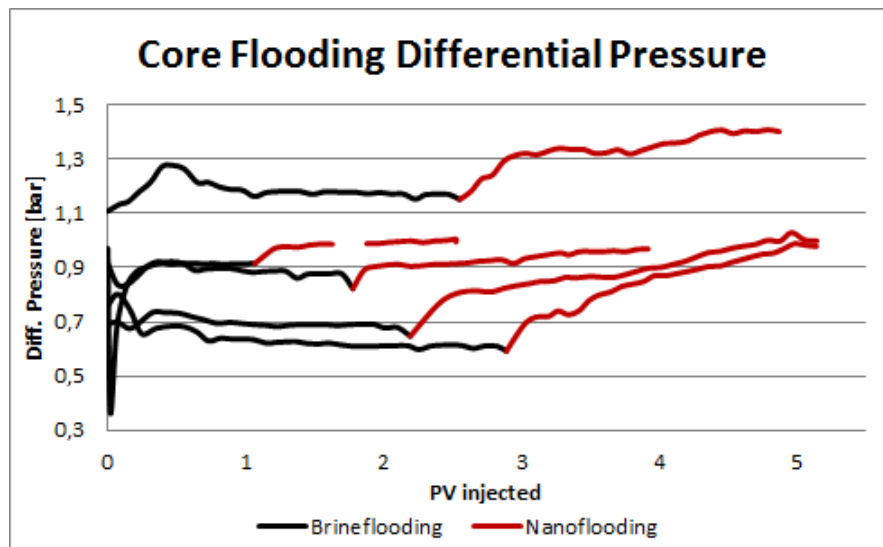


FIGURE 5.14: Differential pressure across medium permeability cores.

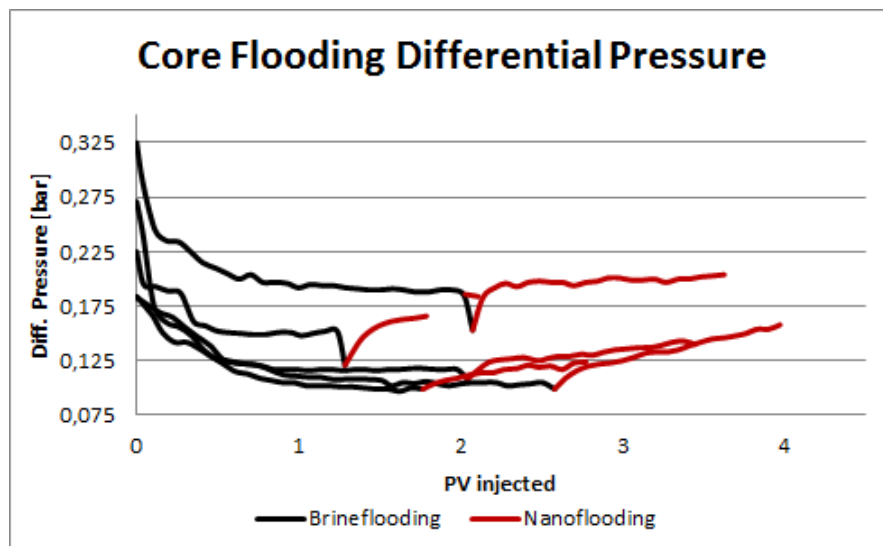


FIGURE 5.15: Differential pressure across high permeability cores.

as seen from Equation 2.8. The pressure increase seen during the nanoflooding is believed to be a result of retained nanoparticles in the pores, inducing a permeability impairment.

5.6.4 Concentration Tests

Based on the flooding experiments with a 0,05 wt% nanoparticle concentration, it was decided to focus on the fumed silica particles for concentration tests. A 0,025 wt% and 0,075 wt% nanofluid were prepared for each of these three types. The results were compared to the 0,05 wt% flooding experiments in Figure 5.16 to 5.18.

As reported earlier by Li et al. (2013a), the optimal nanoparticle concentration in terms of oil recovery is the 0,05 wt%. This corresponds with the results presented in this thesis. The flooding experiments at different concentrations provided significantly less additional recovery. None of them came close to the results of the 0,05 wt% nanofluid, for any of the fumed silica types.

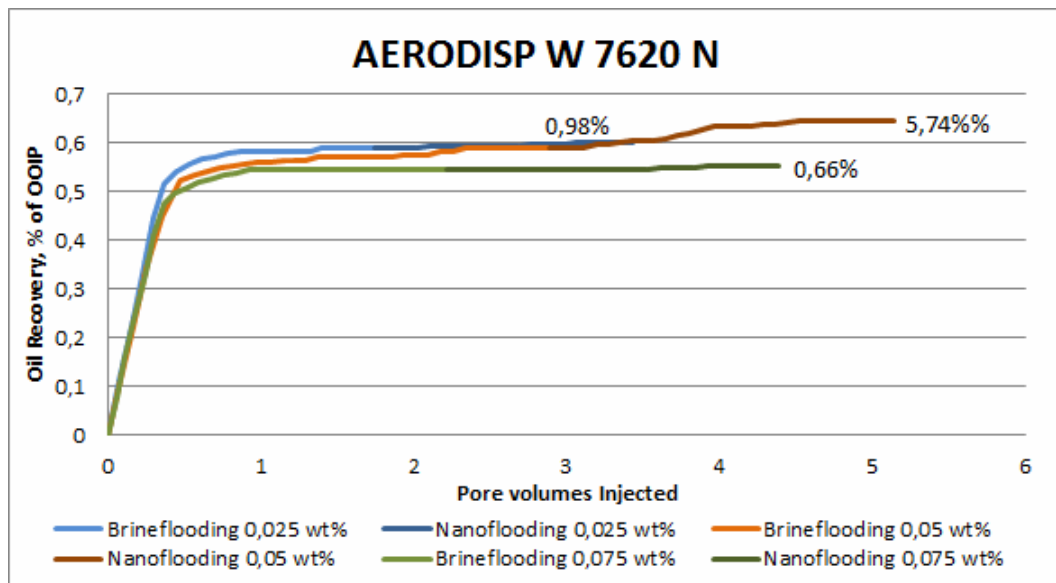


FIGURE 5.16: Increased recovery from AERODISP W 7620 N (small particles) at different concentrations.

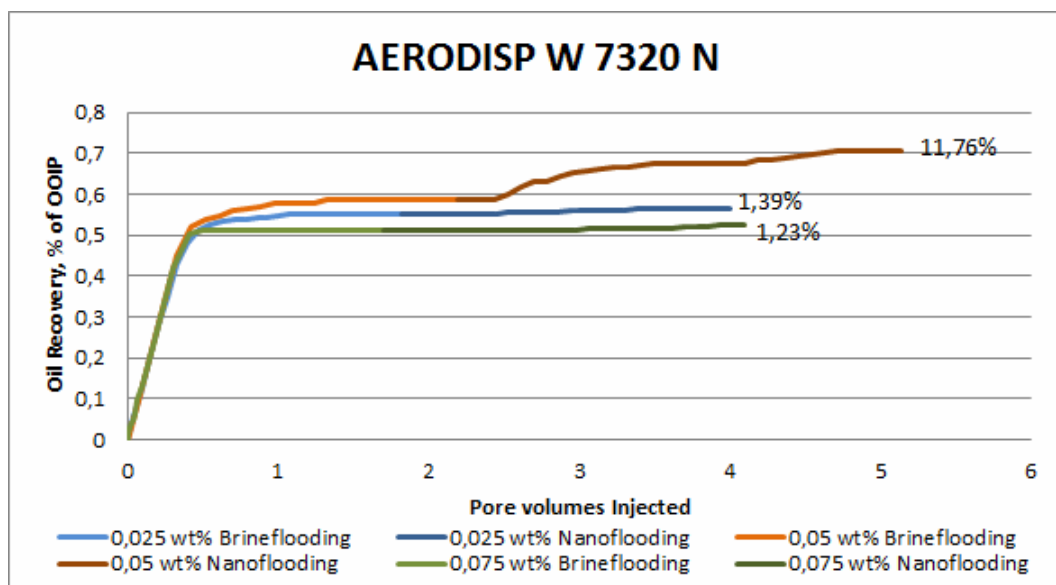


FIGURE 5.17: Increased recovery from AERODISP W 7320 N (large particles) at different concentrations.

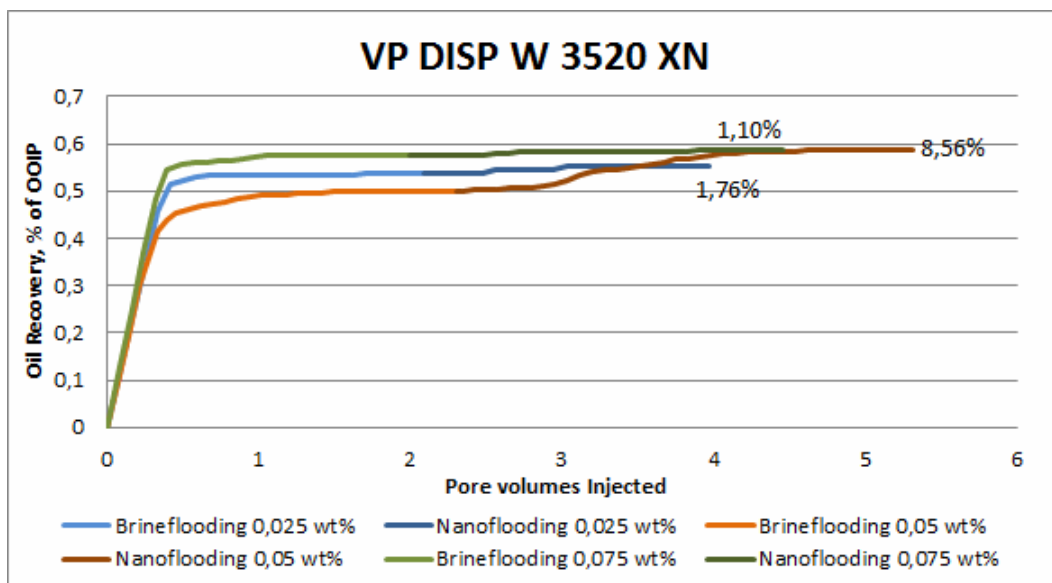


FIGURE 5.18: Increased recovery from VP Disp 3520 XN (medium sized silica) at different concentrations.

5.6.5 Coreflooding Summary

A summary of the flooding tests with different nanoparticles is given in Table 5.6. Given that the nanofluids were most efficient at 0,05 wt% concentration, the table focuses on these flooding experiments. Initial water saturations and residual oil saturations for all the cores were very similar, and there were no correlations between increased recovery and these saturations. Thus, they will not be listed here. All relevant flooding data can be found in Appendix C.

TABLE 5.6: Summary of the increased recovery from 0,05 wt% nanofluids in medium and high permeability cores.

Nanofluid	Size ³	Recovery Medium Perm. %	Recovery High Perm. %
AERODISP W 7620 N	S	5,74	0,12
VP Disp 3520 XN	M	8,56	0
AERODISP W 7320 N	L	11,76	0,23
IDISIL IC 0820	S	2,36	0,67
IDISIL EM 7520 K	M	3,48	0
IDISIL SI 1520	L	6,03	0,24

³S=Small, M=Medium, L=Large.

5.6.6 Validation tests

To confirm the measured values from earlier flooding experiments, second tests were performed to validate the results. Due to time constraints and the time required to perform one flooding test (6-9 hours), the fumed silicas were the only nanofluids tested. The three fluids were tested in medium permeability cores first (see Figure 5.19). They showed significantly lower results than previous experiments, although the general trend was the same with increasing recovery for increasing particle size.

It was suggested that something with the experimental setup could have changed from the first to second tests, given the low additional recovery compared to previous flooding experiments. The setup itself was unchanged, but there could have been some damage to the sleeve in the coreholder. If so, major portions of the nanofluid would flow around the core instead of through it, due to uneven confining pressure. The reason behind this assumption was that prior to the validation tests, a sound of leaking air from the coreholder appeared when applying sleeve pressure above 16 bar. The flooding experiments were still conducted, but with a little lower sleeve pressure compared to the previous tests. The old sleeve was replaced with a new one before the final core flooding test (Figure 5.20). The workshop had disposed of the old sleeve when they replaced it, thus it was not inspected for any visible sign of damage.

Only one test was performed on high permeability because there were no cores left with the properties wanted. Ideally all the nanofluids should be tested at least twice to confirm the results. However, due to time constraints and insufficient experimental material (cores) only a few were tested a second time.

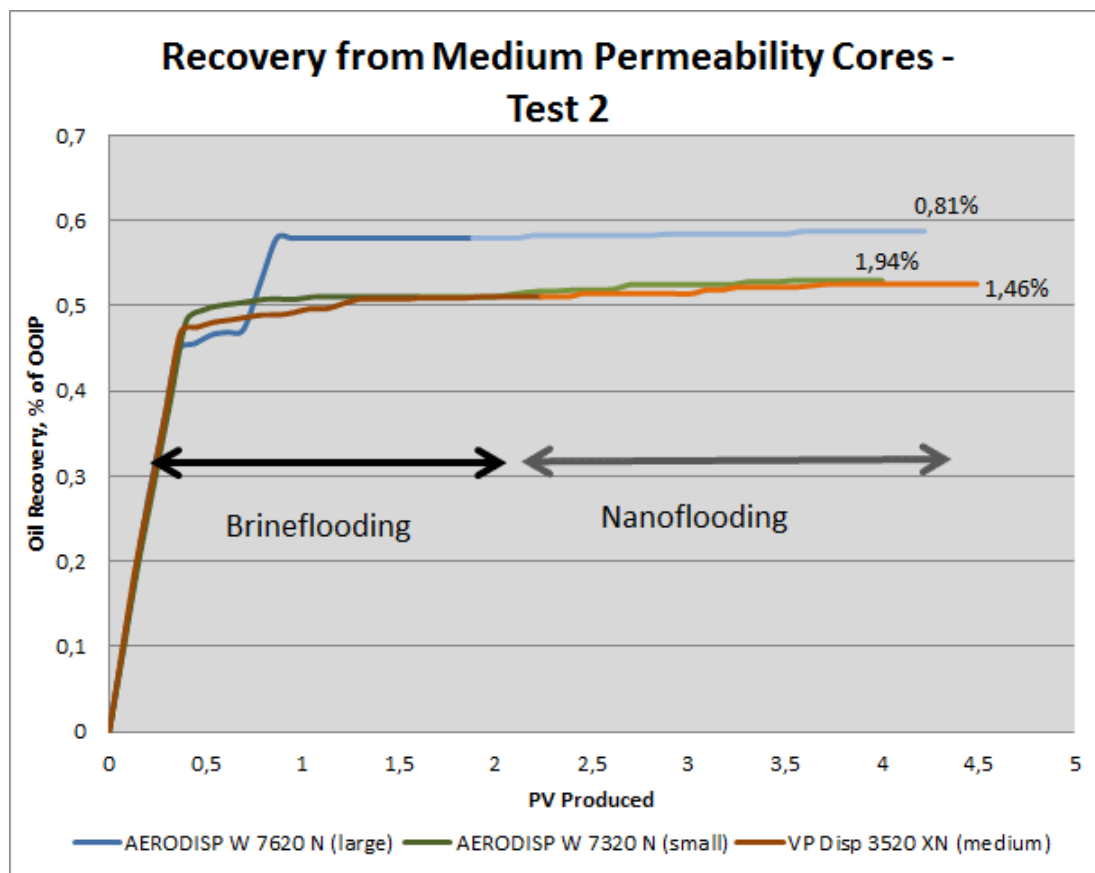


FIGURE 5.19: Test 2 using 0,05 wt% fumed silica in medium permeability cores. Tests performed with the old sleeve.

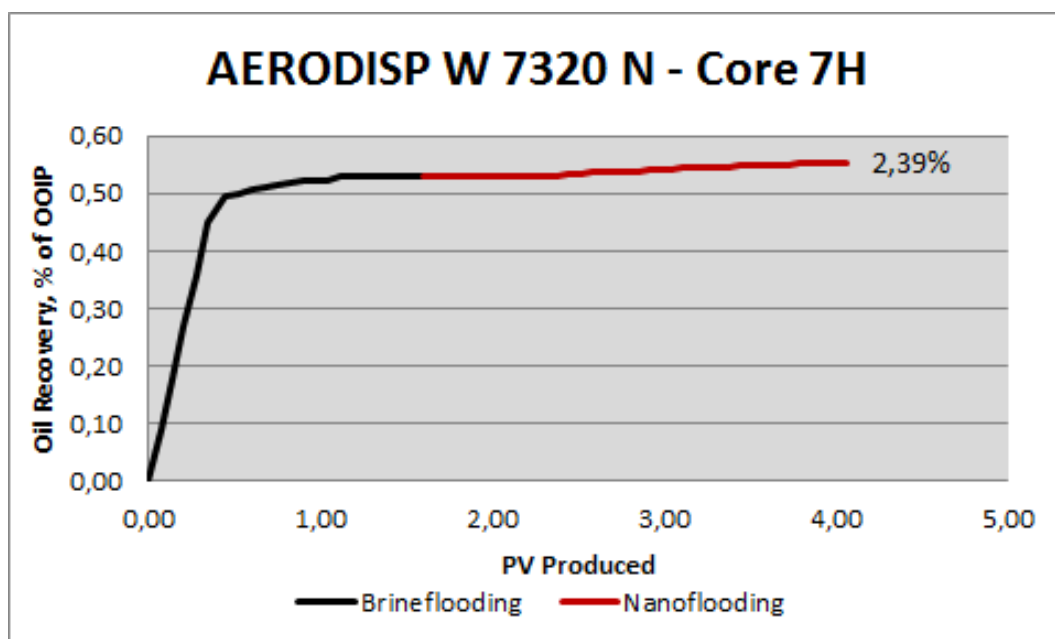


FIGURE 5.20: Increased recovery using 0,05 wt% AERODISP W 7320 N in a high permeability core. Test performed with a new sleeve.

Chapter 6

Discussion

6.1 Wettability Alteration

The contact angle of an oil droplet on a smooth glass plate immersed in brine was observed to increase as nanoparticles were added. This means that the wettability of the glass plate is changed, becoming more water wet. The wettability alteration is related to the spreading of nanoparticles on the glass plate. As proposed by [Wasan and Nikolov \(2003\)](#), the creation of a wedge film of nanoparticles at the three-phase contact enhances the spreading behavior of the particles, disrupting the interface between the solid surface and the oil droplet (see [Figure 6.1](#)). This will alter the wettability, as displayed by the increased contact angle. The spreading behavior depends on particle volume fraction, particle size, polydispersity and particle charge. ([Zhang et al., 2014](#)) Simulations have shown that spreading of nanoparticles will increase with increasing concentration and decreasing particle size. ([Chengara et al., 2004](#)) The electrostatic repulsion between particles will increase with concentration, giving a larger structural disjoining pressure which drives the wedge film forward. ([Wasan and Nikolov, 2003](#)) Altering the wetting preference of the rock can mobilize trapped oil in the porous system by overcoming capillary forces.

Improper cleaning of equipment, too short equilibrium time, moving oil droplets and inaccurate adjustment of the image baseline which had to be placed manually are possible sources of inaccuracy during the experiment. In addition, the tests were conducted on a glass plate, and not on the surface of Berea sandstone or a

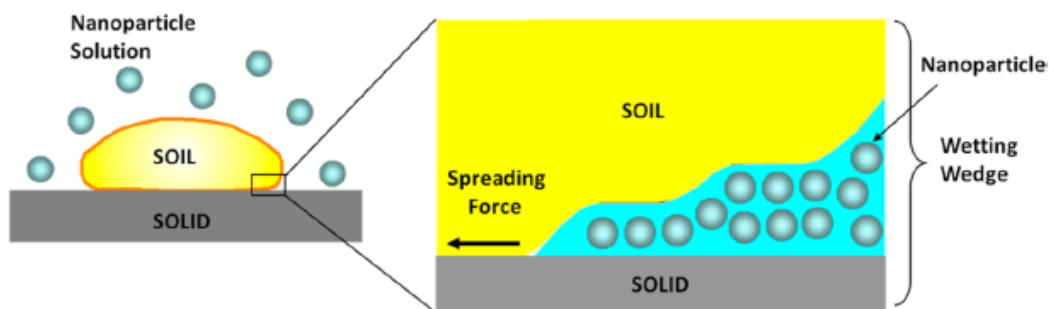


FIGURE 6.1: Spreading of nanoparticles on a solid surface. (Zhang et al., 2014)

quartz plate. Thus there will be some deviations. Nevertheless, considering that the glass plate is made out of quartz, the dominant mineral of sandstone, it is an adequate assumption that the two surfaces are analogous.

6.2 Interfacial Tension

The introduction of nanoparticles to an oil/brine system gave a lower interfacial tension, and the reduction might be large enough to mobilize more oil by overcoming capillary forces. Depending on the type of nanofluid used, the reduction varied between 11 % and 29 %. It was observed that the small, fumed particles gave the best results, while the largest particles gave the least IFT reduction both for the fumed and colloidal cases. The reduction in interfacial tension is due to nanoparticles assembling on the interface between the oil and the aqueous phase. This layer of particles will lower the tension between the two immiscible fluids. As the silica is strongly hydrophilic it will remain mostly in the brine phase. Due to Brownian motion particles will be effectively distributed to an equilibrium configuration with the lowest total free energy. Consequently, some of the particles will gather at the fluid interface due to the fact that reducing the oil-brine contact area is energetically favorable. (Binks, 2002) It has to be noted that the nanofluids used contain a stabilizing agent, Sodium Hydroxide (NaOH). The NaOH might have an impact on the measurements as it has been observed to decrease the IFT between oil and aqueous solutions. (Xu, 1995) The reduction in IFT seen in this experiment can therefore be a result of both the nanoparticles and the stabilizer in combination. An experiment using brine with NaOH and oil should have been conducted in order to investigate the effect of introducing nanoparticles.

Adsorption of hydrophilic particles on oil/water interfaces has been observed to increase with decreasing particle size. (Sharpa et al., 2013) Thus it was expected that the particles with the highest specific surface area (= smallest particles) would give the lowest IFT, as they have the potential to cover a larger portion of the oil/brine interface. This was indeed the case for the fumed particles. However, medium colloidal silica had a slightly larger reduction than the smaller colloidal particle. The difference is very small and due to difficulties in getting a stable IFT reading from the medium sized colloidal silica (because of the instability of that nanofluid), the measurement might be slightly inaccurate.

The temperature will have an effect on the measurements. High temperatures can reduce the IFT in a oil/aqueous system. Since the measurements in this thesis were performed at room temperature, it is believed that the IFT would have been lower had the experiments been carried out under reservoir temperature. (Lara et al., 2012) The complexity of the salts in the brine will also have an impact on the IFT reduction. The North Sea Brine used in the experiment contains several divalent ions (Ca^{2+} , Mg^{2+} and Sr^{2+}). Higher valency ions and salt concentration have a tendency to lower the effect of nanoparticles on IFT. (Miranda et al., 2012; Lara et al., 2012) This is caused by a difference in the distribution of ions in the solution, which modifies hydration and electrostatic potential for ions near the nanoparticle. Swapping adsorbed monovalent ions (e.g. Na^+) on the silica surface for divalent ions will reduce the hydration and hence effect the radius of the nanoparticles. (Fielden et al., 2000)

In addition to lowering the interfacial tension, the gathering of solid nanoparticles at the oil/brine interface has been observed to induce highly stable pickering emulsions. (Zhang et al., 2010) Emulsions of this sort can withstand harsh conditions due to irreversible adsorption of nanoparticles on the surface of the oil droplet, and they can remain stable for several months without coalescence. The average drop diameter of oil-in-water emulsions will decrease with decreasing particle size and increasing concentration (Binks and Lumsdon, 2001; Binks and Whitby, 2004; Zhang et al., 2010), meaning it can travel longer distances in the reservoir without much retention.

The IFT was measured at different concentrations for the three fumed silica types;

0,025 wt% and 0,075 wt% in addition to the 0,05 wt% already acquired. The general trend was a greater reduction in IFT the higher the nanoparticle concentration in the aqueous phase. This is in agreement with the theory given in Chapter 3.2.2. Nanofluids of higher concentrations should leave more particles to gather at the oil/brine interface and hence lower the IFT. However the nanofluids made from small and large fumed silica particles showed the largest IFT reduction for 0,05 wt%, followed by the 0,075 wt% concentration. There is no good explanation for this, but it's possibly due to errors during the experiment. Due to the short deadline of the thesis and that the spinning drop tensiometer was frequently occupied, second experiments were not conducted.

The main challenges with the spinning drop method were the cleaning process and air bubbles in the sample. Strong solvents such as toluene, acetone and methanol were used in the cleaning process. Any residue will affect the IFT. The hardest part of the experiment was trying to place the oil droplet in the test tube and close it without any air bubbles inside. The bubbles tend to merge with the oil droplet and ruin the experiment. Lastly, in a few experiments the oil droplet was so small that the spinning drop tensiometer had difficulties measuring. The IFT is measured by comparing the horizontal radius of the oil droplet to the vertical radius. If the droplet is really small, the difference between these two radiuses are insufficient for a stable reading.

6.3 Retention of Nanoparticles

It was obvious based on the increasing differential pressure during the nanoflooding that a small portion of particles is retained in the cores. The only clay present in the cores was kaolinite, which is non-swelling and will have no impact on the pressure development. Nanoparticle retention occurs by one of four different physical mechanisms, explained in Chapter 3.2.5. Mechanical entrapment occurs when a particle has a greater size than the pore throat and therefore blocks it. Gravity settling can happen when the injected particles have a higher density than the carrying fluid and will settle on the pore wall due to gravity. Since the nanoparticles have low specific gravity and small particle size (7-16 nm) these two mechanisms will seldom occur in these experiments. As nanoparticles can gather in agglomerations with larger radius than the particle itself, the larger clusters can

still be trapped at the pore throat in some cases. However, it is believed that this happens seldom, meaning mechanical entrapment will have limited effect. That leaves adsorption and log-jamming as the main mechanisms for retention.

The differential pressure measured during the flooding seemed to increase indefinitely during the nanoflooding. During both the oil and brine injection the pressure would reach a maximum, and either decrease or stabilize after that point. The increase in pressure during the nanoflooding is caused by retention of nanoparticles in the core, inducing a permeability impairment. This effect was observed to have less impact in the flooding experiments with high permeability cores. The high permeability cores had a very slow pressure increase during the nanoflooding. The reason for this might be that the pore throat size increases with increasing permeability. (Pittman, 1992) This will make it less likely for log-jamming and mechanical entrapment to occur.

Samples were taken of the effluent fluids during the nanoflooding and sent to Evonik Industries in Germany for analysis. The purpose of this was to measure the concentration of nanoparticles in the effluent fluid, as it would determine the loss of particles in the core. Especially interesting would be to take samples at different time intervals, to see if the retention changes as more and more nanofluids are injected. The adsorption/desorption process of particles on the pore wall should eventually reach equilibrium with continuous injection. (Zhang et al., 2013) It is therefore expected that the nanoparticle concentration of the effluent fluid will increase over time as the adsorption capacity of the rock is reached. Eventually it should reach the concentration of the injection fluid. After this point, any retention will occur due to blocking of pore throats, most likely log-jamming. Unfortunately the effluent concentration results were not available before the deadline of this thesis.

Concentration analysis can be used to establish the maximum adsorption capacity of a rock surface at a given operating condition. This property is dependent upon the particle size, injection concentration, pore size and flow rate. (Bolandtaba et al., 2009; Skauge et al., 2010; Zhang et al., 2013). A better understanding of the retention process is important for predicting the porosity and permeability impairment. By injecting brine after the nanofluid, it is also possible to find how

much of the adsorption is reversible and irreversible. Knowledge around this can help us design a better recovery scenario. For example, a possibility could be alternating nanofluid and brine as an alternative to continuous nanoflooding. This way, the nanofluid can potentially mobilize more oil, while the brine can desorb the reversible particles and perhaps prevent major porosity/permeability impairments.

6.4 Coreflooding Experiments

Six types of nanoparticles were tested with respect to their ability to enhance oil recovery, all with a particle concentration of 0,05 wt%. The differences between each of these types are the particle size and morphology. They all increased the oil recovery in medium permeable cores, where fumed silica showed the most promising potential, increasing the recovery with 5,74 % to 11,76 %. The colloidal silica provided an additional recovery of 2,36 % to 6,03 %.

Increased recovery from the medium permeable cores was significantly higher than from the high permeable cores. [Hendraningrat et al. \(2013e\)](#) tested recovery from low and medium permeable cores using different concentrations of silica. Their experiments showed increasing displacement efficiency with increasing permeability. The permeability range of the cores went up to 392 mD, which is equivalent to the medium permeability cores used in this thesis. The fact that recovery from the high permeability cores in this thesis had low recovery indicates that silica nanoparticles will increase the recovery with increasing permeability up to a certain point, before they start losing effect. In high permeability rocks the particles seems to be effectively flushed through without affecting the oil recovery much.

Several possible mechanisms for increased oil recovery using nanoparticles have been mentioned in Chapter 3.2. Traditional mechanisms such as wettability alteration, IFT reduction, favorable viscosities as well as the concept of structural disjoining pressure have the potential to mobilize trapped oil. All of these mechanisms are a function of the nanoparticles' chemical properties. The size of the particles is especially important; smaller particles will have a higher surface area. This makes them more suitable for covering the oil/brine interface and lowering the tension. A higher specific surface area also means that the particles can cover a larger

part of the rock surface and hence alter the wettability. This is supported by the contact angle measurements, where large particles had a lower angle than the small particles. An increased contact angle means that the system gets more water wet and the oil trapped at the rock surface is easier to mobilize.

[Chengara et al. \(2004\)](#) showed that the structural disjoining pressure increased when the diameter of each particle decreased. The number of particles increases as the diameter gets smaller (for the same volume fraction). Consequently more particles are pumped into the wedge film at the three phase contact region by entropic forces and the structural disjoining pressure increases. Polydispersity, or the heterogeneity of sizes of molecules, will also highly affect the structural disjoining pressure. [Chu et al. \(1996\)](#) indicated that a 20 % variation in particle size can result in a 30 % decrease in the structural disjoining pressure. Unequal sizes of particles prevent them from ordering in the wedge film.

In summary, all these recovery mechanisms indicate that smaller particles are most suited for mobilizing oil. This is also shown in coreflood experiments performed by [Hendraningrat et al. \(2013f\)](#) where recovery increased with decreasing particle diameter. However, experiments performed in this thesis show the opposite trend (see Figures [5.10](#) and [5.11](#)). The highest increased recovery was achieved using the largest fumed silicas particles. This indicates that the recovery mechanism has a mechanical nature rather than chemical. One possible explanation is that the dominant mechanism for mobilizing oil is log-jamming. Due to the smaller size of pore throats and constant differential pressure, fluid flow velocity is increased at the pore throat compared to pore bodies. At the entrance of the pore throat, water molecules will accelerate faster than the heavier silica particles. This results in an accumulation of particles that can eventually block the pore entrance and divert waterflow from waterfilled pores into other pores, possibly oil filled. ([Bolandtaba et al., 2009](#); [Skauge et al., 2010](#)) As retention increases with increasing particle diameter ([Todd et al., 1984](#); [Gao, 2008](#)), the large silica will be more likely to cause retention by log-jamming. This might explain why the recovery increased with increasing particle size.

Two types of silica were experimentally tested. The fumed silica differs from the colloidal by their structure/shape. While the colloidal particles have a spherical

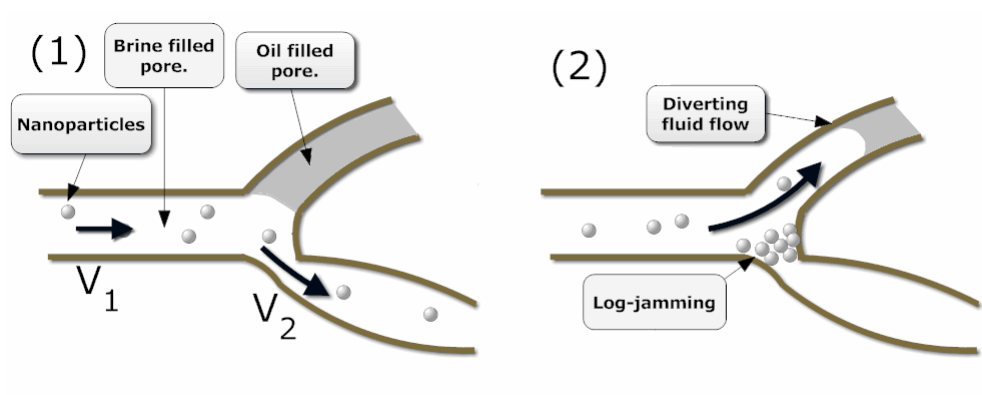


FIGURE 6.2: (1) Nanoparticles accumulate at the pore throat due to different flow velocities in the pore body and at the pore throat ($V_1 \neq V_2$). (2) The pore throat will eventually be blocked, diverting fluid flow into other pores, which could be oil filled.

form, the fumed particles are made out of chain-like structures fused together. The three sets of sizes for the colloidal particles is approximately the same as for the fumed particles, while the specific surface area was slightly higher for the colloidal particles (for particles of the same size). It was therefore interesting to see that the fumed silica was so much more effective in mobilizing oil. If log-jamming is the dominant EOR mechanism, the shape of the particles might be an important factor for whether or not a pore throat will be blocked.

Based on the coreflooding experiments performed in this thesis, nanoparticles appear to have a higher potential to mobilize oil in medium permeability cores compared with high permeability cores. See Figure 5.10 to 5.13 for results. Since the size of pore throats often increases with permeability (Pittman, 1992), log-jamming will be less likely to occur in the high permeability cores. Looking at the pressure drops during nanoflooding (see Chapter 5.6.3) the medium permeability cores experience a much larger pressure increase than the high permeability cores. A more rapid increase indicates that the core is subjected to a more extensive permeability impairment, which is caused by nanoparticle retention. This further suggests that log-jamming is the cause of the mobilized oil. In the high permeability cores, the nanoparticles seem to be effectively flushed through without having much effect, thus giving lower recovery. Running an analysis of the effluent nanofluid would tell us if the majority of nanoparticles stays in the brine or undergoes retention.

The oil recovery might be dependent upon the fluid flow rate. [Hendraningrat et al. \(2013f\)](#) investigated how oil recovery varied with injection rate using 7 nm silica nanoparticles. They tested rates between 0,2 mL/min and 0,8 mL/min. The results showed that oil recovery decreased with increasing injection rate, making 0,2 mL/min the optimal rate in terms of maximum oil recovery. However, their tests had one weakness. Only small silica particles of 7 nm were tested. It is fair to assume that larger silica particles will have a greater mass. For a constant flow rate, heavier (larger) particles will migrate slower through the pore system compared to the lighter (smaller) particles. Thus, they will have more time to chemically react with the rock surface and/or the oil-brine interface. This indicates that oil recovery during nanoflooding is dependent upon the injection rate. Small particles might need a lower flow rate to fully exploit their potential, while larger particles can work well at higher velocities. In addition, the flow rate used in this thesis is high compared to normal rates in the reservoir. This will give high viscous forces that could recover more oil during the brineflooding and leave less oil for the nanoparticles to work on. Thus, the additional recovery from nanoflooding might have been higher using lower injection rates.

Increasing the viscosity of the brine using nanoparticles would lower the mobility factor and give a more "piston like" displacement. But since the viscosities of the nanofluids were practically the same as brine, it's assumed that this will have no effect on the displacement efficiency.

Hydrophilic nanoparticles such as the silica used in this thesis have the ability to make cores more water wet. ([Li et al., 2013b](#)) Such a wettability alteration has the potential to release trapped oil in the pore system. However, Berea sandstone cores which have not been subjected to aging are usually strongly water wet. ([Vevle, 2011](#)) It is therefore not likely that the silica will have any major impact on the wetting preference of the cores used in these experiments (which have not been aged). In real term oil fields the sandstone reservoir is typically neutral to weakly water wet meaning wettability alteration might have an impact on the recovery. Coreflooding experiments in the future should therefore include aging of cores for more realistic results.

6.4.1 Recovery at Different Nanoparticle Concentrations

As expected, based on previous studies ([Hendraningrat et al., 2013b,c,e](#)), the recovery during the nanoflooding was highest when using a 0,05 wt% nanoparticle concentration. Both the lower concentration of 0,025 wt% and the higher concentration of 0,075 wt% provided significantly lower recovery. The difference in additional recovery can be explained by a system where larger amounts of nanoparticles enhance the EOR mechanisms while at the same time increase the porosity/permeability impairment. The nanofluid at 0,05 wt% seems to be optimal for the interactions happening, where retention is low while at the same time there is enough nanoparticles to efficiently mobilize more oil.

The high concentration nanofluid provides larger amounts of nanoparticles which can structure inside the wedge film and provide a higher structural disjoining pressure in addition to better IFT reduction and wettability alteration. The reason why these nanofluids give such a low additional recovery could be a major porosity/permeability impairment, caused by retention of nanoparticles. The impairment can trap the oil within the pores, preventing it from being recovered. ([Hendraningrat et al., 2013a](#)) It has to be noted that retention by log-jamming can increase recovery to a certain point. However, at high nanoparticle concentration, the retention of particles will be severe. This will begin to plug the reservoir so that the injection fluid won't reach many areas. Thus the additional recovery will be lower for high concentration nanofluids. The low concentration nanofluid also provided little additional recovery. This is most likely due to insufficient nanoparticles present in the system to fully utilize the structural disjoining pressure, IFT reduction and/or changing of wettability. In addition, low concentration nanofluids have fewer retained particles [Todd et al. \(1984\)](#); [Vetter et al. \(1987\)](#) and the recovery effect from log-jamming will decrease. It is possible that log-jamming will not occur at all, or at least will be delayed. The low concentration nanofloodings were continued for around 2 PV, which might be insufficient time-wise for enough silica particles to accumulate and block pore throats.

6.4.2 Limitations and Complications

Laboratory studies are time consuming work which require precision and good procedures. Due to the relatively short deadline of the Master thesis, there was little room for second trials in case of mistakes or errors during the experiments. In combination with the minimal laboratory experience of the author, this has definitely been a limitation.

Because many of the experimental results were obtained through manual readings, it is expected that the error margin of the final results are large, especially for the coreflooding experiments. Firstly, even small deviations in reading volumes from the helium porosimeter can cause significant errors in the final results. The volumes are used to find porosity, which is also an important parameter in calculating saturations and recovery factor. Secondly, effluent fluids during the flooding process were collected in small graduated cylinders. Reading off the exact fluid volume proved difficult, especially with two phases present. During the nanoflooding phase, only small traces of oil were produced. The volume of these traces were often smaller than the scale on the sample tubes which possibly lead to some inaccurate measurements.

Ideally all of the coreflooding experiments should have been done at least twice in order to verify the results. However, since a test lasted a whole day (6-9 hours) there was insufficient time. Thus, only the three fumed silicas were tested a second time. During these verification tests, the sleeve pressure was reduced to 16 bar. A confining sleeve pressure above this gave a sound of air leaking out of the core holder. It is possible that the sleeve around the core was damaged during these last tests, which could make the results unusable. A damaged sleeve would leave a portion of the injected fluid flowing around the core instead of through it. Still the nanofluids showed the same trends as the previous floodings, even though the magnitude of the increased oil recovery is disparate.

It is believed that the work performed is accurate, where results are not affected to a great extent by errors and inaccuracy. However, too few experiments are performed for each case to make any definitive conclusions. The results generally

point in the same direction, but more extensive laboratory work is required to confirm the data.

Chapter 7

Conclusion

This study focused on testing different types of silica nanoparticles with respect to their ability to mobilize oil. Several coreflooding experiments were performed at different permeabilities to investigate the potential of these particles. Interfacial tension and contact angle measurements were performed to support the findings and to help explaining the mechanisms behind the increased recovery. Based on these observations, the following conclusions can be drawn:

- Nanoparticles have the potential to mobilize trapped oil in Berea sandstones. Even though some cases provided significantly more oil, increased recovery is not guaranteed.
- The enhanced oil recovery from using silica nanoparticles seems to diminish with decreasing particle size and increasing permeability for the cases tested in this thesis.
- Fumed silica nanoparticles were generally more effective at mobilizing oil compared to colloidal silica nanoparticles. The optimal concentration in terms of increased oil recovery was 0,05 wt%, for both fumed and colloidal particles.
- Small particles proved to be more effective at lowering the IFT and altering the wettability.
- The experiments performed indicates that a mechanical process, possibly log-jamming, is the main EOR mechanism. Some oil may also be recovered due to IFT reduction and wettability alteration.

7.1 Future Work

Based on the findings of this thesis, following recommendations for future work are made:

- To get a more realistic representation of a typical reservoir rock, the Berea sandstone cores should be aged. This would give a less water wet rock, and hence wettability alterations made by nanofluids could have a greater impact on the recovery process. In addition, the injection rate used is significantly higher than typical flow rates found in a reservoir. Thus, more oil will be recovered during the brineflooding due to higher viscous forces. Ultimately, this leaves less oil for the nanoparticles to work on meaning the additional recovery from the nanoflooding could have been higher.
- Analysis of the effluent nanofluids should be conducted. Samples were taken during the experimental work of this thesis, but unfortunately the results were not available before the deadline. The objective of these analyzes were to investigate the retention of nanoparticles in the sandstone core.
- Flooding experiments should have been performed at different injection rates. A correlation between particle size and flow rate may exist, meaning a given particle size will have the greatest potential for mobilizing oil at a certain flow rate. For example, small particles are more easily transported through the core. Thus, they might require a lower flow rate in order to fully exploit their potential.
- The potential of nanoparticles are, among other things, related to the salinity of the carrying fluid. It would therefore be interesting to see if/how the oil recovery varied with the salt content of the brine. According to theory, the silica nanoparticles should be more reactive at low salinities and therefore more effective at lowering interfacial tension and alter wettability, in addition to increased stability. Combining nanoparticles with low salinity injection might be an effective EOR technique.
- During the flooding experiments of this thesis, continuous injection of nanofluids were used. Another possibility (which was not tested) is alternating brine and nanofluid as the injection fluid. The nanofluid "slugs" could potentially mobilize more oil, while the brine can desorb retained particles and prevent

major porosity/permeability impairment. In addition, less nanoparticles is required for this process, making it a cheaper alternative.

Symbols

A	area/cross-section	m^2
c	concentration	g/L
C	compressibility	m^2/N
D_{app}	diameter	m
F_σ	free energy	N
G	Gibbs free energy	J
J_D	optical correction factor	-
k	permeability	m^2
k_{ej}	effective permeability of fluid "j"	m^2
k_{rj}	relative permeability of fluid "j"	m^2
L	Length of core plug	m
m	mass of fluid	kg
M	mobility factor	-
n	refractive index	-
P_c	capillary pressure	Pa
q	volume flow	m^3/s
r	radius of curved interface	m
S_i	saturation of fluid "i"	fraction
T	temperature	Celsius or Kelvin
u	velocity	m/s
V_b	bulk volume	m^3
V_g	grain volume	m^3
V_i	fluid volume	m^3
V_p	pore volume	m^3
κ^{-1}	length of the EDL	m
ρ	density	kg/m^3

τ	shear stress	N/m ²
γ	interfacial tension	N/m
γ_{ij}	interfacial tension between "i" and "j"	N/m
ω	angular velocity	rad/s
θ	contact angle	rad
ϕ	porosity	frac
μ	viscosity	Pa s
ν	kinematic viscosity	m ² /s

Abbreviations

CCC	Critical Coagulation Concentration
CMC	Critical Micelle Concentration
CNC	Critical Nanoparticle Concentration
DI	De-ionized (water)
EDL	Electrical Double Layer
EOR	Enhanced Oil Recovery
HLP	Hydrophobic/Lipophilic Nanoparticles
IFT	Interfacial Tension
LHP	Hydrophilic/Lipophobic Nanoparticles
NP	Nanoparticles
SNP	Silica Nanoparticles
VG	Vonnegut
YL	Young-Laplace equation
wt%	Weight percent

References

- Aurand, K., Dahle, G., and Torsaeter, O. Comparison of oil recovery for six nanofluids in berea sandstone cores. 2014.
- Balasubramanian, G., Sen, S., and Puri, I. K. Shear viscosity enhancement in waternanoparticle suspensions. 2011.
- Batychy, J. P. and McCaffery, F. G. Low interfacial tension displacement studies. 1978. doi: 10.2118/78-29-26.
- Bear, J. and Bachmat, Y. *Introduction to Modeling of Transport Phenomena in Porous Media*. Springer, 1990. ISBN 9780792305576. URL <http://books.google.no/books?id=M0aoeI9aAc0C>.
- Berea Sandstone Cores. Petroleum cores. URL <http://www.bereasantonecores.com/>.
- Binks, B. Particles as surfactants - similarities and differences. 2002.
- Binks, B. and Lumsdon, S. Pickering emulsions stabilized by monodisperse latex particles: Effects of particle size. 2001. doi: <http://dx.doi.org/10.1021/la0103822>.
- Binks, B. and Whitby, C. Nanoparticle silica-stabilised oil-in-water emulsions: improving emulsion stability. 2004. doi: <http://dx.doi.org/10.1016/j.colsurfa.2004.10.116>.
- Bolandtaba, S., Skauge, A., and MacKay, E. Pore scale modelling of linked polymer solution (lps) - a new eor process. 2009.
- Caldelas, F., Murphy, M., Huh, C., and Bryant, S. Factors governing distance of nanoparticle propagation in porous media. 2011. doi: <http://dx.doi.org/10.2118/142305-MS>.

- Chengara, A., Nikolov, A. D., Wasan, D. T., Trokhymchuk, A., and Henderson, D. Spreading of nanofluids driven by the structural disjoining pressure gradient. *Journal of Colloid and Interface Science*, 280:192–201, 2004. ISSN 0021-9797. doi: <http://dx.doi.org/10.1016/j.jcis.2004.07.005>.
- Chu, X. L., Nikolov, A. D., and Wasan, D. T. Effects of particle size and polydispersity on the depletion and structural forces in colloidal dispersions. 1996. doi: <http://dx.doi.org/10.1021/la960359u>.
- Civan, F. *Reservoir Formation Damage*. 2000.
- Craft, B., Hawkins, M., and Terry, R. *Applied petroleum reservoir engineering*. Prentice Hall, 1991. ISBN 9780130398840. URL <http://books.google.no/books?id=uDFQAQAIAAJ>.
- Dahle, G. S. The Effect of Nanoparticles on Oil/Water Interfacial Tension. Project thesis, NTNU, 2013.
- Daugherty, R., Franzini, J., and Finnemore, E. *Fluid mechanics with engineering applications*. McGraw-Hill, 1985. ISBN 9780070154414. URL <http://books.google.no/books?id=QphRAAAAMAAJ>.
- Engeset, B. The Potential of Hydrophilic Silica Nanoparticles for EOR Purposes. Master, NTNU, 2013.
- Evdokimov, I. N., Eliseev, N. Y., Losev, A. P., and Novikov, M. A. Emerging petroleum-oriented nanotechnologies for reservoir engineering. 2006. doi: 10.2118/102060-ms.
- Fielden, M. L., Hayes, R. A., and Johnn, R. Oscillatory and ion-correlation forces observed in direct force measurements between silica surfaces in concentrated cacl₂ solutions. 2000. doi: <http://dx.doi.org/10.1039/b001672l>.
- Frijters, S., Gunther, F., and Harting, J. Effects of nanoparticles and surfactant on droplets in shear flow. 2012. doi: 10.1039/C2SM25209K.
- Gao, C. Factors affecting particle retention in porous media. 2008.
- Heiserman, D. *Exploring Chemical Elements and Their Compounds*. McGraw-Hill, 1991. ISBN 9780830630158. URL <http://books.google.no/books?id=241-Cpa19oIC>.

- Hendraningrat, L., Torsæter, O., Engeset, B., and Suwarno, S. Improved oil recovery by nanofluids flooding: An experimental study. 2012. doi: 10.2118/163335-ms. URL <http://www.onepetro.org/mslib/app/Preview.do?paperNumber=SPE-163335-MS&societyCode=SPE>.
- Hendraningrat, L., Engeset, B., Suwarno, S., Li, S., and Torsaeter, O. Laboratory investigation of porosity and permeability impairments in berea sandstones due to hydrophilic nanoparticle retention. 2013a.
- Hendraningrat, L., Li, S., and Torsæter, O. A coreflood investigation of nanofluid enhanced oil recovery. 2013b.
- Hendraningrat, L., Torsaeter, O., and Li, S. Enhancing oil recovery of low-permeability berea sandstone through optimised nanofluids concentration. 2013c. doi: 10.2118/165283-MS.
- Hendraningrat, L., Torsæter, O., and Li, S. Enhancing oil recovery of low-permeability berea sandstone through optimised nanofluids concentration. 2013d. doi: 10.2118/165283-ms. URL <http://www.onepetro.org/mslib/app/Preview.do?paperNumber=SPE-165283-MS&societyCode=SPE>.
- Hendraningrat, L., Torsæter, O., and Li, S. A coreflood investigation of nanofluid enhanced oil recovery in low-medium permeability berea sandstone. 2013e. doi: 10.2118/164106-ms.
- Hendraningrat, L., Torseater, O., and Li, S. Effect of some parameters influencing enhanced oil recovery process using silica nanoparticles: An experimental investigation. 2013f. doi: 10.2118/165955-ms. URL <http://www.onepetro.org/mslib/app/Preview.do?paperNumber=SPE-165955-MS&societyCode=SPE>.
- Hiemenz, P. and Rajagopalan, R. *Principles of Colloid and Surface Chemistry, Third Edition, Revised and Expanded*. Taylor and Francis, 1997. ISBN 9781420001297. URL <http://books.google.no/books?id=CBvrS8rfPLYC>.
- Hocott, C. R. *Interfacial Tension between Water and Oil under Reservoir Conditions*. 1939. ISBN 0096-4778. doi: 10.2118/939184-g.
- Jadhunandan, P. and Morrow, N. Effect of wettability on waterflood recovery for crude-oil/brine/rock systems. *SPE Reservoir Engineering*, 10(1):40–46, 1995. doi: <http://dx.doi.org/10.2118/22597-pa>.

- Kaasa, A. T. Investigation of how Silica Nanoparticle Adsorption Affects Wettability in Water-Wet Berea Sandstone. Master, NTNU, 2013.
- Khilar, K. and Fogler, H. *Migration of Fines in Porous Media*. Springer, 1998. ISBN 9780792352846. URL <http://books.google.no/books?id=XHH-Kn19B0gC>.
- Kong, X. and Ohadi, M. Applications of micro and nano technologies in the oil and gas industry - an overview of recent progress. 2010. doi: <http://dx.doi.org/10.2118/138241-MS>.
- Lake, L. W. *Enhanced Oil Recovery*. Prentice Hall, Englewood Cliffs, New Jersey 07632, 1989.
- Lara, L. d., Micheleon, M., Metin, C., Nguyen, Q., and Miranda, C. Interface tension of silica hydroxylated nanoparticle with brine: A combined experimental and molecular dynamics study. 136, 2012. doi: <http://dx.doi.org/10.1063/1.4705525>.
- Li, S., Hendraningrat, L., and Torsæter, O. Improved oil recovery by hydrophilic silica nanoparticles suspension: 2-phase flow experimental studies. 2013a. doi: [10.2523/16707-ms](http://dx.doi.org/10.2523/16707-ms). URL <http://www.onepetro.org/mslib/app/Preview.do?paperNumber=IPTC-16707-MS&societyCode=IPTC>.
- Li, S., Kaasa, A. T., Torsæter, O., and Hendraningrat, L. Effect of silica nanoparticles adsorption on the wettability index of Berea sandstone. 2013b.
- Ling, K. and Shen, Z. Effects of fluid and rock properties on reserves estimation. 2011. doi: [10.2118/148717-ms](http://dx.doi.org/10.2118/148717-ms). URL <http://www.onepetro.org/mslib/app/Preview.do?paperNumber=SPE-148717-MS&societyCode=SPE>.
- Mcelfresh, P. M., Holcomb, D. L., and Ector, D. Application of nanofluid technology to improve recovery in oil and gas wells. 2012. doi: [10.2118/154827-ms](http://dx.doi.org/10.2118/154827-ms).
- Miranda, C. R., Lara, L. S. d., and Tonetto, B. C. Stability and mobility of functionalized silica nanoparticles for enhanced oil recovery applications. 2012. doi: [10.2118/157033-ms](http://dx.doi.org/10.2118/157033-ms). URL <http://www.onepetro.org/mslib/app/Preview.do?paperNumber=SPE-157033-MS&societyCode=SPE>.
- Moghadasli, J., Steinhagen, H., Jamialahmadi, M., and Sharif, A. Theoretical and experimental study of particle movement and deposition in porous media during water injection. 2004.

- Morrow, N. R. Wettability and its effect on oil recovery. *Journal of Petroleum Technology*, 42(12):1476–1484, 1990. doi: <http://dx.doi.org/10.2118/21621-pa>.
- MPG Petroleum. Oil and & gas fundamentals, 2003. URL www.mpgpetroleum.com/fundamentals.html.
- Nanowerk. Introduction to nanotechnology. URL www.nanowerk.com/nanotechnology/introduction/.
- Ogolo, N., Olafuyi, O., and Onyekonwu, M. Enhanced oil recovery using nanoparticles. 2012. doi: 10.2118/160847-ms. URL <http://www.onepetro.org/mslib/app/Preview.do?paperNumber=SPE-160847-MS&societyCode=SPE>.
- Owens, W. and Archer, D. The effect of rock wettability on oil-water relative permeability relationships. *Journal of Petroleum Technology*, 23(7):873–878, 1971. doi: <http://dx.doi.org/10.2118/3034-pa>.
- Pedersen, K. S., Lund, T., and Fredenslund, A. Surface tension of petroleum mixtures. *Journal of Canadian Petroleum Technology*, 28(2), 1989. doi: 10.2118/89-02-12. URL <http://www.onepetro.org/mslib/app/Preview.do?paperNumber=PETSOC-89-02-12&societyCode=PETSOC>.
- Pittman, E. D. Relationship of porosity and permeability to various parameters derived from mercury injection-capillary pressure curves for sandstone. 1992.
- Shanker, N. S., Chandra Shekar Reddy, M., and Basava Rao, V. V. On prediction of viscosity of nanofluids for low volume fractions of nanoparticles. 1, 2012.
- Sharpa, E., Al-Shehria, H., Horozova, T., Stoyanovbcd, S., and Paunova, V. Adsorption of shape-anisotropic and porous particles at the airwater and the decanewater interface studied by the gel trapping technique. 2013. doi: <http://dx.doi.org/10.1039/C3RA44563A>.
- Skauge, T., Spildo, K., and Skauge, A. Nano-sized particles for eor, 2010. URL <http://www.onepetro.org/mslib/app/Preview.do?paperNumber=SPE-129933-MS&societyCode=SPE>.
- Suleimanov, F., Ismailov, F., and Veliyev, E. Nanofluid for enhanced oil recovery. 2011. doi: <http://dx.doi.org/10.1016/j.petrol.2011.06.014>.

- Tichelkamp, T., Vu, Y., Nourani, M., and Øye, G. Interfacial tension between low salinity solutions of sulfonate surfactants and crude and model oils. 2014. doi: dx.doi.org/10.1021/ef4024959.
- Todd, A., Somerville, J., and Scott, G. The application of depth of formation damage measurements in predicting water injectivity decline. 1984. doi: <http://dx.doi.org/10.2118/12498-MS>.
- Torsæter, O. Interfacial Tension. Lecture Notes - Carbonate Reservoir Characteristics MSc Course. 2012.
- Torsæter, O. and Abtahi, M. *Experimental Reservoir Engineering Laboratory Work Book*. 2000.
- Trube, A. S. *Compressibility of Undersaturated Hydrocarbon Reservoir Fluids*. 1957.
- Vafaei, S., Borca-Tasciuc, T., Podowski, M. Z., Purkayastha, A., Ramanath, G., and Ajayan, P. M. Effect of nanoparticles on sessile droplet contact angle. 17: 2523, 2006. doi: 10.1088/0957-4484/17/10/014.
- Vetter, O. J., Kandarpa, V., Stratton, M., and Veith, E. Particle invasion into porous medium and related injectivity problems. 1987. doi: <http://dx.doi.org/10.2118/16255-MS>.
- Vevle, J. NMR measurements of wettability alternation in Berea Sandstone. Master, UiB, 2011.
- Viades-Trejo, J. and Gracia-Fadrique, J. Spinning drop method: From younglaplace to vonnegut. *Colloids and Surfaces A: Physicochemical and Engineering Aspects*, 302(13):549–552, 2007. ISSN 0927-7757. doi: <http://dx.doi.org/10.1016/j.colsurfa.2007.03.033>. URL <http://www.sciencedirect.com/science/article/pii/S0927775707002567>.
- Vonnegut, B. Rotating bubble method for the determination of surface and interfacial tensions. *Review of Scientific Instruments*, 13(1):6–9, 1942. doi: <http://dx.doi.org/10.1063/1.1769937>. URL <http://scitation.aip.org/content/aip/journal/rsi/13/1/10.1063/1.1769937>.
- Wasan, D., Nikolov, A., and Kondiparty, K. The wetting and spreading of nanofluids on solids: Role of the structural disjoining pressure. *Current Opinion in Colloid and Interface Science*, 16(4):344–349, 2011.

- Wasan, D. T. and Nikolov, A. D. Spreading of nanofluids on solids. *Nature*, 423(6936):156–159, 2003. ISSN 0028-0836. doi: <http://dx.doi.org/10.1038/nature01591>. 10.1038/nature01591.
- Whitson, C. and Brulè, M. *Phase behavior*. Henry L. Doherty Memorial Fund of AIME, Society of Petroleum Engineers, 2000. ISBN 9781555630874. URL <http://books.google.no/books?id=Z4cQAQAAMAAJ>.
- Wisconsin Geological Survey. Rock properties: Porosity and density, 2010. URL http://wisconsingeologicalsurvey.org/porosity_density/about_porosity_density.html.
- Xu, Y. Dynamic interfacial tension between bitumen and aqueous sodium hydroxide solutions. 1995. doi: dx.doi.org/10.1021/ef00049a022.
- Yu, J., Berlin, J. M., Lu, W., Zhang, L., Kan, A. T., Zhang, P., Walsh, E. E., Work, S., Chen, W., Tour, J., Wong, M., and Tomson, M. B. Transport study of nanoparticles for oilfield application. 2010. doi: <http://dx.doi.org/10.2118/131158-ms>.
- Zhang, H., Nikolov, A., and Wasan, D. Enhanced oil recovery (eor) using nanoparticle dispersions: Underlying mechanism and imbibition experiments. 2014. doi: <http://dx.doi.org/10.1021/ef500272r>.
- Zhang, T., Davidson, D., Lawrence, S., and Huh, C. Nanoparticle-stabilized emulsions for applications in enhanced oil recovery. 2010. doi: <http://dx.doi.org/10.2118/129885-MS>.
- Zhang, T., Huh, C., Yu, H., Nielson, B., Yoon, K. Y., Bagaria, H., Johnston, K., Murphy, M., Bryant, S., and Bielawski, C. Investigation of nanoparticle adsorption during transport in porous media, 2013.
- Zolotukhin, A. and Ursin, J. *Introduction to Petroleum Reservoir Engineering*. Hyskoleforlaget, Norwegian Academic Press, 2000. ISBN 9788276340655. URL <http://books.google.no/books?id=eiwAGQAACAAJ>.

Appendix A

Core Data

TABLE A.1: Core dimensions and porosity.

Core Nr	V_1 cm^3	V_2 cm^3	D cm	L cm	V_b cm^3	V_g cm^3	V_p cm^3	Porosity %
1H	169	48,2	3,791	13,668	154,28	120,8	33,48	21,70
2H	169	47,0	3,787	13,432	151,29	122,0	29,29	19,36
3H	169	49,2	3,778	13,422	150,46	119,8	30,66	20,37
4H	169	48,2	3,786	13,423	151,11	120,8	30,31	20,06
5H	169	48,0	3,782	13,584	152,60	121,0	31,60	20,70
6H	169	47,3	3,781	13,492	151,49	121,7	29,79	19,66
7H	169	47,5	3,780	13,420	150,60	121,5	29,10	19,32
8H	169	46,3	3,784	13,419	150,91	122,7	28,21	18,69
9H	169	46,9	3,784	13,411	150,82	122,1	28,72	19,04
10H	169	47,7	3,776	13,415	150,23	121,3	28,93	19,25
1M	169	51,0	3,827	12,953	149,00	118,0	31,00	20,80
2M	211	92,0	3,801	12,960	147,06	119,0	28,06	19,08
3M	211	91,0	3,803	12,961	147,22	120,0	27,22	18,49
4M	169	49,3	3,795	12,976	146,78	119,7	27,08	18,44
5M	169	48,0	3,804	12,945	147,12	121,0	26,12	17,75
6M	169	48,5	3,799	12,980	147,13	120,5	26,63	18,10
7M	169	48,9	3,798	12,954	146,76	120,1	26,66	18,16
8M	169	49,1	3,792	12,970	146,48	119,9	26,58	18,14
9-1	169	48,0	3,808	13,012	148,19	121,0	27,19	18,35
9-2	169	48,0	3,805	13,02	148,05	121,0	27,05	18,27
9-3	169	48,4	3,803	13,012	147,80	120,6	27,20	18,41
9-4	169	47,4	3,794	13,008	147,06	121,6	25,46	17,31
9-5	169	47,0	3,793	13,011	147,02	122,0	25,02	17,02
9-6	169	47,0	3,795	13,023	147,31	122,0	25,31	17,18
9-7	169	48,0	3,795	13,018	147,25	121,0	26,25	17,83

TABLE A.2: Core dimensions and porosity.

Core Nr	V_1 cm^3	V_2 cm^3	D cm	L cm	V_b cm^3	V_g cm^3	V_p cm^3	Porosity %
9-8	169	48,0	3,792	13,008	146,91	121,0	25,91	17,63
9-9	169	47,2	3,793	13,014	147,05	121,8	25,25	17,17
9-10	169	48,3	3,780	13,023	146,15	120,7	25,45	17,41

TABLE A.3: Pore volume of the cores.

Core Nr	Dry Weight g	Wet Weight g	Pore Volume cm^3
1H	320,8	350,2	28,42
2H	321,6	350,9	28,34
3H	320,1	349,9	28,82
4H	321,1	350,4	28,35
5H	319,8	349,5	28,66
6H	321,5	350,8	28,36
7H	320,9	350,5	28,64
8H	323,9	352,4	27,61
9H	321,9	351,1	28,23
10H	320,2	349,7	28,56
1M	322,4	348,1	24,75
2M	319,3	345,6	25,42
3M	320,7	346,3	24,81
4M	317,7	344,7	26,13
5M	321,6	347,2	24,71
6M	323,1	347,1	23,18
7M	319,6	345,9	25,42
8M	319,3	345,6	25,40
9-1	317,33	344,3	26,06
9-2	317,31	344,3	26,05
9-3	316,02	343,6	26,67
9-4	317,55	344,1	25,64
9-5	319,2	345,6	25,50
9-6	319,2	345,2	25,05
9-7	316,63	342,8	25,29
9-8	316,93	344,0	26,18
9-9	319,01	345,1	25,22
9-10	316,4	343,0	25,70

TABLE A.4: Mineral analysis of the cores, five samples from each block.

Block	Sample	Quartz %	Microline %	Diopside %	Kaolinite %
H	1	96,98	2,73	-	0,29
H	2	97,70	2,13	-	0,17
H	3	96,76	2,91	-	0,34
H	4	96,88	2,82	-	0,29
H	5	98,23	1,66	-	0,11
M	1	94,59	3,94	1,47	-
M	2	93,10	5,67	1,23	-
M	3	92,99	5,65	1,36	-
M	4	94,84	4,07	1,09	-
M	5	93,06	5,62	1,32	-

TABLE A.5: Air permeability measurements and Klinkenberg Corrections.

Core	Length cm	Radius cm	P ₁ bar	P ₂ bar	ΔP bar	Q L/min	1/P _m 1/bar	Air Perm. mD	Liq. Perm. mD
1H	13,668	1,896	1,2	1,0	0,2	0,83	0,91	1362,9	725,1
			1,4	1,2	0,2	0,93	0,77	1292,2	
			1,6	1,4	0,2	1,03	0,67	1240,3	
			1,8	1,6	0,2	1,05	0,59	1115,6	
2H	13,432	1,894	1,2	1,0	0,2	0,83	0,91	1342,2	714,1
			1,4	1,2	0,2	0,93	0,77	1272,5	
			1,6	1,4	0,2	1,03	0,67	1221,5	
			1,8	1,6	0,2	1,05	0,59	1098,8	
3H	13,422	1,889	1,2	1,0	0,2	0,75	0,91	1217,7	666,3
			1,4	1,2	0,2	0,83	0,77	1140,3	
			1,6	1,4	0,2	0,89	0,67	1059,7	
			1,8	1,6	0,2	0,98	0,59	1029,6	
4H	13,423	1,893	1,2	1,0	0,2	0,54	0,91	873,1	414,3
			1,4	1,2	0,2	0,59	0,77	807,2	
			1,6	1,4	0,2	0,68	0,67	806,3	
			1,8	1,6	0,2	0,7	0,59	732,4	
			1,9	1,7	0,2	0,71	0,56	701,5	
			2,0	1,8	0,2	0,75	0,48	635,2	
5H	13,584	1,891	1,2	1,0	0,2	0,83	0,91	1361,0	601,9
			1,4	1,2	0,2	0,87	0,77	1207,1	
			1,6	1,4	0,2	0,95	0,67	1142,3	
			1,8	1,6	0,2	1,04	0,59	1103,4	
			1,9	1,7	0,2	1,05	0,56	1052,2	
6H	13,492	1,891	1,2	1,0	0,2	0,77	0,91	1254,7	654,5
			1,4	1,2	0,2	0,88	0,77	1213,3	
			1,6	1,4	0,2	0,94	0,67	1123,3	
			1,8	1,6	0,2	0,99	0,59	1043,8	
			1,9	1,7	0,2	1,03	0,56	1025,7	
7H	13,420	1,890	1,2	1,0	0,2	0,80	0,91	1297,3	635,8
			1,4	1,2	0,2	0,89	0,77	1221,2	
			1,6	1,4	0,2	0,97	0,67	1153,5	
			1,8	1,6	0,2	1,00	0,59	1049,3	
8H	13,419	1,892	1,2	1,0	0,2	0,69	0,91	1116,5	505,89
			1,4	1,2	0,2	0,79	0,77	1081,6	
			1,6	1,4	0,2	0,84	0,67	996,8	
			1,8	1,6	0,2	0,86	0,59	900,4	
			1,9	1,7	0,2	0,89	0,56	880,1	
9H	13,411	1,892	1,2	1,0	0,2	0,79	0,91	1277,5	591,8
			1,4	1,2	0,2	0,86	0,77	1176,8	
			1,6	1,4	0,2	0,94	0,67	1114,8	
			1,8	1,6	0,2	0,98	0,59	1025,5	
10H	13,415	1,888	1,2	1,0	0,2	0,59	0,91	958,4	375,6
			1,4	1,2	0,2	0,66	0,77	907,2	
			1,6	1,4	0,2	0,69	0,67	822,0	
			1,8	1,6	0,2	0,73	0,59	767,3	
			1,9	1,7	0,2	0,74	0,56	734,6	
			2,0	1,8	0,2	0,76	0,48	714,8	

TABLE A.6: Air permeability measurements and Klinkenberg Corrections.

Core	Length cm	Radius cm	P ₁ bar	P ₂ bar	ΔP bar	Q L/min	1/P _m 1/bar	Air Perm. mD	Liq. Perm. mD
1M	12,953	1,914	1,2	1,0	0,2	0,40	0,91	610,8	285,1
			1,4	1,2	0,2	0,43	0,77	555,6	
			1,6	1,4	0,2	0,49	0,67	548,7	
			1,8	1,6	0,2	0,50	0,59	494,0	
			1,9	1,7	0,2	0,51	0,56	475,9	
2M	12,953	1,901	1,2	1,0	0,2	0,66	0,91	1021,7	345,0
			1,4	1,2	0,2	0,73	0,77	956,2	
			1,6	1,4	0,2	0,77	0,67	874,1	
			1,8	1,6	0,2	0,79	0,59	791,3	
			1,9	1,7	0,2	0,80	0,56	756,8	
3M	12,961	1,902	1,2	1,0	0,2	0,41	0,91	634,4	362,6
			1,4	1,2	0,2	0,46	0,77	602,3	
			1,6	1,4	0,2	0,51	0,67	578,7	
			1,8	1,6	0,2	0,53	0,59	530,6	
			1,9	1,7	0,2	0,55	0,56	519,2	
4M	12,976	1,898	1,2	1,0	0,2	0,70	0,91	1088,9	437,6
			1,4	1,2	0,2	0,76	0,77	1000,4	
			1,6	1,4	0,2	0,81	0,67	924,0	
			1,8	1,6	0,2	0,85	0,59	855,6	
5M	12,945	1,902	1,2	1,0	0,2	0,42	0,91	648,7	337,1
			1,4	1,2	0,2	0,46	0,77	594,7	
			1,6	1,4	0,2	0,52	0,67	583,3	
			1,8	1,6	0,2	0,54	0,59	539,7	
			1,9	1,7	0,2	0,55	0,56	519,2	
6M	12,980	1,900	1,2	1,0	0,2	0,52	0,91	807,5	393,5
			1,4	1,2	0,2	0,57	0,77	748,9	
			1,6	1,4	0,2	0,61	0,67	694,6	
			1,8	1,6	0,2	0,66	0,59	663,2	
7M	12,954	1,899	1,2	1,0	0,2	0,50	0,91	775,3	357,6
			1,4	1,2	0,2	0,53	0,77	695,4	
			1,6	1,4	0,2	0,58	0,67	659,5	
			1,8	1,6	0,2	0,63	0,59	632,1	
			1,9	1,7	0,2	0,64	0,56	606,4	
8M	12,970	1,896	1,2	1,0	0,2	0,53	0,91	825,4	546,1
			1,4	1,2	0,2	0,61	0,77	803,4	
			1,6	1,4	0,2	0,68	0,67	776,6	
			1,8	1,6	0,2	0,71	0,59	715,5	

TABLE A.7: Air permeability measurements and Klinkenberg Corrections.

Core	Length cm	Radius cm	P ₁ bar	P ₂ bar	ΔP bar	Q L/min	1/P _m 1/bar	Air Perm. mD	Liq. Perm. mD
9-1	13,012	1,904	1,2	1,0	0,2	0,74	0,91	1146,5	451,1
			1,4	1,2	0,2	0,79	0,77	1035,7	
			1,6	1,4	0,2	0,85	0,67	965,7	
			1,8	1,6	0,2	0,89	0,59	892,2	
			1,9	1,7	0,2	0,93	0,56	880,5	
9-2	13,020	1,903	1,2	1,0	0,2	0,57	0,91	885,0	453,7
			1,4	1,2	0,2	0,63	0,77	827,7	
			1,6	1,4	0,2	0,68	0,67	774,3	
			1,7	1,5	0,2	0,69	0,59	736,6	
			1,8	1,6	0,2	0,74	0,56	743,5	
9-3	13,012	1,902	1,2	1,0	0,2	0,65	0,91	1009,7	488,1
			1,4	1,2	0,2	0,73	0,77	959,5	
			1,6	1,4	0,2	0,79	0,67	899,9	
			1,8	1,6	0,2	0,82	0,59	824,2	
			1,9	1,7	0,2	0,85	0,56	806,9	
9-4	13,008	1,897	1,2	1,0	0,2	0,64	0,91	998,6	458,3
			1,4	1,2	0,2	0,72	0,77	950,6	
			1,6	1,4	0,2	0,77	0,67	881,0	
			1,8	1,6	0,2	0,81	0,59	817,8	
			1,9	1,7	0,2	0,82	0,56	781,9	
9-5	13,011	1,897	1,2	1,0	0,2	0,62	0,91	968,1	449,6
			1,4	1,2	0,2	0,68	0,77	898,4	
			1,6	1,4	0,2	0,74	0,67	847,4	
			1,8	1,6	0,2	0,77	0,59	778,0	
			1,9	1,7	0,2	0,81	0,56	772,9	
9-6	13,023	1,899	1,2	1,0	0,2	0,58	0,91	905,5	342,4
			1,4	1,2	0,2	0,65	0,77	858,7	
			1,6	1,4	0,2	0,66	0,67	755,7	
			1,7	1,9	0,2	0,68	0,59	729,9	
			1,8	2,0	0,2	0,71	0,56	717,3	
9-7	13,018	1,898	1,2	1,0	0,2	0,76	0,91	1186,1	468,4
			1,4	1,2	0,2	0,84	0,77	1109,3	
			1,6	1,4	0,2	0,89	0,67	1018,6	
			1,7	1,5	0,2	0,92	0,59	987,1	
			1,8	1,6	0,2	0,93	0,56	939,2	
			1,9	1,7	0,2	0,95	0,48	906,1	
9-8	13,008	1,896	1,2	1,0	0,2	0,63	0,91	984,0	559,0
			1,4	1,2	0,2	0,70	0,77	925,1	
			1,6	1,4	0,2	0,77	0,67	882,0	
			1,8	1,6	0,2	0,82	0,59	828,7	

Core	Length cm	Radius cm	P ₁ bar	P ₂ bar	ΔP bar	Q L/min	1/P _m 1/bar	Air Perm. mD	Liq. Perm. mD
9-9	13,014	1,897	1,2	1,0	0,2	0,55	0,91	859,0	419,6
			1,4	1,2	0,2	0,60	0,77	792,9	
			1,6	1,4	0,2	0,64	0,67	733,0	
			1,7	1,9	0,2	0,69	0,59	697,8	
			1,8	2,0	0,2	0,73	0,56	623,9	
9-10	13,023	1,890	1,2	1,0	0,2	0,69	0,91	1085,8	434,1
			1,4	1,2	0,2	0,76	0,77	1012,0	
			1,6	1,4	0,2	0,80	0,67	923,2	
			1,7	1,9	0,2	0,84	0,59	855,3	
			1,8	2,0	0,2	0,87	0,56	836,7	

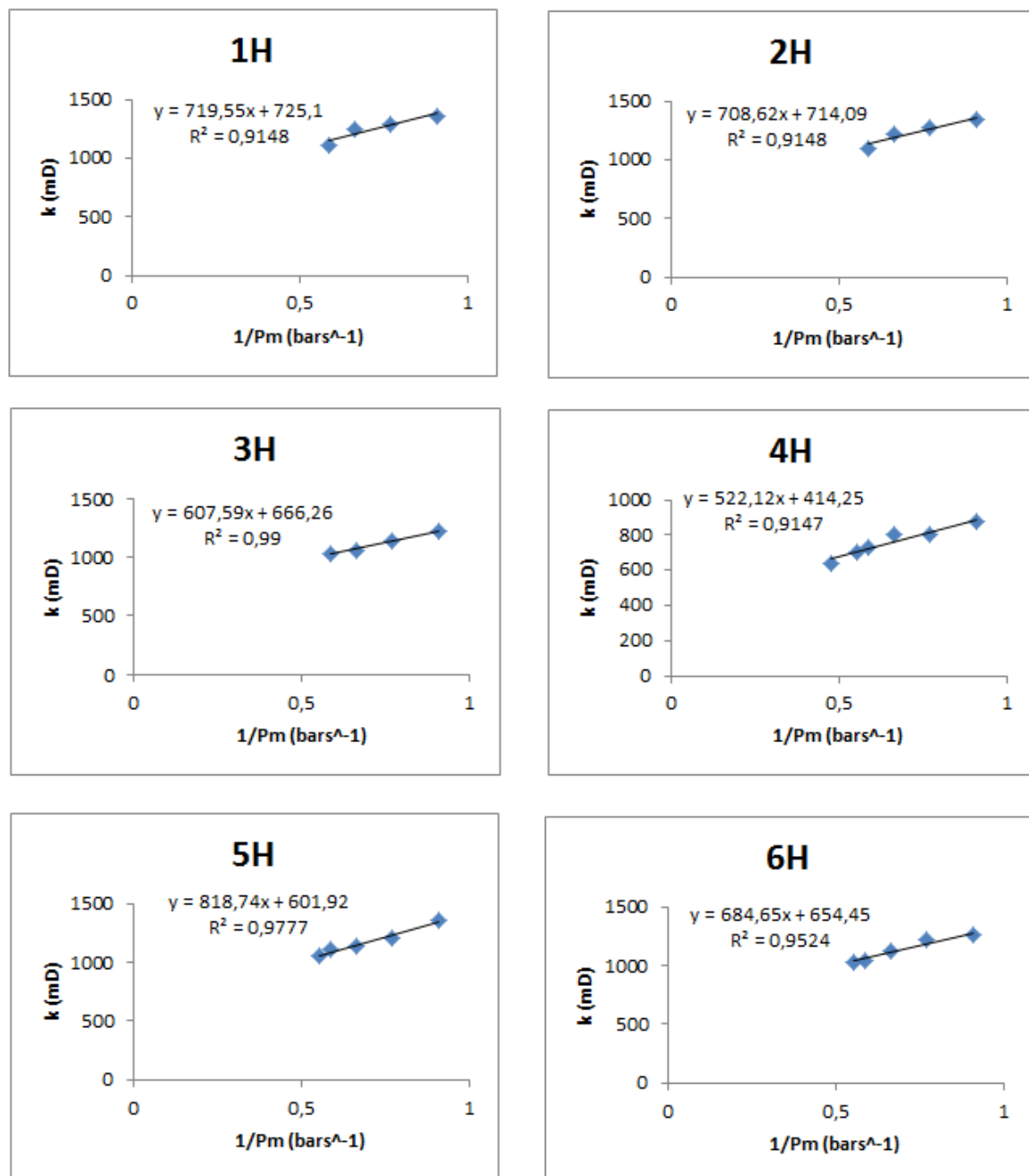


FIGURE A.1: Klinkenberg Plots for core 1H-6H.

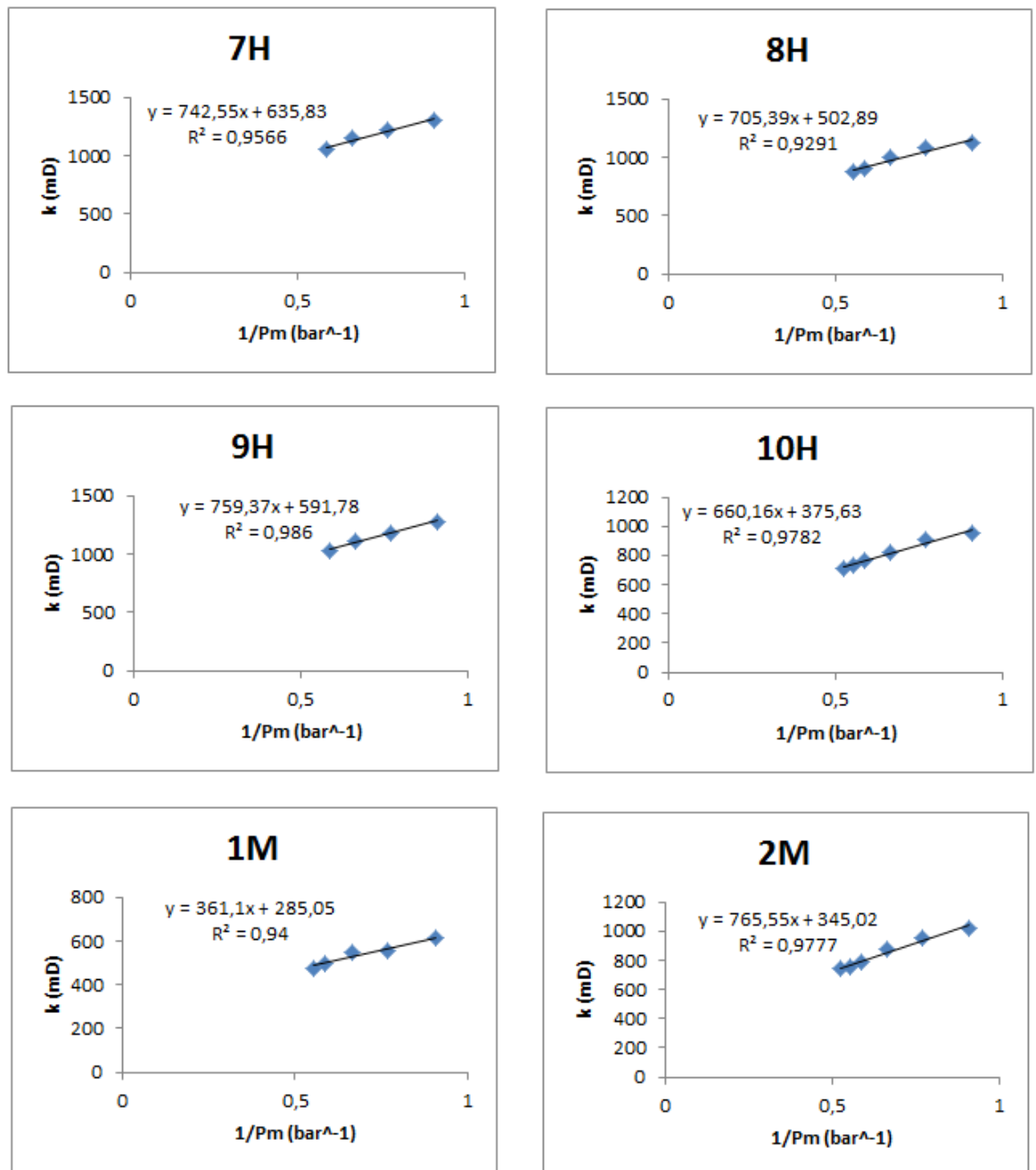


FIGURE A.2: Klinkenberg Plots for core 7H-10H and 1M-2M.

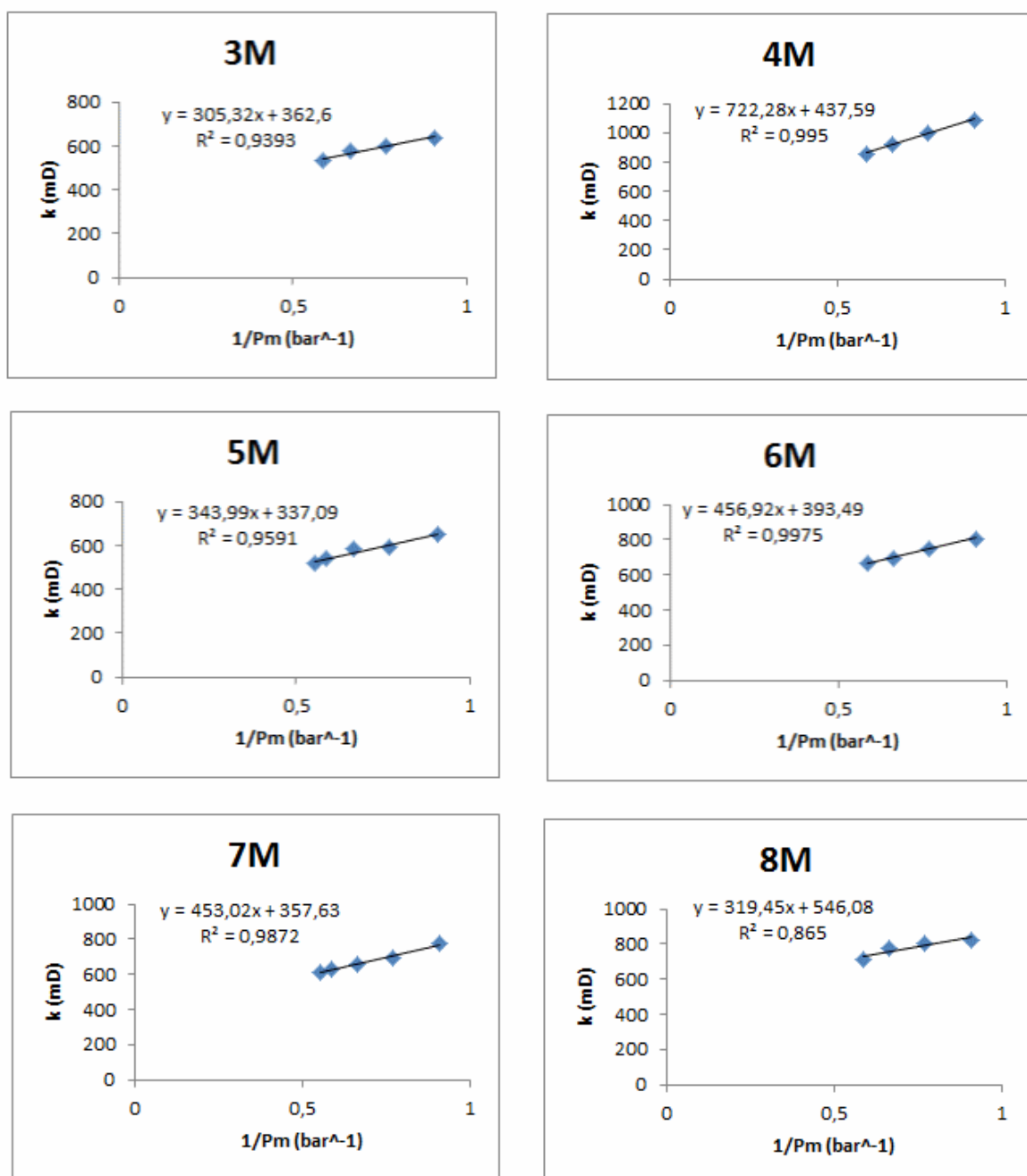


FIGURE A.3: Klinkenberg Plots for core 3M-8M.

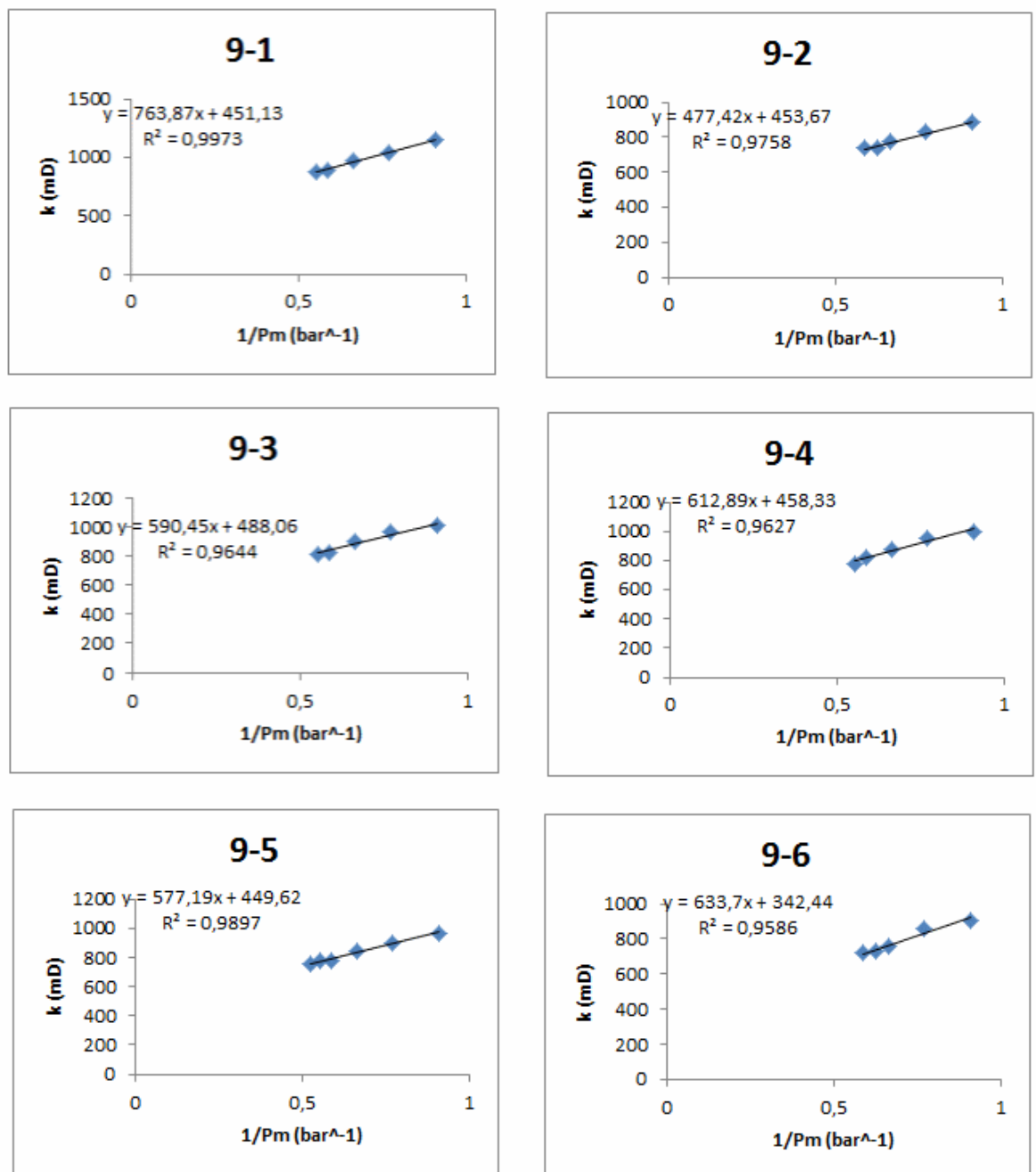


FIGURE A.4: Klinkenberg Plots for core 9-1 to 9-6.

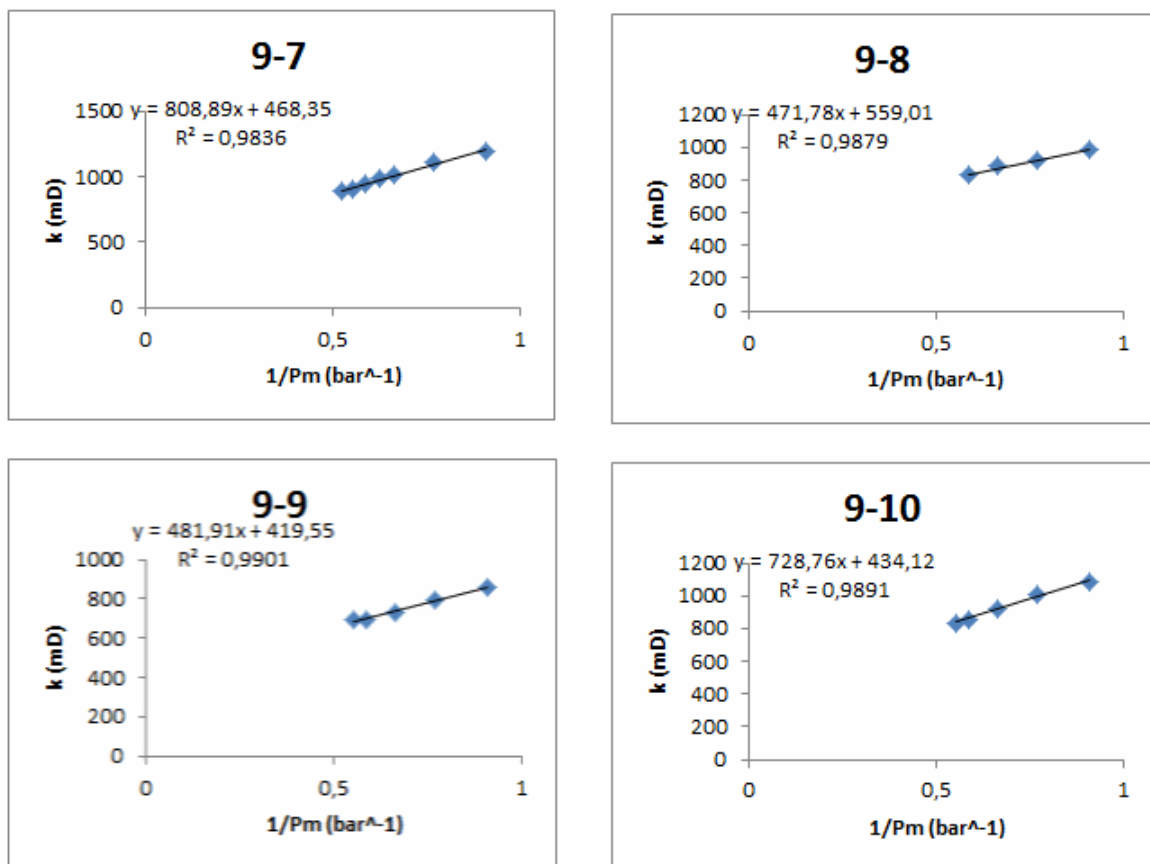


FIGURE A.5: Klinkenberg Plots for core 9-7 to 9-10.

Appendix B

Nanofluid Properties

This appendix will present all relevant fluid data gathered during the experiments. A graphical presentation for all the contact angles will be shown. The average of the two contact angles will be used as the final value.

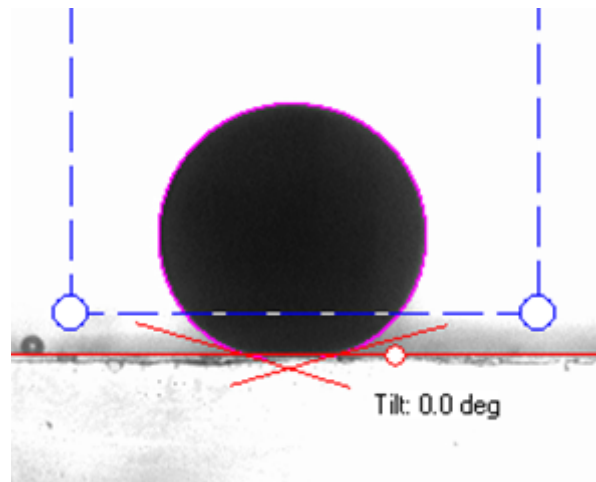


FIGURE B.1: The imaging method for measuring contact angle.

TABLE B.1: Nanofluid properties. Particle and aggregate sizes are presented with average diameter.

Fluid	Type	Particle Size (D) nm	Surface Area m^2/g	Aggregate Size (D) nm	Stabilizer
AERODISP W 7620 N	Fumed	7	300	105	NaOH
AERODISP W 7320 N	Fumed	16	130	116	NaOH
VP Disp W 3520 XN	Fumed	-	-	70	NaOH
IDISIL IC 0820	Colloidal	8	350	18	NaOH
IDISIL SI 1530	Colloidal	15	150	30	NaOH
IDISIL EM 7520 K	Colloidal	-	65	75	Potassium

TABLE B.2: Measured fluid properties at 22,8°C.

Fluid	Concentration wt%	Temperature °C	Density g/cm ³	Viscosity cP	Contact Angle Degrees	Refractive Index	IFT mN/m
North Sea Brine	-	22,8	1,022	1,08	153,4	1,3390	16,41
AERODISP W 7620 N	0,05	22,8	1,022	0,94	157,2	1,3389	11,65
AERODISP W 7320 N	0,05	22,8	1,025	1,02	158,4	1,3389	12,67
IDISIL IC 0820	0,05	22,8	1,023	0,97	167,9	1,3389	12,99
IDISIL SI 1520	0,05	20,1	1,025	1,02	150,0	1,3393	14,52
VP Disp W 3520 XN	0,05	22,8	1,025	0,97	160,6	1,3389	11,96
IDISIL EM 7520 K	0,05	20,4	1,023	0,91	-	1,3394	12,15

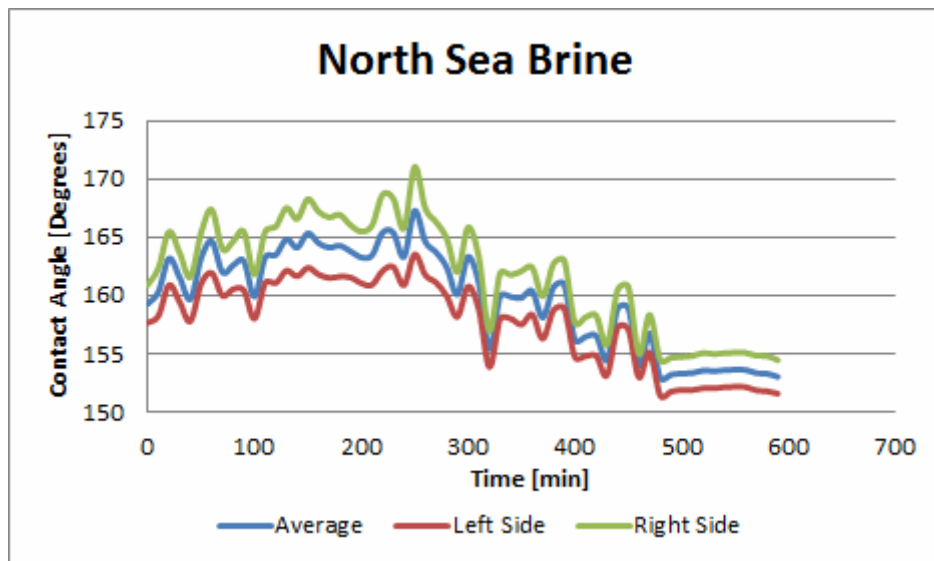


FIGURE B.2: Contact angle measurements of an oil droplet in North Sea Brine.

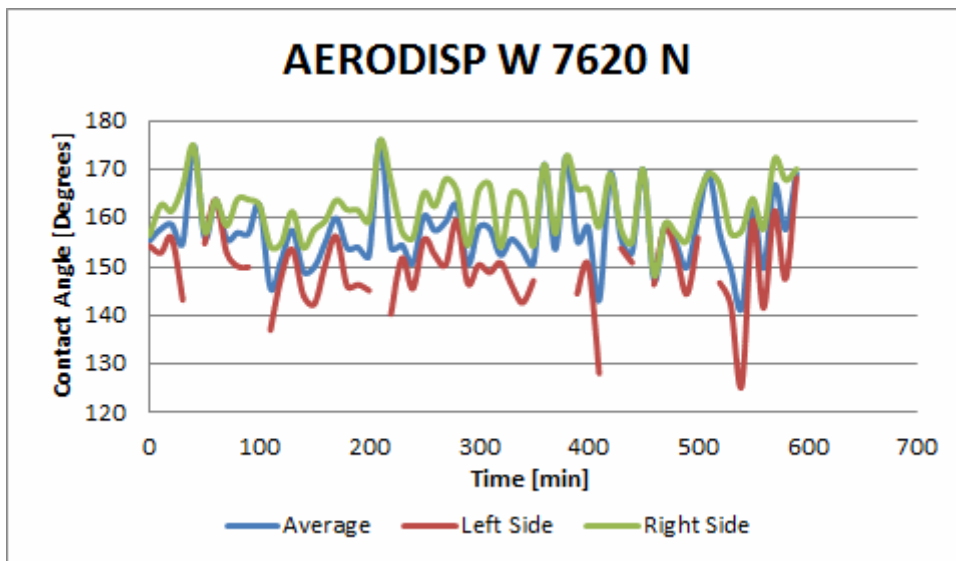


FIGURE B.3: Contact angle measurements of an oil droplet in AERODISP W 7620 N.

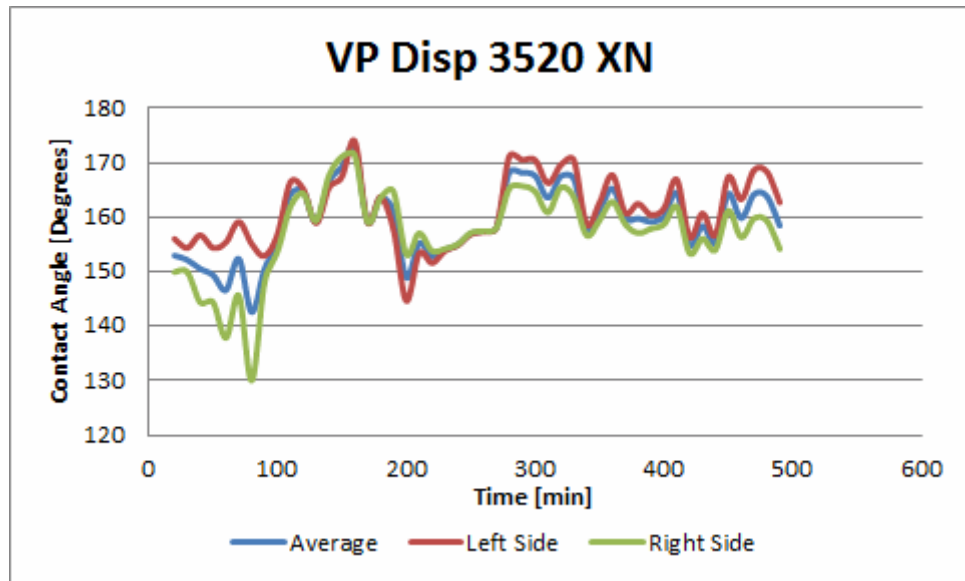


FIGURE B.4: Contact angle measurements of an oil droplet in VP Disp W 3520 N.

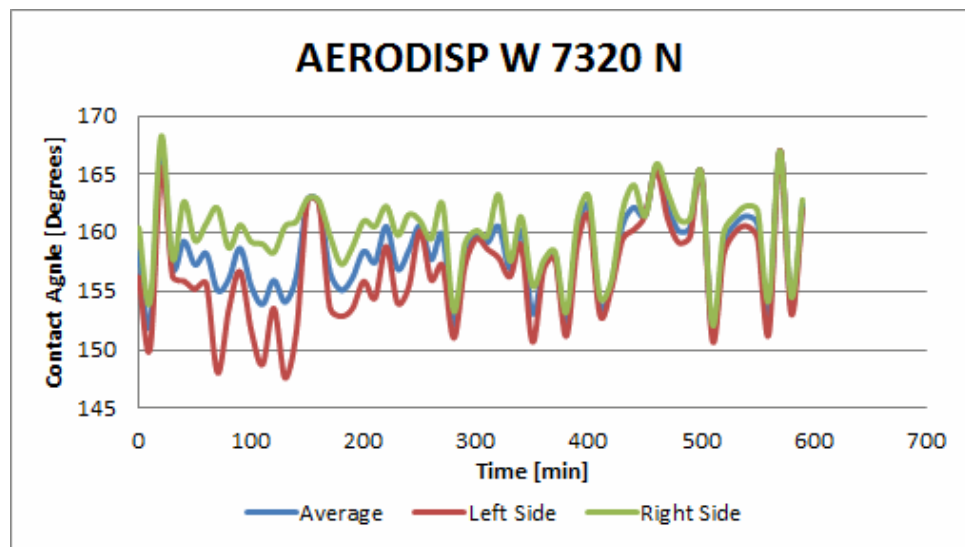


FIGURE B.5: Contact angle measurements of an oil droplet in AERODISP W 7320 N.

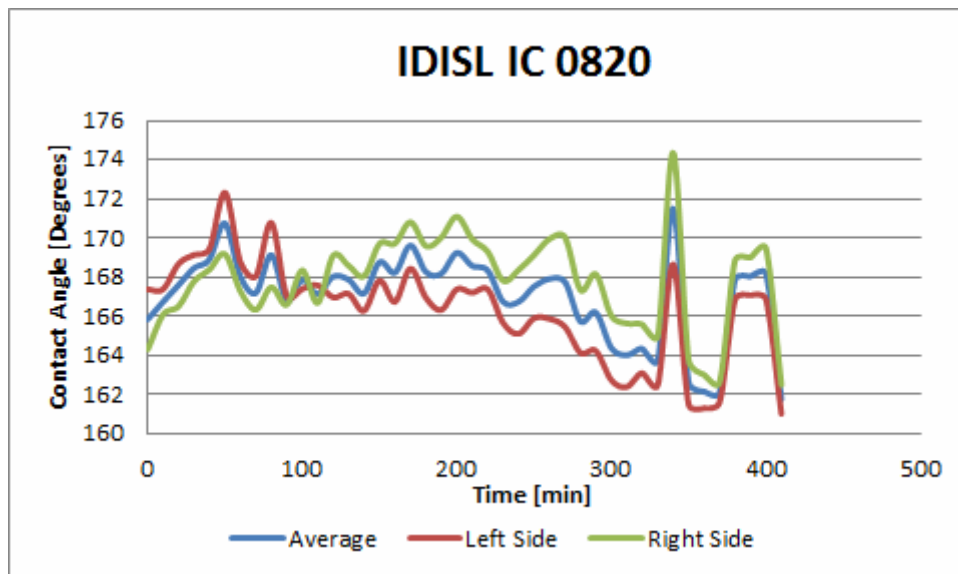


FIGURE B.6: Contact angle measurements of an oil droplet in IDISIL IC 0820.

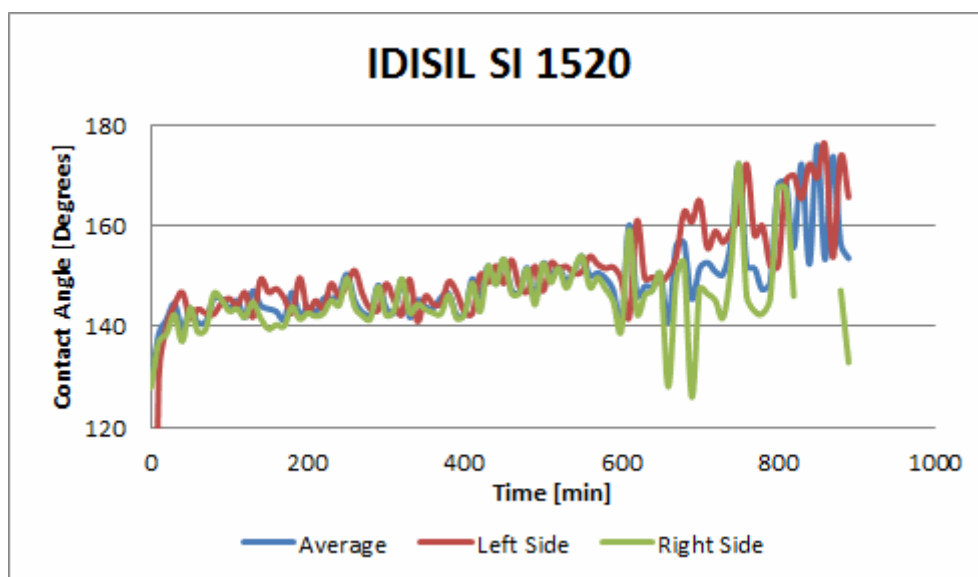


FIGURE B.7: Contact angle measurements of an oil droplet in IDISIL SI 1520.

Appendix C

Flooding Results

This chapter will show graphical and numerical results of all the corefloodings performed. The differential pressure across the core will be plotted, as well as the recovery from each flooding phase.

TABLE C.1: Core flooding summary. The first ten tests used 0,05 wt% nanofluids. The next six tested nanofluids at different concentrations. The last four testes were used to validate the previous results.

Nanofluid	Core	Concentration [wt%]	Swi	Sor ¹	Increased Recovery ² [%]
AERODISP W 7620 N	7M	0,05	0,28	0,41	5,74
AERODISP W 7320 N	6M	0,05	0,27	0,41	11,76
VP Disp W 3520 XN	4M	0,05	0,28	0,50	8,56
IDISIL IC 0820	3M	0,05	0,40	0,38	2,36
IDISIL SI 1520	1M	0,05	0,26	0,30	6,03
IDISIL EM 7520 K	5M	0,05	0,30	0,48	3,48
AERODISP W 7620 N	5H	0,05	0,25	0,47	0,12
AERODISP W 7320 N	1H	0,05	0,23	0,36	0,23
VP Disp W 3520 XN	2H	0,05	0,26	0,30	0,00
IDISIL IC 0820	4H	0,05	0,21	0,51	0,67
IDISIL SI 1520	6H	0,05	0,25	0,49	0,24
IDISIL EM 7520 K	8H	0,05	0,23	0,59	0,00
AERODISP W 7620 N	9-3	0,025	0,33	0,41	0,98
AERODISP W 7620 N	9-2	0,075	0,28	0,45	0,66
VP Disp 3520 XN	9-4	0,025	0,28	0,46	1,76
VP Disp 3520 XN	9-5	0,075	0,34	0,42	1,10
AERODISP W 7320 N	9-1	0,025	0,24	0,45	1,39
AERODISP W 7320 N	8M	0,075	0,28	0,49	1,23
AERODISP W 7320 N	9-7	0,05	0,24	0,49	1,94
AERODISP W 7620 N	9-8	0,05	0,27	0,51	0,81
VP Disp W 3520 XN	9-6	0,05	0,30	0,49	1,46
AERODISP W 7320 N	7H	0,05	0,22	0,47	2,39

¹Residual oil saturation before nanoflooding.

²Increased recovery from the nanoflooding phase.

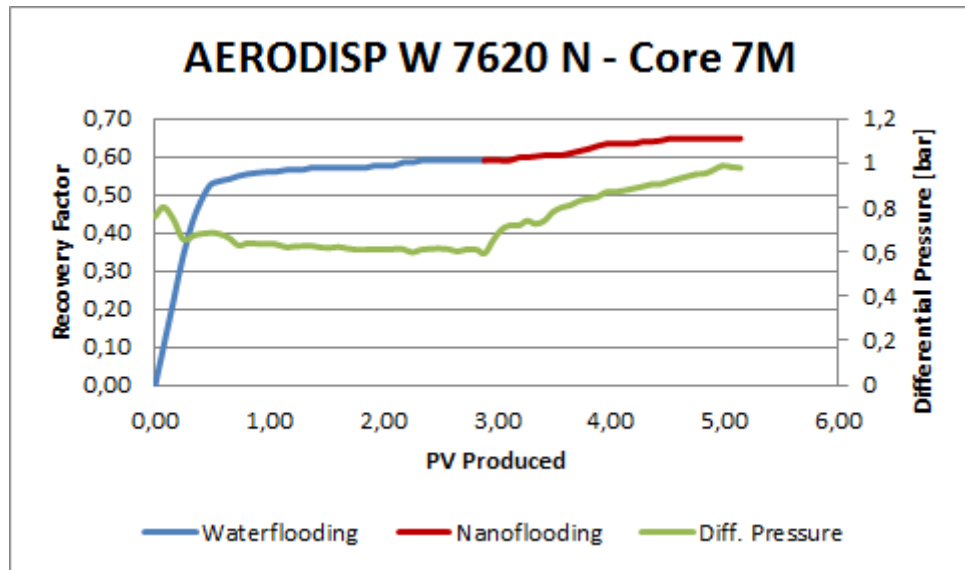


FIGURE C.1: AERODISP W 7620 N flooding in medium permeability core.

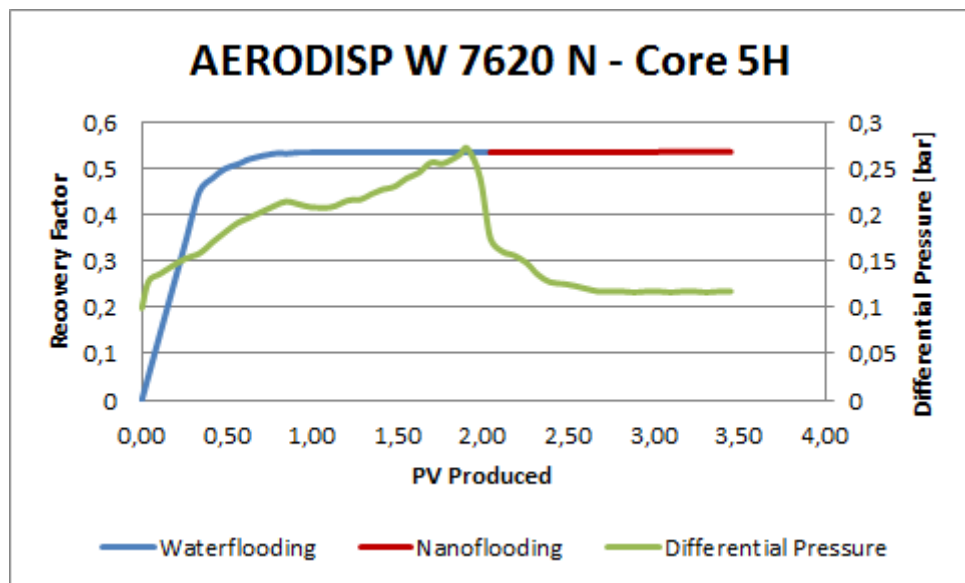


FIGURE C.2: AERODISP W 7620 N flooding in high permeability core.

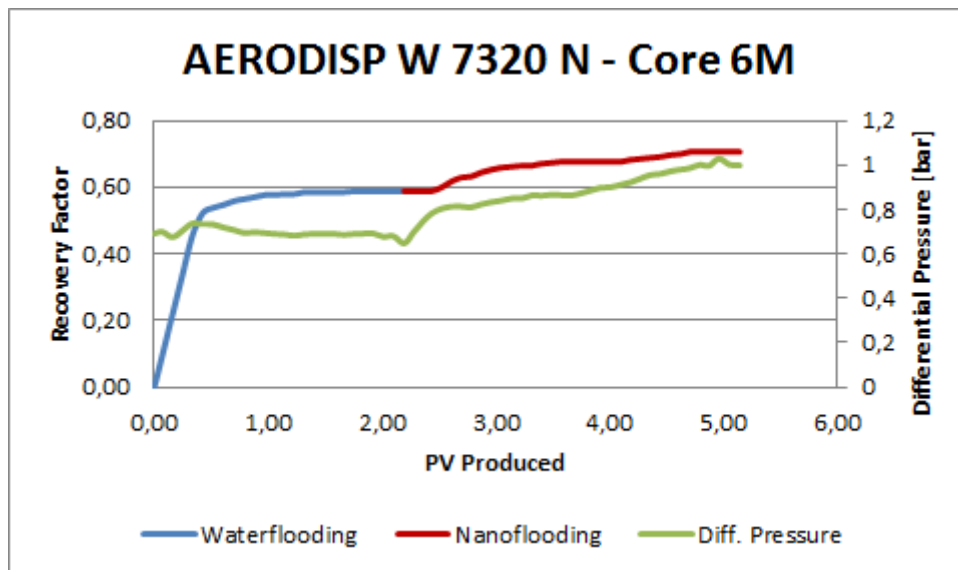


FIGURE C.3: AERODISP W 7320 N flooding in medium permeability core.

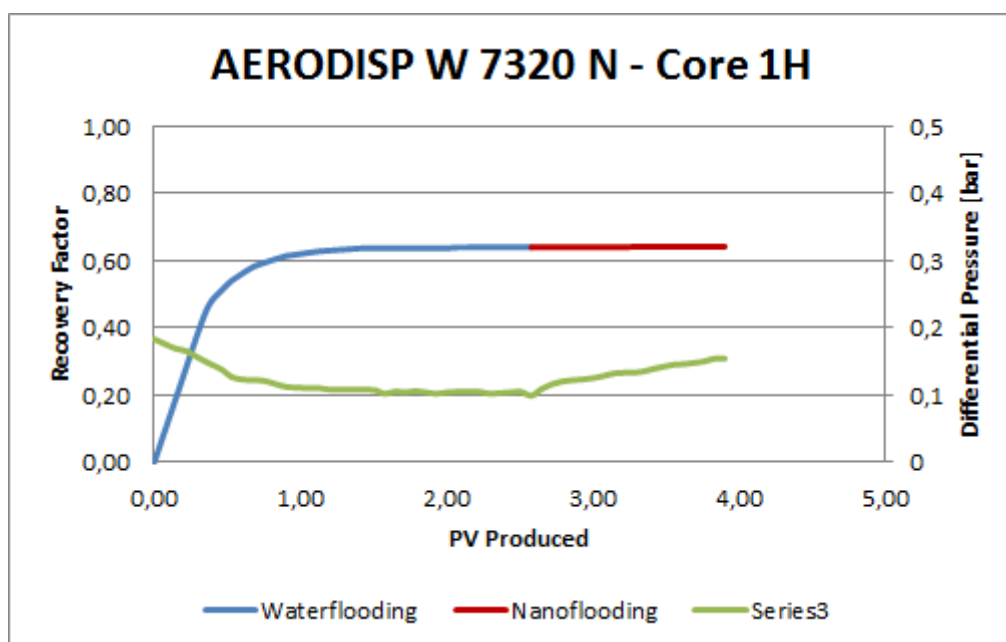


FIGURE C.4: AERODISP W 7320 N flooding in high permeability core.

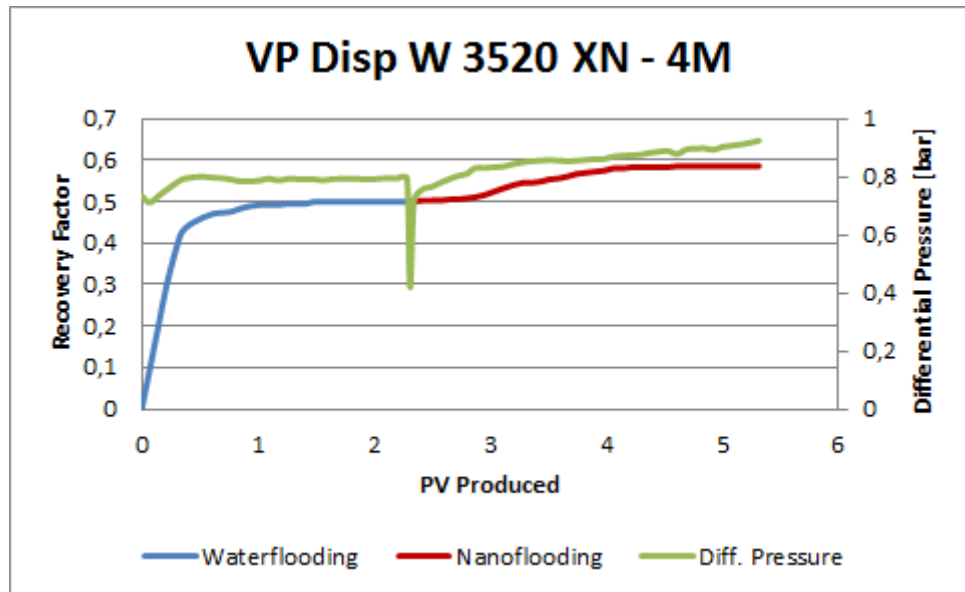


FIGURE C.5: VP Disp W 3520 XN flooding in high permeability core.

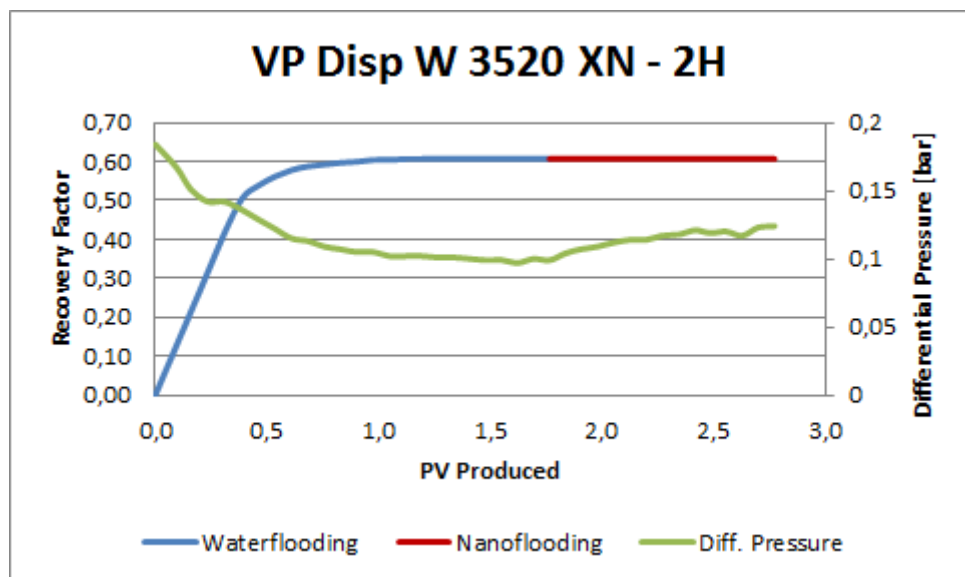


FIGURE C.6: VP Disp W 3520 XN flooding in high permeability core.

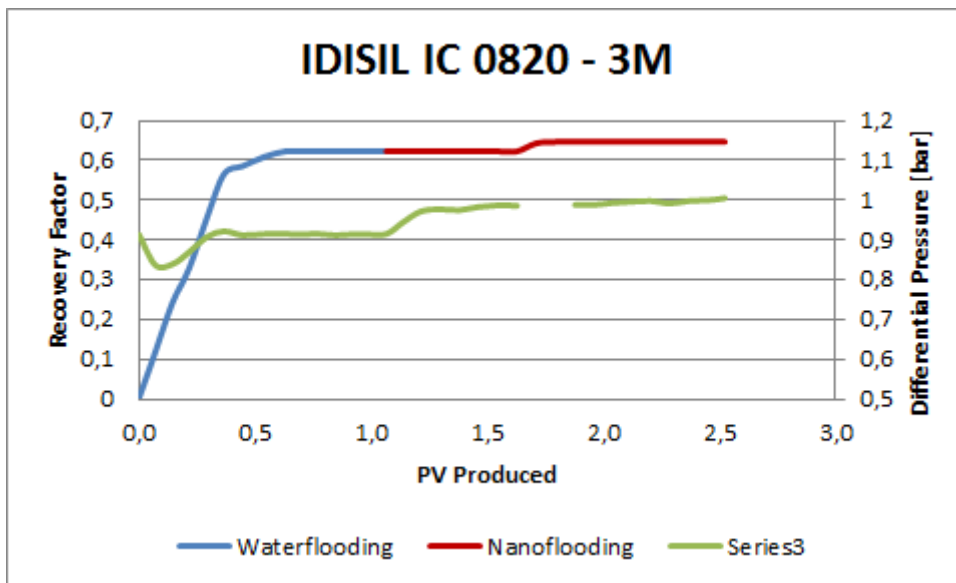


FIGURE C.7: IDISIL IC 0820 flooding in high permeability core.

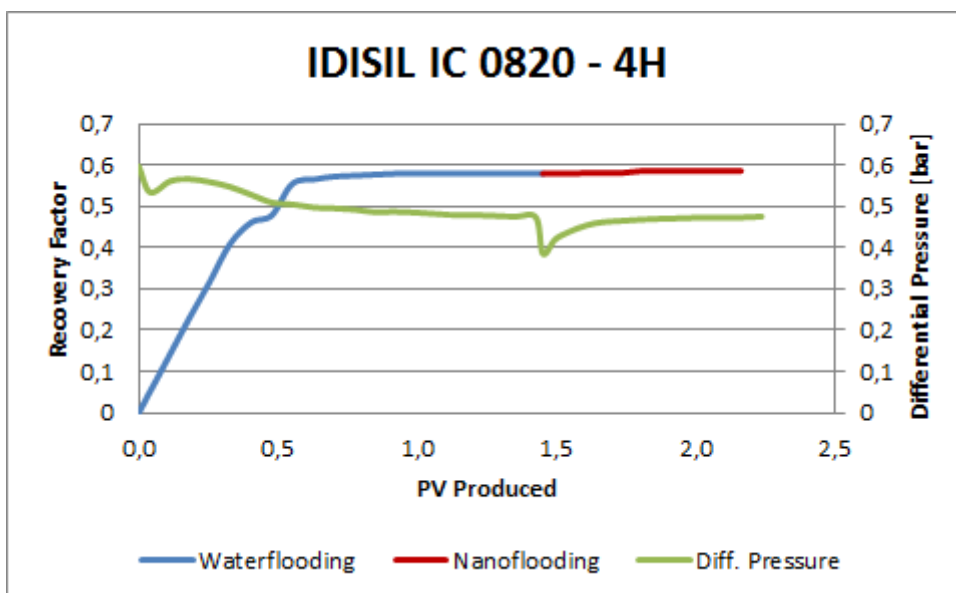


FIGURE C.8: IDISIL IC 0820 flooding in high permeability core.

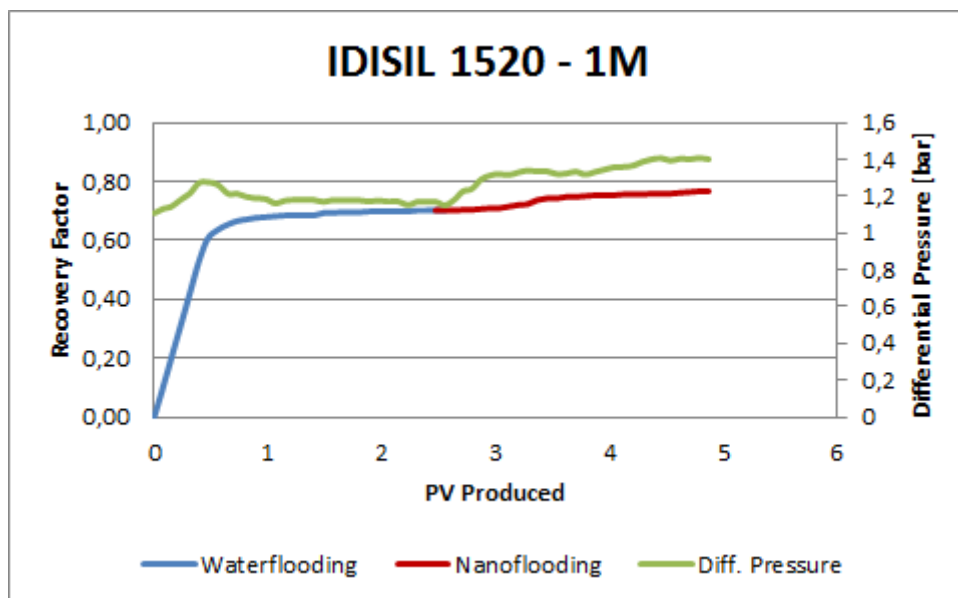


FIGURE C.9: IDISIL SI 1520 flooding in high permeability core.

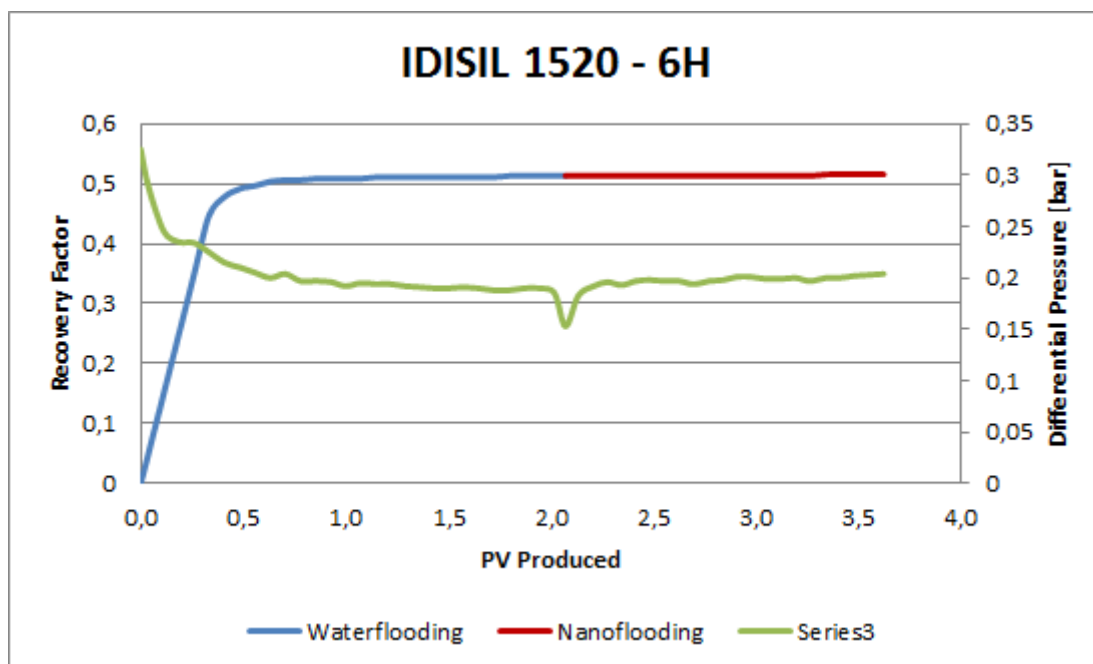


FIGURE C.10: IDISIL SI 1520 flooding in high permeability core.

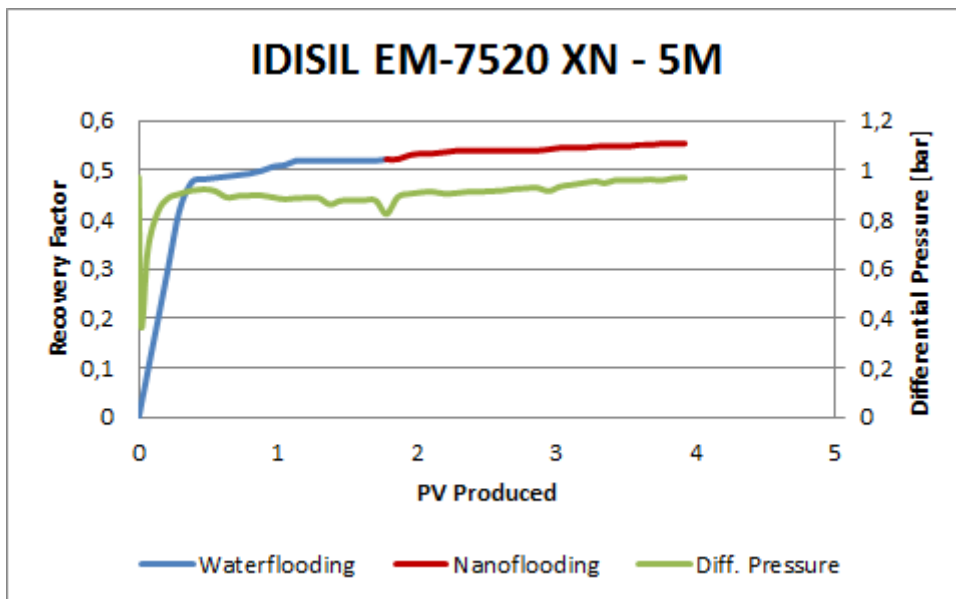


FIGURE C.11: IDISIL EM-7520 K flooding in high permeability core.

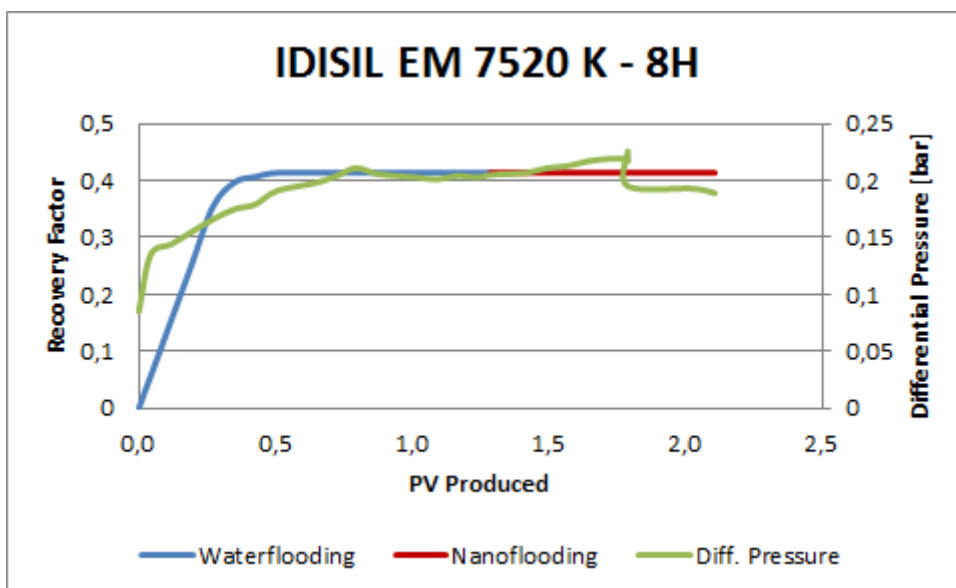


FIGURE C.12: IDISIL EM-7520 K flooding in high permeability core.

The following graphs contain the concentration tests:

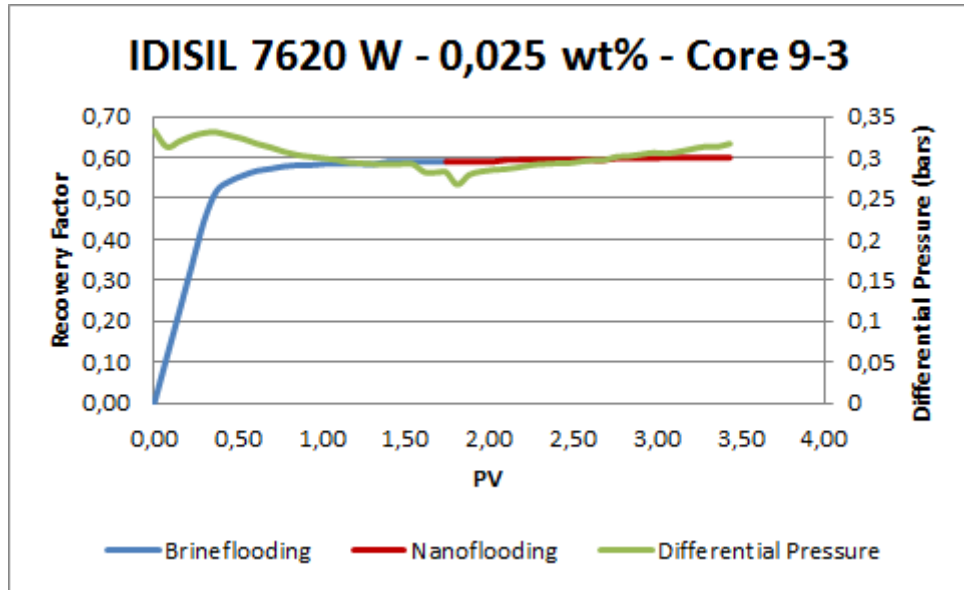


FIGURE C.13: IDISIL 7620 W at 0,025% flooded in medium permeability core.

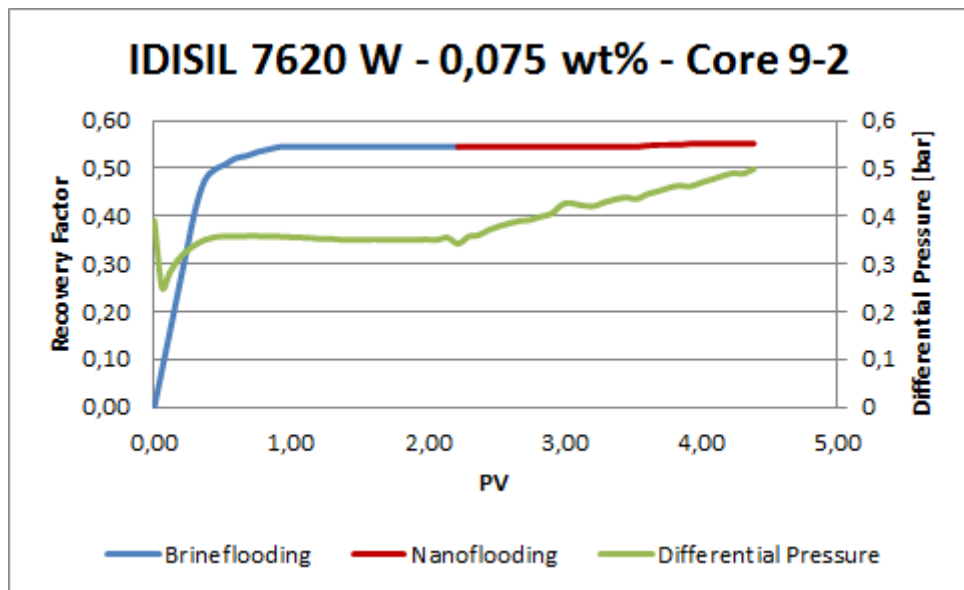


FIGURE C.14: IDISIL 7620 W at 0,075% flooded in medium permeability core.

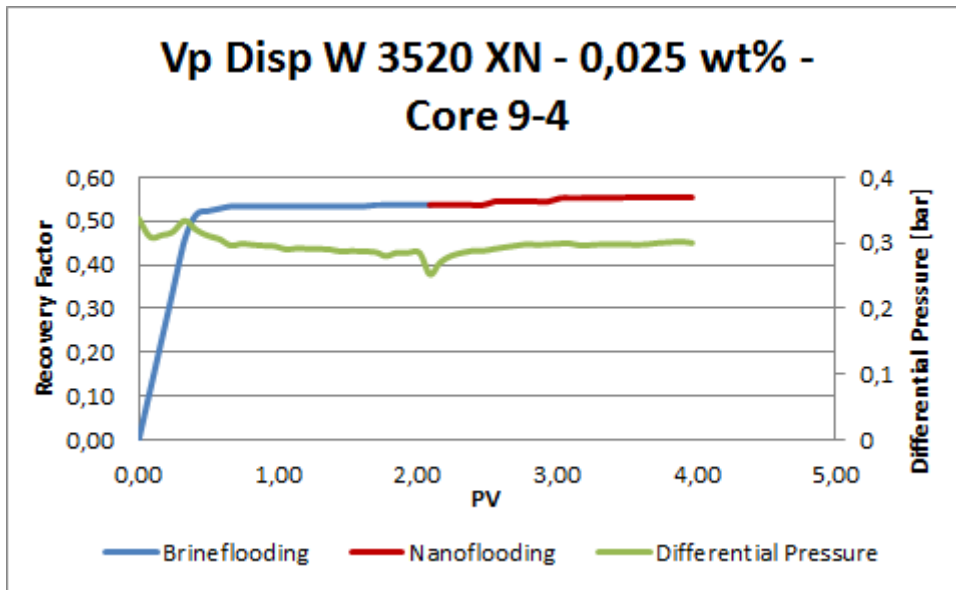


FIGURE C.15: Vp Disp W 3520 XN at 0,025% flooded in medium permeability core.

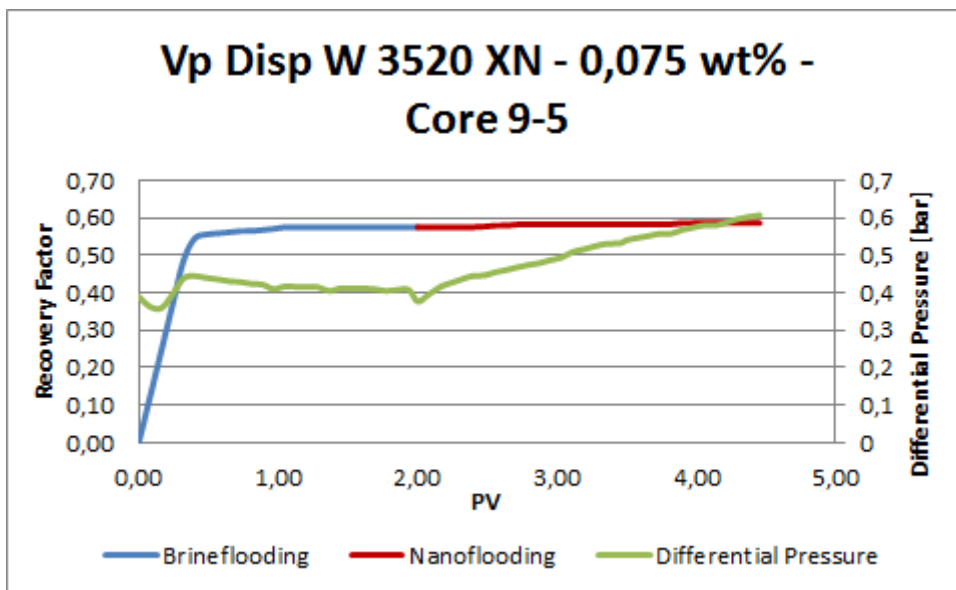


FIGURE C.16: Vp Disp W 3520 XN at 0,075% flooded in medium permeability core.

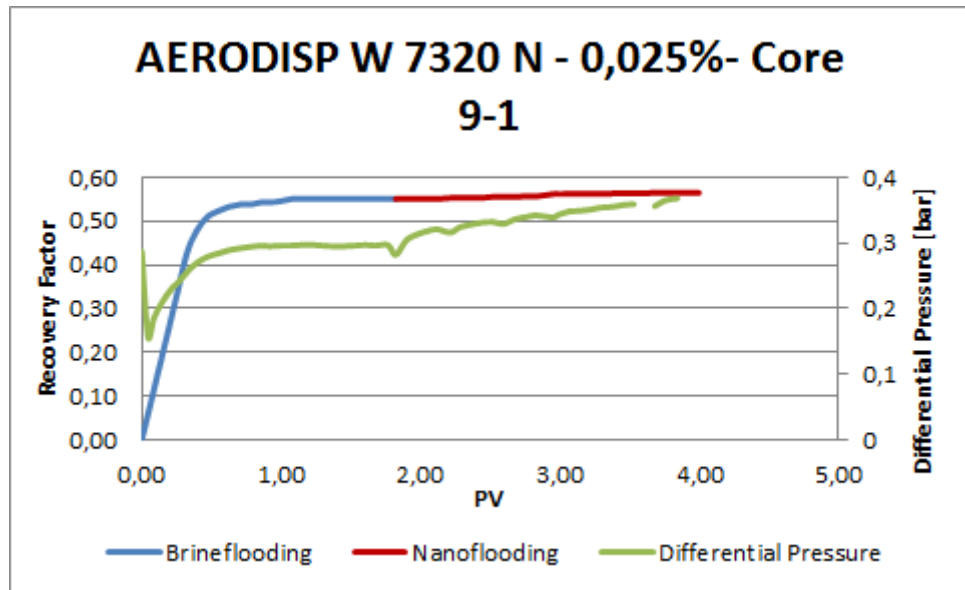


FIGURE C.17: AERODISP W 7320 N at 0,025% flooded in medium permeability core.

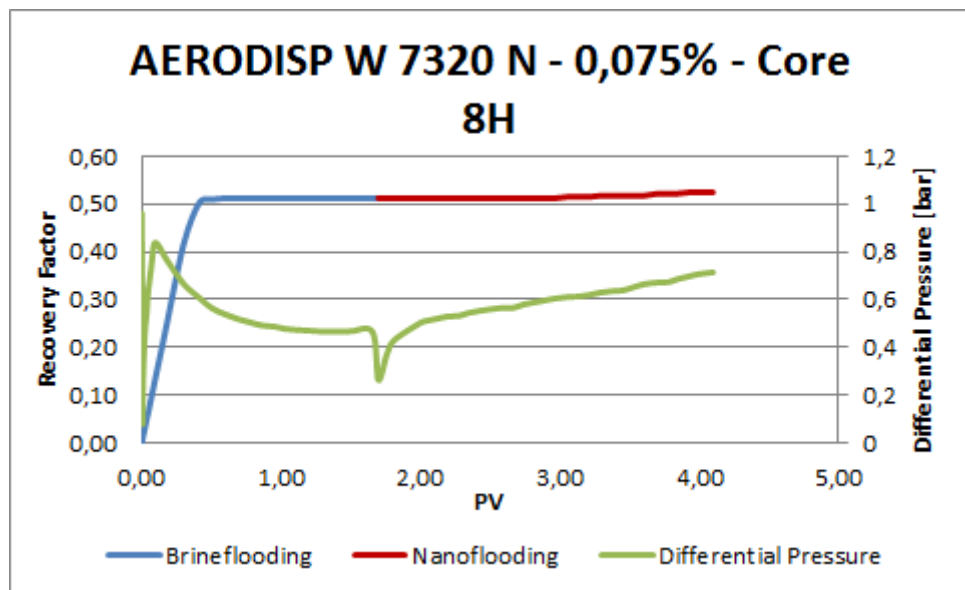


FIGURE C.18: AERODISP W 7320 N at 0,075% flooded in medium permeability core.

The following graphs contain the verification tests tests:

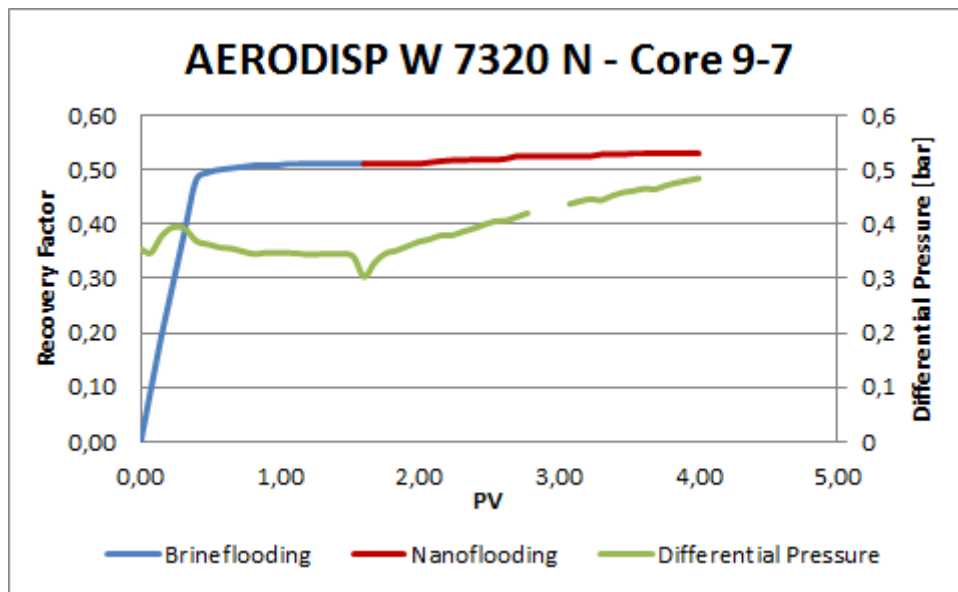


FIGURE C.19: Verification tests with AERODISP W 7320 N at 0,05% flooded in medium permeability core.

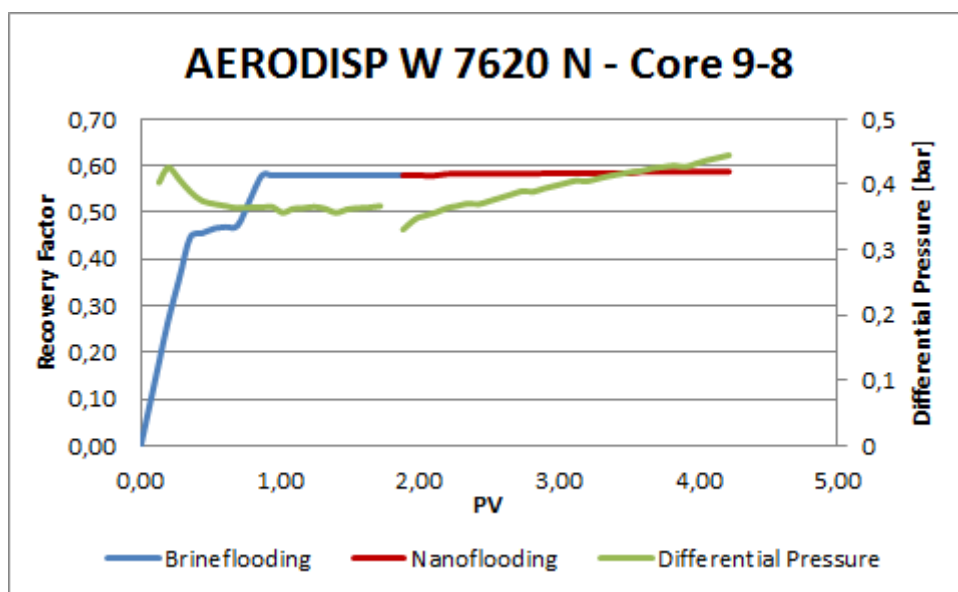


FIGURE C.20: Verification tests with AERODISP W 7620 N at 0,05% flooded in medium permeability core.

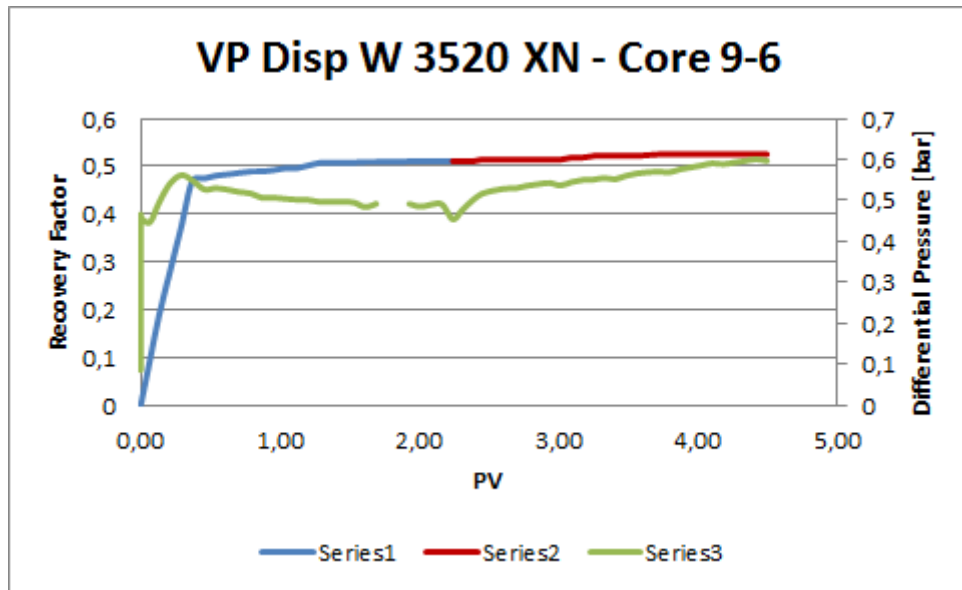


FIGURE C.21: Verification tests with VP Disp W 3520 XN at 0,05% flooded in medium permeability core.

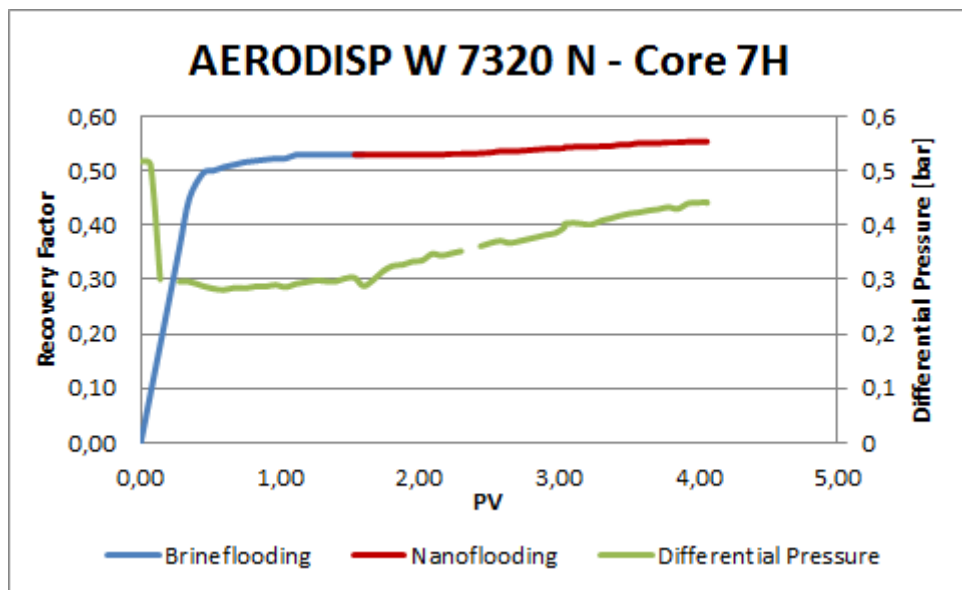


FIGURE C.22: Verification tests with AERODISP W 7320 N at 0,05% flooded in high permeability core.